



Norwegian University of
Science and Technology

Exploring Biopolymers by the Fibre Bundle Model

Sunniva Indrehus

Master of Science in Physics and Mathematics

Submission date: July 2017

Supervisor: Alex Hansen, IFY

Co-supervisor: Pietro Ballone, IFY

Norwegian University of Science and Technology
Department of Physics

Abstract

Bundles of polymeric chains in biological systems represent the analogue of macroscopic fibrous materials such as textile, wood or paper, scaled down to nanometric dimensions, and performing the same mechanical functions of their macroscopic counter-parts. The scale reduction, however, does not leave the physical picture unchanged, but it amplifies surface effects, fluctuations, and affects phase transformations taking place into the system.

The thesis is devoted to the exploration of these size and time scale effects, using molecular dynamics approach based on an idealised force field model. The focus of the investigation is on creep and fatigue, that represent irreversible aging processes due to the thermal breaking of bonds. On the long time scale, and under tensile load, both processes cause the breaking of fibre bundles.

For nearly a century the so called fibre-bundle model has been the method of choice to model creep and fatigue in macroscopic materials.

My work, based on a preliminary study carried out in my host group, aimed at developing, implementing and validating a simulation approach intermediate between the fibre-bundle model and the atomistic simulation models prevalent in biophysics and materials science.

The main portion of the thesis reports results from representative simulations, showing that the new model opens the possibility of investigating a wider range of phenomena than otherwise possible.

The thesis work has many possible developments and applications in biophysics and in nanotechnology, that are briefly outlined at the end of the thesis.

Sammendrag

Polymeriske fiberbunter representerer en analog til makroskopiske fibermaterialer som tekstil, tre og papir i biologiske systemer. På nanoskala fungerer fiberbuntene med samme mekaniske funksjonalitet som sine makroskopiske motsetninger, men med forminsking av lengdeskalaen endres det fysiske bildet. Systemets overflate-effekter, fluktasjoner og faseoverganger forsterkes.

Molekylærdynamikk basert på en ideell kraft felt model ble brukt som fremgangsmåte for å undersøke tids- og størrelseseffekter på nanoskala. Kryp og utmattelse representerer irreversible ald-ringsprosesser i materialer forårsaket av termisk rykning av bånd. Over lang tid, og under påføring av kraft, resulterer disse prosessene i fiberbrudd.

Fiber bunt modeller har gjennom nesten et åthundre vært den foretrukne metoden for å undersøke kryp og utmattelse i makroskopiske materialer.

Mitt arbeid, basert på en forhåndsstudie gjennomført i min verstgruppe, har forsøkt å utvikle, implementere og validere en simuleringsmetode som forener fiber bunt modellen og tilgjengelige metoder i bio- og materialfysikk.

Oppgavens hoveddel fremlegger resultater fra representative simuleringer. Den nye modellen åpner dørene til en dypere forståelse av disse fenomenene på nanoskala.

Arbeidet presentert i oppgaven har potensielle anvendelser i biofysikk og nanoteknologi. Disse er skissert i siste del av oppgaven.

PREFACE

This thesis completes the degree of Master of Science and Technology (Sivilingeniør) in Applied Physics and Mathematics at the Norwegian University of Science and Technology, NTNU. It is the work of one semester (TFY4900) equivalent to 30 credits. The thesis is a continuation of the work I did in my project 'Creep Failure in Polymeric Materials: A Computational Study' in the Fall Semester of 2016.

The results presented in the thesis are based on computations I performed within the group of Prof. Alex Hansen. The computations have been performed with the computer resources of the Department of Physics.

The time evolution of the breaking procedure in the bundles was visualised with the simulation program *jmol*. The illustrations have been created with the graphic \TeX -packages *TikZ* and *chemfig*.

Some additional videos can be found online [here](#).

Trondheim,
July 6, 2017
Sunniva Indrehus

ACKNOWLEDGEMENTS

There are a lot of people that deserve credit for aiding me with this thesis. This document would never have been completed without the help from patient supervisors, fellow students, friends and family.

I would first like to thank my supervisors Prof. Alex Hansen and Adj. Prof. Pietro Ballone, for generously including me in their group and letting me work with their models. Sincere thanks to Pietro for the countless hours he has spent discussing, teaching, correcting and guiding me through the processes leading to this thesis. He has given me the space needed to perform mistakes and learn from them.

Gratitude is extended to the PhD candidate Eivind Bering for useful discussions and comments.

Furthermore, I would like to extend my thanks to the fellow students in the '!! Lønjs-gjengen !!'. Our daily meals have brought me both relevant and irrelevant, but always interesting discussions.

I would also like to acknowledge Jon Krognæs for providing me the tools to gain confidence.

Appreciation is extended to Tor Ytrehus. His scientific coffee cups during my years in Trondheim have been truly inspiring.

I greatly thank my parents and sister for their unconditional support and encouragement throughout my study.

Finally, my dearest Johan. Thank you for the love and the music.

S. I.

CONTENTS

Abstract	i
Sammendrag	iii
Preface	v
Acknowledgements	vii
List of symbols	xiii
Acronyms	xv
1 Introduction	1
2 Of chains and bundles	5
2.1 Chain models	6
2.1.1 Statistical mechanics of ideal chains	6
2.1.1.1 End-to-end vector	6
2.1.1.2 Chain stiffness	7
2.1.1.3 The radial distribution function	7
2.1.2 Statistical mechanical models of biopolymers	8
2.1.2.1 Freely Jointed Chain	8
2.1.2.2 Extensible Freely Jointed Chain	9
2.1.2.3 Worm Like Chain	9
2.1.3 Real chains	10
2.1.3.1 The effect of the excluded volume	10
2.2 The phenomenon of creep	10
2.2.1 The Kelvin-Voigt Model	11
2.3 Fibre Bundle Models	13
2.3.1 Traditional FBMs	13
2.3.1.1 FBM and scaling relations	15
2.3.1.2 FBM and creep experiments	15
2.3.2 A first implementation of a particle based FBM	15

2.4	Biobundles	16
2.4.1	Building a macromolecule	16
2.4.1.1	Making nanobundles	17
2.4.2	Experimental methods	18
2.4.2.1	Fibre diffraction	18
2.4.2.2	Microscopy and fluorescence	19
2.4.2.3	Force spectroscopy	19
2.4.2.3.1	Atomic force microscope	20
2.4.2.3.2	Optical tweezer	20
2.4.2.3.3	Magnetic tweezer	21
2.4.2.4	Modern <i>in vitro</i> tools	21
3	Polynucleotides	23
3.1	Molecule structure	23
3.2	Force-displacement curves	23
3.3	Torsional constraints	26
3.4	DNA origami	26
3.5	The cell nucleus	26
3.5.1	Mechanical properties of whole cells	26
3.6	Chromatin	27
3.6.1	Transitions during stretching	27
3.6.2	The 30 nm-fibre	28
4	Polysaccharides	31
4.1	Molecule structure	32
4.2	Structural changes during stretching	32
4.3	Mechanical properties of nanocellulose	32
4.4	Polysaccharide hydrogels	33
4.4.1	Alginate	34
5	Polypeptides	35
5.1	Molecule structure	35
5.2	Collagen	36
5.2.1	Load transfer mechanisms	36
5.3	Amyloids	37

5.4	The mechanics in the cytoskeleton	38
5.4.1	Actin	38
5.4.1.1	Stress fibres	40
5.4.2	Tubulin	40
5.4.3	Intermediate filaments	41
5.5	Spider silk	41
6	Molecular dynamics	43
6.1	Numerical algorithm	43
6.1.1	Verlet algorithms	45
6.2	Impact of bead-bead interactions	46
7	Our numerical model	47
7.1	System Hamiltonian	48
7.1.1	Two different but related chain models	49
7.1.2	The Lagrangian	51
7.1.3	Temperature with Langevin Dynamics	52
7.2	Investigated values	52
7.2.1	The choice of time step Δt	53
7.3	Limitations of the model	53
8	Results	55
8.1	Sample preparation	55
8.2	Regular finite bundle	57
8.2.1	Evolution under tension	58
8.2.2	The effect of the force	58
8.2.3	The effect of the temperature	60
8.3	Regular periodic bundle	60
8.3.1	Constant strain rate	65
8.3.2	Low density samples	66
8.4	Extensible periodic bundle	66
9	Summary and conclusions	73
	Bibliography	77

List of Symbols

- D_0 Potential well depth.
- E Elastic modulus.
- E_s Elastic spring modulus.
- F External tensile load.
- L_z Instantaneous system length.
- P_{2D} Kinetic 2D pressure along x - and y -direction.
- $U(\mathbf{r})$ Non-bonded interaction potential.
- $V_M(\mathbf{r})$ Morse potential.
- $V_{wall}(\mathbf{r})$ Non-bonded interaction potential at head beads.
- W Phenomenological system mass.
- Δt Time step.
- $\Theta - point$ Theta point.
- \bar{n}_b Number of broken bonds in a chain.
- \bar{n}_c Number of broken chains in a bundle.
- $\beta - sheet$ Beta-sheet.
- \mathbf{R} End-to-end vector.
- $\beta(t)$ Thermal noise.
- ϵ Strain.
- η Dashpot viscosity.
- ϕ Polymer stiffness.
- $\phi(r_{i,j})$ Pairwise additive potential.

σ Stress.

σ_{TS} Tensile strength.

τ Bundle lifetime.

ξ Fluctuations in the system.

a_0 Potential well width.

b Kuhn length.

$g(\mathbf{r})$ Pair correlation function.

k_B Boltzman's constant.

l_s Segment length.

l_c Contour length.

l_p Persistence length.

m Individual bead mass.

n Degree of polymerisation.

n_b Number of beads in a chain.

n_c Number of chains in a bundle.

r_e Equilibrium distance.

s_p Number of bonds in persistence segment.

$x_c(j)$ Critical extension length of a fibre.

Acronyms

1D one-dimensional.

2D two-dimensional.

3D three-dimensional.

AFM Atomic Force Microscope.

bp Base Pair.

CPU Central Processing Unit.

DNA Deoxyribonucleic Acid.

ds-DNA double strand-Deoxyribonucleic Acid.

ECM Extracellular Matrix.

ELS Equal Load Sharing.

FBM Fiber Bundle Model.

FJC Freely Jointed Chain.

FJC+ Extensible Freely Jointed Chain.

LD Langevin Dynamics.

LLS Local Load Sharing.

MD Molecular Dynamics.

MEMS Microelectromechanical systems.

MT Magnetic Tweezer.

NC Nanocellulose.

OT Optical Tweezer.

PBC Periodic Boundary Condition.

RNA Ribonucleic Acid.

SEM Scanning Electron Microscope.

SMFS Single Molecule Force Spectroscopy.

ss-DNA single strand-Deoxyribonucleic Acid.

TEM Transmission Electron Microscopy.

VL Verlet's List.

WLC Worm Like Chain.

WLC+ Extensible Worm Like Chain.

1 | INTRODUCTION

Fibrous materials are ubiquitous in nature, since in the form of cellulose, wood, collagen and chitin they represent a large portion of all the biomass produced every year on Earth. Moreover, these same materials provided the basis for important early technologies from textile to paper production.

Scientists, and physicists in particular, strive to identify common structural motives and characteristic properties in the observable reality, and natural or artificial inpolymer molecules, bundles and fibres easily provide examples of such paradigmatic classes, and became the subject of systematic studies [1].

Recently the interest in systems of this kind has been revived by the rapid development of biophysics and of nanotechnology, dealing with fibres and bundles of microscopic dimensions [2]. At the size and time scale of interest for these new disciplines, the usual macroscopic laws can no longer be taken for granted [3], and our general view of the the behaviour and properties of fibres and bundles has to be re-assessed and validated anew.

My investigation targets the properties of fibres and bundles of biological origin and of nanometric size. It focuses, in particular, on a characteristic phenomenon of materials, and polymers in particular, that goes under the name of *creep*, consisting of the gradual degradation over time of the mechanical resistance of fibre bundles under tensile solicitation, eventually leading to the bundle failing under a subcritical load.

My study builds on the long tradition at our Physics Department of theoretical and computational investigations of creep in fibre bundles based on the so called *Fiber Bundle Model* (FBM) that will be discussed extensively throughout the thesis.

The FBM describes the system in terms of bond, organised into chains. A kinetic model of random chain breaking is derived from very basic assumptions on the resistance of each bond, and from more crucial assumptions about the redistribution of load following the progressive breaking of chains. The results of computer simulations based on the FBM connect the kinetics of single bond breaking to collective phenomena such as the sudden collapse of the bundle in the final stages of creep. The collapse, in particular, occurs when the increase of the load on intact chains turns the random breaking of bonds into a highly correlated sequence, causing an avalanche of bond breakings.

Because of its idealised character, the FBM is particularly able to give information on general or even *universal* aspects, and on scaling relations. However, in its basic formulation, it lacks a microscopic time scale, as well as a detailed description of the structure and dynamics of the polymeric

material at the atomistic level.

The evolution of our interest for fibre bundles towards nanometric biosystems increasingly requires a chemically accurate picture of fibre bundles as well as a detailed account of all interactions. The quantitative inclusion of real time dynamics is also required.

In the last few years, the development of models and of computer methods and facilities has prepared the stage for such a detailed description, especially through the development of a broad machinery of approaches, from empirical force fields to ab-initio methods, and from *Molecular Dynamics* (MD) to Monte Carlo.

It is well known that computer simulation methods are limited in their ability to cover size ranges of interest for real-life systems, and, even more, the time scales relevant for complex mechanical phenomena such as creep. However, the simultaneous growth in global computer capabilities, together with the increasing focus on smaller and smaller systems is easing the matching of problems and capabilities, bringing creep within the reach of present day methods.

A publication by G.Linga et al. [4] represents a recent development along these lines, since it introduced MD to investigate creep in a still very idealised model. The system is described as an assembly of bonds and *particles* of mass m , reintroducing real time evolution into the picture and allowing for a wider range of investigations than possible with the original FBM. For instance, the model allows to investigate how dynamical modes and excitations of the polymer affect the onset of creep, and to analyse the microscopic mechanisms leading to bond breaking and eventually to the bundle failing. Moreover, the model allows to consider a time dependent load, and to investigate fatigue in addition to creep. The model, however, neglects non bonded interactions among beads beyond the nearest neighbours along each chain. As such, the model is unsuitable for the investigation of important issues such as excluded volume effects, that tend to increase the size of chains, or the effect of attractive forces among beads, that tend to shrink chains. The model is also unable to reproduce transitions between different phases of the bundle, such as the liquid state at high temperature, and the glassy state at low temperature. Moreover, no finite size or surface effect could be observed since the interactions among beads in the transversal plane are neglected. Last but not least, the lack of surface effects and of surface tension in particular, qualitatively modifies the way creep evolves during the last avalanche stage, thus undermining the description of arguably the most important stage of the phenomenon under study.

The aim of my project has been to re-introduce non-bonded bead-bead interactions into the basic model used to investigate creep by MD. The model that I implemented represents the system to a coarse grained level, and allows to simulate bundles of many thousand neutral particles over long simulation times. The aim of the thesis is to define the model, discuss the details of its implementation

in a simulation code, and present the results of representative simulations.

As already anticipated, the focus of my work is represented by nanometric fibre bundles in systems of biological origin. Since it is not easy to find in the literature a systematic account of this class of systems and of their mechanical properties, in the first part of the thesis I provide an overview of experimental and theoretical studies of bundles in biological systems. I discovered that most of the recent experimental studies strived to reach the single-molecule limit. While the interest of such a measurement is apparent, I argue that identifying and modelling the effect of joining chain molecules into a bundle is at least as crucial, and deserves a larger effort than is now being made.

The importance of these topics is enhanced by the recent appreciation of the role of mechanical forces in the life and functioning of cells. For instance, cells sense and respond to mechanical signals from the environment as much as to biochemical ones. The stiffness of the *Extracellular Matrix* (ECM), the compression applied by neighbouring tissue and by external forces impose changes in the cytoskeleton [5]. Further, elucidating the time dependent properties of the cell nucleus, including its response to external mechanical perturbations, is regarded as one of the 'grand challenges' in modern structural and molecular biology [6]. Application of single-molecule manipulation techniques has advanced our knowledge of biomolecules such as *Deoxyribonucleic Acid* (DNA), *Ribonucleic Acid* (RNA), proteins, and viruses [7]. During the last decade, a number of studies aimed at identifying the signature of cancer in the response of cells to mechanical forces. Cancer cells have been identified as softer than cells from normal tissue [8], and cell migration is the driving force behind tissue invasion and the cancer metastasis [9]. Eventually, all these properties and phenomena will be amenable to investigation by computer simulation, possibly based on multi-scale algorithms able to span a wide range of length and time scale.

The thesis is organised as follows: Chapter 2 gives a short introduction to the statistical mechanics describing biopolymeric chains and bundles, their mechanical properties, and existing measurement techniques. Chapters 3, 4, and 5 present stretching experiments on paradigmatic biopolymers, i.e., polynucleoties, polysaccharides, and polypeptides. A minimal description of the MD-simulation technique is presented in Chapter 6. Our physical and numerical approach together with the results of the simulations, are presented respectively in Chapters 7 and 8. Chapter 9 states a conclusion for my investigations and outlines future developments for the subject of my thesis.

2 | OF CHAINS AND BUNDLES

*“One Bundle to rule them all, One bundle to find them,
One Bundle to bring them all and in the darkness bind them.
In the Land of Mordor where the Shadows lie.”*

– Adapted from J. R. R. Tolkien, Lord of the Rings

The first structural motif shared by the systems of interest for the present study is represented by chains, that, in chemical terms, will consist of polymers, and in particular of biopolymers.

Each biopolymer is characterised by its chemical composition, that largely determines the number and quality of the chemical bonds among atoms. Other properties such as the degree of polymerisation n^1 may depend also on the past history of the molecule, sometimes deviating from strict chemical and thermodynamic equilibrium over macroscopic time intervals. Long term metastability may affect many other properties of biopolymers. Proteins, for instance, are folded into their working conformation while being formed within ribosomes, and might not reach their thermodynamic equilibrium state during their entire lifetime.

Like most industrial polymers, biopolymers belong to the vast class of organic compounds. Biopolymers, however, tend to be more complex than their artificial counterpart, at least because they tend to be heteropolymers, sometimes to an extreme degree. Moreover, and more importantly, biopolymers often interact with water and among themselves to give origin to a variety of supra-molecular structures. For instance, they might be joined into chain bundles, that represent the second structural motif and the primary reason of interest of the systems discussed in the present thesis.

The first half of this chapter collects basic information on how chains and bundles are modelled in statistical mechanics and in computational materials science. A crucial relaxation channel that characterises non-equilibrium polymeric materials is creep, that will be defined in this section, and will be discussed extensively through the following chapters. The second half of the chapter is devoted to a brief outline of the experimental methods that allow us to characterise the properties of biopolymers and of their bundles, sometimes down to their atomistic details.

¹Determined by the number of monomers.

2.1 Chain models

At the most idealised level of abstraction, we can picture a biopolymer molecule as a collection of bonds and particles. Bonds can be flexible or semiflexible, giving origin to a large conformational space, thus enhancing the role of the system entropy [10].

With increasing temperature, in particular, a huge number of rotational isomeric states might become accessible to the system dynamics, opening the way to fluid phases. Polymers in the melt visit distinct configurations according to the Boltzmann probability distribution [11, Chapter 2].

2.1.1 Statistical mechanics of ideal chains

General features of polymeric materials are captured even by idealised models, whose predictions can be worked out analytically. Models of this kind are based (at least implicitly) on a simple Hamiltonian, that is parametrised with the equilibrium value of bond lengths, bending and torsion angles of the polymer under investigation.

Properties that need to be reproduced by the model include a variety of thermodynamic properties such as density, cohesive energy, bulk modulus and Young's modulus, together with a variety of elastic constants from the harmonic dynamics of bonds to the Rouse dynamics of chains [6].

Although a few polymers tend to be partly or even fully crystalline at low temperature, most polymeric materials turn into a glass upon decreasing temperature below the so called glass transition temperature, marking a transformation of the system properties whose nature is still debated.

2.1.1.1 End-to-end vector

The first property of interest for idealised models of chains is the end-to-end vector \mathbf{R} measuring the overall size (and possibly orientation) of the polymeric chain. Mathematically it is defined as

$$\mathbf{R} = \mathbf{r}_{n_b} - \mathbf{r}_1 = \sum_{l=1}^{n_b} \mathbf{a}_l, \quad (2.1)$$

where \mathbf{a}_l describe the distance between bead number $\mathbf{r}_j = \mathbf{r}_{i+1} - \mathbf{r}_i$ and \mathbf{r}_i . n_b denotes the total number of beads in the chain. In a homogeneous and isotropic system \mathbf{R} averages to zero because all orientations are equally likely.

The simplest non-zero average value that could be computed is the mean-square of the end-to-end vector $\langle \mathbf{R}^2 \rangle$. In ideal chains there typically exists no correlations between monomers separated by a great distance. For bonds of the same length and no correlation along the chain the expression is

given:

$$\langle \mathbf{R}^2 \rangle = \left\langle \left(\sum_{l,l'=1}^{n_b} a_l \right)^2 \right\rangle = \left\langle \sum_{l,l'=1}^{n_b} a_l \cdot a_{l'} \right\rangle = n_b \langle |a_l|^2 \rangle \delta_{l,l'} = l_c a_l, \quad l_c = n_b a_l. \quad (2.2)$$

Where l_c is the contour length of a chain. In the large limit Eq.(2.2) scale as the number of beads $\langle \mathbf{R}^2 \rangle \sim n_b$.

2.1.1.2 Chain stiffness

The chain stiffness is formally characterised by the persistence length l_p . It is a statistically defined measure of the length the tangent vectors becomes de-correlated. Equivalently it measures the distance along the chain over which bonds tend to align along the same direction. This quantity can be derived from the expression for the end-to-end vector:

$$\langle \mathbf{R}^2 \rangle = \sum_{i=1}^{n_b} \sum_{j=1}^{n_b} \langle \mathbf{r}_i \cdot \mathbf{r}_j \rangle = |r_i| |r_j| \sum_{i=1}^{n_b} \sum_{j=1}^{n_b} \langle \cos \theta_{ij} \rangle, \quad (2.3)$$

where $\cos \theta^{|i-j|}$ is the angle between the two neighbouring beads $\mathbf{r}_j = \mathbf{r}_{i+1} - \mathbf{r}_i$ and \mathbf{r}_i

$$\cos \theta^{|i-j|} = e^{-|j-i| \ln(\cos \theta)} = e^{-|j-i|/s_p}, \quad s_p = \frac{1}{\ln(\cos \theta)}. \quad (2.4)$$

s_p is the number of bonds in a persistence segment. The length of the persistence segment is defined as the persistence length l_p :

$$l_p = l s_p. \quad (2.5)$$

At the length scale below l_p chains behaves like rigid rods.

2.1.1.3 The radial distribution function

The pair correlation function $g(\mathbf{r})$ measures the conditional probability of finding a particle at $\mathbf{r}_0 + \mathbf{r}$ provided there is one particle at \mathbf{r}_0 . If $\langle dN(\mathbf{r}) \rangle$ is the average number of particles in the volume element $d\mathbf{r}$ at $\mathbf{r}_0 + \mathbf{r}$ given the reference particle at \mathbf{r}_0 , the pair distribution function is defined as:

$$\langle dN \rangle = \rho(\mathbf{r}_0 + \mathbf{r}) g(\mathbf{r}) d\mathbf{r} \quad (2.6)$$

where $\rho(\mathbf{r}_0 + \mathbf{r})$ is the one-body density in the system at position $\mathbf{r}_0 + \mathbf{r}$.

In a homogeneous system, $g(\mathbf{r})$ is a function of the scalar distance $|\mathbf{r}|$, and $g(r)$ is known as the radial distribution function. In a liquid, both $g(\mathbf{r})$ and $g(r)$ are expected to tend to a value of one in the

Table 2.1: The most common statistical-mechanical models for describing the biopolymer elasticity [12]. F denotes the tensile load, x the equilibrium end-to-end separation, l_c the contour length, k_B the Boltzmann's constant, T the temperature, l_p the persistence length, l_s the segment length, E_s elastic constant of the segment spring, and ϕ the specific stiffness of the polymer.

Model	Expression
FJC	$x(F) = l_c \left[\coth \left(\frac{Fl_s}{k_B T} \right) - \frac{k_B T}{Fl_s} \right]$
WLC	$F(x) = \frac{k_B T}{l_p} \left[\frac{1}{4} \frac{1}{1 - \frac{x}{l_c}} + \frac{x}{l_c} - \frac{1}{4} \right]$
FJC+	$x(F) = l_c \left[\coth \left(\frac{Fl_s}{k_B T} \right) - \frac{k_B T}{Fl_s} \right] \cdot \left[1 + \frac{nF}{E_s l_c} \right]$
WLC+	$F(x) = \frac{k_B T}{l_p} \left[\frac{1}{4} \left(1 - \frac{x}{l_c} + \frac{F}{\phi} \right)^2 + \frac{x}{l_c} - \frac{1}{4} - \frac{F}{\phi} \right]$

limit of large r , corresponding to the loss of correlation at large distances. This quantity is directly related to the structure factor measured by X-ray, neutron- and light- scattering experiment. Thus it gives a measure of comparison between numerical and physical experiments.

Successful models are able to predict at least qualitatively all the properties listed in the previous subsections. Popular idealised chain models widely used by the polymer physics community include: the *Freely Jointed Chain* (FJC), the *Worm Like Chain* (WLC), the *Extensible Freely Jointed Chain* (FJC+) and the *Extensible Worm Like Chain* (WLC+) [12], that are briefly discussed in the following sub-sections.

2.1.2 Statistical mechanical models of biopolymers

Applying a stretching force on the ends of a polymer bundle with progressively enhance the alignment of chains. The external load slowly reduces the overall entropy of the chain and a small reduction of in the conformation numbers will give rise to entropic elasticity forces. Large extensions bring tension in the molecular backbone and may lead to enthalpic elasticity effects such as bond deformation in the chain, rupture of the intramolecular hydrogen bindings and even conformational changes in the molecule [13]. Four models to describe the polymer elasticity under an applied tensile load are given in Table 2.1.

2.1.2.1 Freely Jointed Chain

The FJC, or the ideal chain, is the simplest possible description of a chain and serves as the starting point for all other models [11, Chapter 2]. A FJC model describes the chain as a random walk with properties determined by the number and the length of each segment. The bonds between neighbouring beads are at a fixed length b^2 , with arbitrary coupling angles between. An illustration of the FCJ

²In the literature referred to as the Kuhn length.

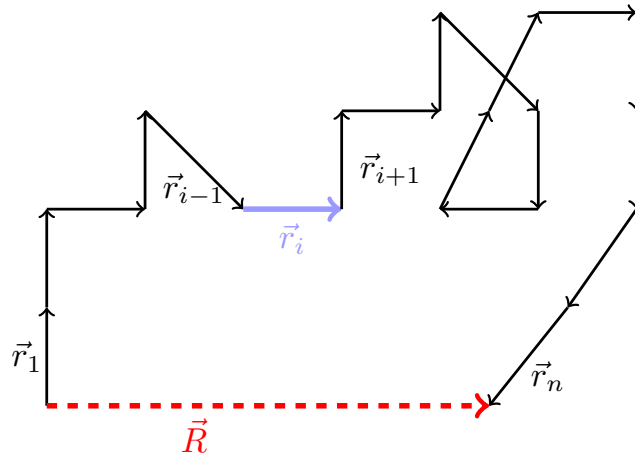


Figure 2.1: Illustration of a short FJC with arbitrary coupling angles between the beads r_1, \dots, r_n . The end-to-end vector \vec{R} is shown in red.

chain is given in Figure 2.1.

The FJC model cannot describe a chain extended beyond its contour length l_c , because the chain would then be infinitely rigid. Flexible polysaccharides comply with the assumptions of the FJC, hence they are will described by this model [10].

2.1.2.2 Extensible Freely Jointed Chain

The *Extensible Freely Jointed Chain* (FJC+) accounts for elastic deformation of bonds and angles neglected in the FJC. The polymer is modelled by n elastic springs with a third fitting parameter E_s accounting for the bond elasticity. At large elongations, forces contain also an additional enthalpic term which allow the chain to be extend beyond its contour length. Despite its simplicity, the FJC+ model is able to reproduce the flexibility transition observed during the stretching of dextran and amylose [12], due to the cleavage of their pyranose rings. Thus, polysaccharides behaving like a series of loosely connected elastic (extensible) rods conform to the assumptions of FJC+, and are well described by this model [14].

2.1.2.3 Worm Like Chain

The WLC or the persistent model, describes chains where the chain stiffness is accounted for with an irregular curved filament linear on the scale of the persistence length l_p [11, Chapter 2]. Even though the model consider both entropic and enthalpic contributions the chains cannot extend beyond its contour length. Rigid biopolymers and proteins behaving like deformable rods [10, 13] and single DNA molecules [15] are generally described by the WLC model. The WLC+ model adds the stiffness of the chains as a third fitting parameter to the WLC model [12].

2.1.3 Real chains

The correspondence of polymer chains and random walks is lost in the case of real chains made of beads of non-vanishing size. In this case, beads along the chain cannot occupy the same position at the same time, a constraint that has a number of consequences that go under the name of ‘excluded volume effects’. Although the non bonded bead-bead pair interaction might be short-ranged, the excluded volume interaction might be felt even at length scales comparable to the chain size. The most obvious manifestation of these effects is represented by expansion of the chain, whose configuration can no longer be considered as the result of a Brownian process (random walk). More details on the excluded volume effect are given in the following subsection.

2.1.3.1 The effect of the excluded volume

Historically, the effect of finite bead size, and therefore of excluded volume has been an important topic in the general discussion of the spatial expansion of long chain molecules in solution. A fundamental contribution on this subject has been given by Pierre-Gilles de Gennes. According to his theory of excluded volume, the effect is qualitatively different in poor solvent (low temperature) or in good solvent (high temperature). In particular:

- Chains remain ideal (or Gaussian) at high temperature, following a standard Brownian statistics.
- At low temperature chains are expanded by excluded volume effects, and need to be modelled as self-avoiding random walks.

Again according de Gennes, in the limit $m \rightarrow \infty$ the change between the two regimes takes the form of a critical phenomenon. Both experiments and simulations have shown that the properties of low temperature chains expanded by finite volume effects scale like simple power laws. The transition is rounded (no longer sharp) in chains of finite length.

Chains with a moderate molar mass often represents a mixed state where the characters of the chains depends on the selected length scale. At the Θ – *point* the ratio between solvent and solution is such that the excluded volume feature can be neglected. An illustration of the excluded volume effect is given in Figure 2.2.

2.2 The phenomenon of creep

Creep is a relaxation mechanism in polymeric materials under moderate tension. It is due to the irreversible breaking of covalent bonds accompanied by the slow increase of the sample length. On a

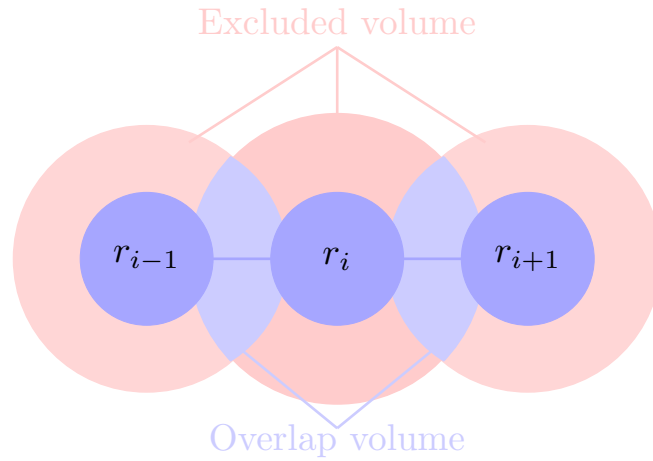


Figure 2.2: Schematic illustration of the effect of the excluded volume displayed in a chain with beads approximated as hard spheres.

time scale that is long compared to typical molecular processes, creep causes the failing of polymeric samples.

In hard materials, such as oxides³ and ceramics, applying stress under the critical limit gives no surprises. The material will restore its original shape after the load is removed. Fractures will occur if one apply '*stress*' σ over a critical limit.

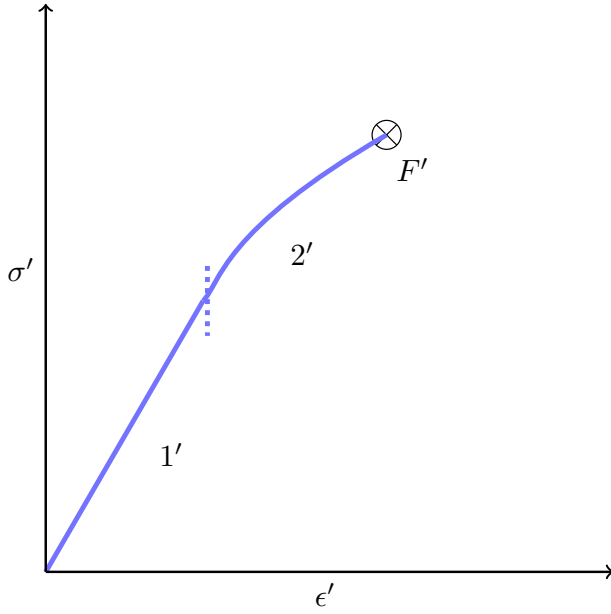
In soft materials, instead, the outcome is failing by creep. In material science, creep is characterised by plotting the sample length whose change from the initial value is called '*strain*' ϵ versus rupture under a fixed load (stress). Typical stress-strain relations for a hard and soft materials and the deformation curve in a soft material under a constant tensile load is given in Figure 2.3. From the curve in Figure 2.3C different stages can be identified. This multistage creep process is a characteristic behaviour of soft matter materials under load.

2.2.1 The Kelvin-Voigt Model

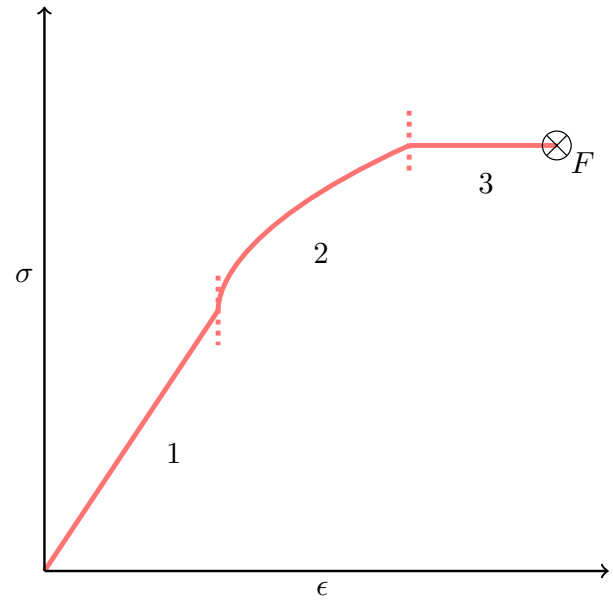
Creep is one of the important manifestations of the non-linear and irreversible properties of polymers that go under the name of visco-elasticity. A large effort is routinely devoted to the experimental, theoretical and computational analysis of these phenomena [11, Chapter 6].

A simple mechanical model of viscoelasticity was proposed long ago by Kelvin and Voigt. The model represents the system as made by an elastic spring of modulus E_s in parallel with a dashpot of viscosity η under a time-dependent stress. The system evolution is often given in real time. For instance, the time dependence of stress $\sigma(t)$ is given by:

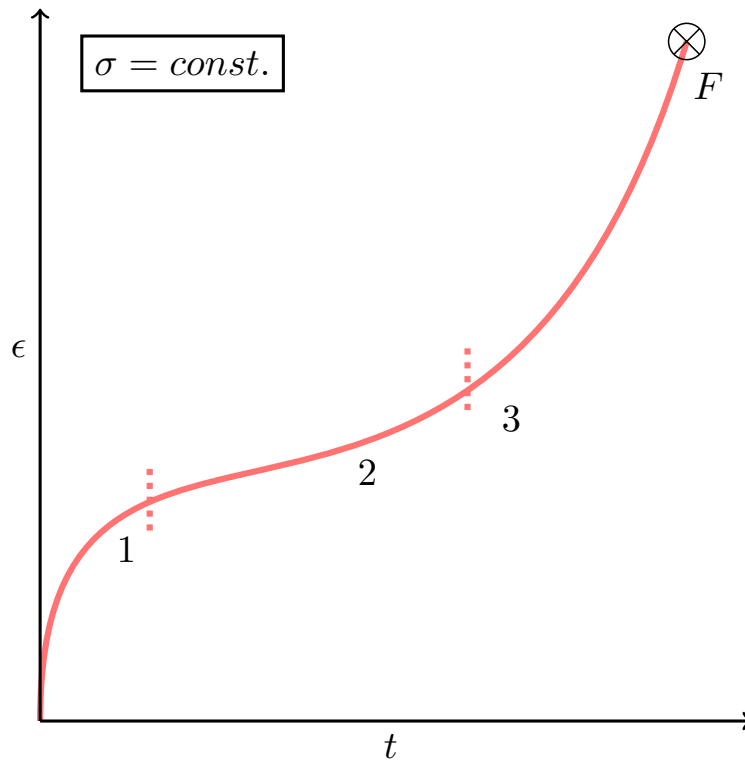
³Creep phenomena can also occur in metals, but only on time scales much longer than that of polymers.



(A) Schematic stress-strain curve in a hard material. After the elastic region (1') the material undergoes hardening (2') before failure (F').



(B) Schematic stress-strain curve in a soft material. After the elastic region (1) the material undergoes a short hardening (2) in front of a creep region (3) before failure (F).



(C) Typical deformation curve of the strain ϵ as a function of time under constant tensile load in a soft material displayed. The creep rate decreases with time in the primary regime, corresponding to the hardening of the sample under load (1). Under the secondary regime (2) the creep rate is a constant slope. In the tertiary regime (3) the creep rate increases with time before a complete failure in the critical point (F).

Figure 2.3: Typical deformation curves. The stress-strain relation in a hard (Figure 2.3A) material. The stress-strain (Figure 2.3B) and the creep relations (Figure 2.3C) in a soft material.

$$\sigma(t) = E_s \epsilon(t) + \eta \frac{d\epsilon(t)}{dt}. \quad (2.7)$$

where $\epsilon(t)$ is the time dependent *strain* or time dependent deformation of the material. The equation says that the time dependent stress is balanced by the normal (linear) elasticity, and by a term arising from the sample deformation, due primarily to creep. Eq. 2.7 is easily solved by computational approaches, and it can be solved analytically in many cases, depending on the choice of variables. A schematic illustration of the Kelvin-Voigt model is given in Figure 2.4.

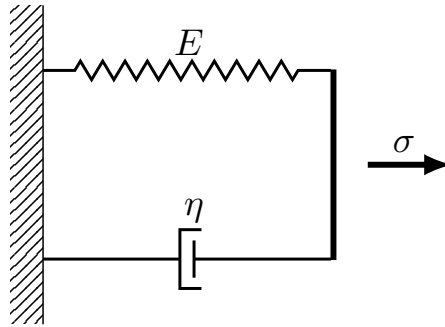


Figure 2.4: Schematic view of the Kelvin-Voigt model. A system with a spring of modulus E in parallel with a dashpot of viscosity η reproduces viscoelastic behaviour under a constant stress σ .

2.3 Fibre Bundle Models

A FBM aims to describe the rupture in a collection of fibres, a bundle, caused by an applied tensile load. Detailed investigations of the rupture phenomenon in materials have been performed by experimentalists in various contexts for a long time. 500 years ago Leonardo Da Vinci studied the strength of iron wires of various lengths [16]. The first scientific treatment of a FBM was given by Fredrick T. Pierce in the context of textile engineering in 1926 [17]. A detailed description of FBMs combining the fields of statistical physics, material science, and computational and simulation methods was given by Hansen et al. in 2015 [1].

2.3.1 Traditional FBMs

A traditional FBM analyses a *one-dimensional* (1D) bundle consisting of N elastic fibres of equivalent length with both ends clamped to some sort of solid support. The fibres are in a two state condition of intact or ruptured. Under an applied tensile load F each fibre elongates as a Hookean spring before it reaches an individual critical extension length $x_c(j)$. Elongation beyond this point causes the fibre to fail, thus it does not contribute any longer to the bundle strength. F is balanced by the combined

Hookean forces from each intact fibre, thus the system is in equilibrium as long as F is kept constant. Figure 2.5 display a schematic illustration of a traditional FBM.

It is common to pick the maximum force a fibre can handle before it breaks, or equivalently the threshold of critical length $x_c(j)$ from a probability distribution $p(x_c(j))$. The force acting on individual fibres is given by:

$$f_j(x) = \begin{cases} E_s x, & x < x_c(j) \\ 0, & x \geq x_c(j), \end{cases} \quad (2.8)$$

where E_s is the elastic constant assigned to individual fibres⁴. The total force on the bundle is $F = \sum_j^N f_j(x)$.

The probability distribution $p(x_c)$ for x and the reorganisation of the force upon intact fibres determines the specific FBM. Two main categories of models are the *Equal Load Sharing* (ELS) and the *Local Load Sharing* (LLS) models. In the ELS, or global load sharing model, the force is distributed equally among intact fibres every time a chain breaks. It is the oldest and simplest FBM. This behaviour differs from the LLS model where the distribution of force on the remaining fibres depends of the state of their neighbours. The fibres can now fail either because they are weak or because they are highly stressed from their weak neighbours [1]. LLS was introduced by Harlow and Phoenix in 1991. The two models approach each other with increasing dimensionality d , that causes both models to approach the mean field limit [18].

Further sophistication of the model is possible, for example by assigning individual values of the spring constants E_s^i dependent on the position of the fibres. The breaking process of a fibre is a probabilistic event, fluctuations around the average behaviour will therefor always exist.

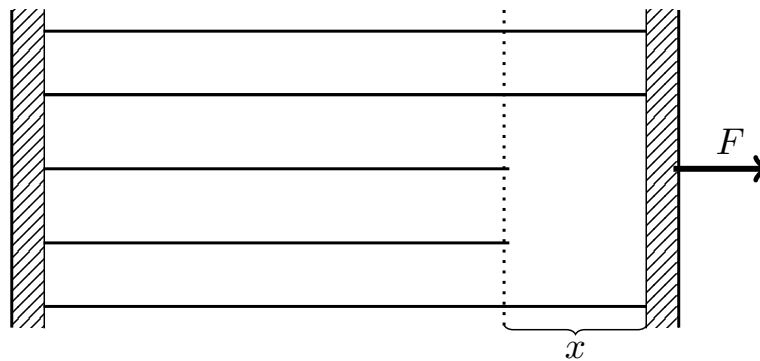


Figure 2.5: Illustration of a traditional FBM under an external tensile load F , adapted from [1]. One support is fixed whereas the other support have been shifted a distance x by F . This have caused failure of some fibres. The combined Hookean forces of the intact fibres balance F .

⁴In the literature often set to one for simplistic reasons.

2.3.1.1 FBM and scaling relations

A strength of FBMs is their ability to identify scaling relations among the variables of an experiment. An example is the power law dependence of avalanches. An avalanche is defined as the simultaneous breaking of fibres in a bundle. It is a direct effect of correlated fluctuations. The expected asymptotic distribution $D(\Delta)$ of total number of avalanches of a given size Δ is given by a power law dependence

$$\frac{D(\Delta)}{N} \propto \Delta^\Lambda, \quad (2.9)$$

where the value of Λ was determined to $\Lambda = -\frac{5}{2}$ of a LLS model of Hemmer and Hansen in 1992 [19].

2.3.1.2 FBM and creep experiments

The relations between traditional FBM and creep have been extensively studied [20]. In a FBM model describing creep a two state description of the fibre state is no longer realistic. Such a fibre should have the ability to be damaged without complete failure in such a way that the damaged fibre contributes to the bundle strength with a reduction in the elastic constant of some factor a . The load on a fibre i is then changed from σ_i to $a\sigma_i$.

A creep experiment can be stress or strain controlled. A strain-controlled experiment use the strain ϵ as the independent variable. In such a case burst of the first fibre will cause a sudden decrease in the elastic force at the value of x . The proportionality constant is smaller because the number of intact fibres is less than N . In a stress-controlled experiment one slowly increase the applied force F in such a way that the stress σ , given as the external force on each fibre $\sigma = F/N$. The extension of a fibre increases instantaneously while the bundle force remains constant at the breaking point. After the failure of one fibre the extension again increase linearly with the force.

This form of load sharing differs from the previous described ELS because the stiffer fibres of the bundle receive a higher load. Several local-load-sharing mechanisms are also possible [1, Chapter 7].

2.3.2 A first implementation of a particle based FBM

The creep modification and eventual failing of polymeric materials has recently been described by a computational approach by Linga et al. [4]. In their study, they constructed a FBM in which the structure and dynamics of polymers chains were given an explicit representation.

This approach, that in what follows will be labelled as '*particle based*' FBM, is in many ways intermediate between a traditional FBM, and the standard molecular dynamics approach widely used

in computational investigations of condensed matter systems.

To ease computations and to give their results a paradigmatic role, Linga et al. adopted a rather idealised model in which polymer beads interact with each other only along the polymer backbone while inter-chain interactions are neglected.

Two variants of the basic model have been identified, allowing and disallowing the recombination of broken chains.

In this way a number of real-life effects have been reintroduced into the model, such as interacting chains.

The elongation process as a function of normalised time gave hints of an universality process explained by a one-step FBM in the model allowing recombination. A power law dependence of the bundle lifetime $\tau \sim F^{-\gamma}$, $\gamma = 4 \pm 0.1$ was presented for chains disallowing recombination.

2.4 Biobundles

Mechanical forces plays an essential role in cellular processes. Muscle contraction and extension, cell rolling, red blood cell deformation, division and fusion, endocytosis and exocytosis, spreading adhesion, locomotion, endocytosis, and exocytosis are important examples [10, 13, 21–23].

Similarly with what happens in industrial mechanical systems, force transmission in cells is often carried out by fibrous materials, whose microscopic organisation is recognisable as a bundle. In fact, there exists a lot of biopolymeric bundles in nature, that self-assemble through the usually complex pathways of biochemistry. Their formation and stability depend on the intra-and inter-cellular environment, according to equilibrium conditions and kinetic constraints.

However, the recent literature has focused primarily on single-molecule experiments and on biomolecule networks (gels). With increasing sophistication of the experimental and computational methods, it is reasonable to assume that the bundle structure will receive the attention it deserves, for the roles it plays in cells and for the many potential applications in bio-nano-technology. A first review on the properties of biopolymer bundles has appeared recently [24]. A short description of how one generates a biopolymeric bundle and the most important methods to measure their properties is given in the following.

2.4.1 Building a macromolecule

A biopolymeric macromolecule is generated through the process of polymerization starting from a substance of much simpler molecules. This can occur spontaneously within a cell, or it can take place through artificial synthesis process, sometimes very complex. Most biopolymers, are frozen into their

polymeric form, that normally doesn't change with time.

A special role among biopolymers is played by the so-called living polymers (i.e., actin, tubulin,...), whose polymerisation instead is an equilibrium process. Properties of living polymers, including living bio-polymers, have been reviewed by Greer et. al. [25]. Their short review presents results on sulphur, α -methylstyrene and actin, whose polymerisation is seen as a equilibrium polymerisation and second-order phase transition of the $n \rightarrow 0$ universality class.

New advances in the technology have broaden the scope of investigations of the non-equilibrium thermodynamical case. In this picture the assembly rates of the systems are of key importance [26].

The main processing techniques to generate biopolymeric bundles for experiments at the nanometer scale are: *self-organisation* and *electrospinning*.

2.4.1.1 Making nanobundles

The primary approach to generate nanobundles is represented by self-organisation, which happens in a disordered system with pre-existing components that form an organised structure often out of equilibrium conditions. Pattern formation in reaction and diffusion systems is an example of that [27]. Protein folding or phase separation of lipids and proteins due to macromolecular interactions are further examples concerning biopolymers.

Electrospinning is a technique to form minute fibrous structures using the electrostatic repulsion of polymer jets emitted from a micro-metric nozzle. The method allows the preparation of fibres of ~ 100 nm diameter. Electrospinning of proteins has been performed mainly on collagen, gelatin, elastin, and silk fibroin [28, 29].

Structural DNA nanotechnology is a specially important self-assembly technique. It aims to control the hybridisation, temporal and spatial *three-dimensional* (3D) structure of the components of nucleic acid at the finest possible level [30]. The field is based on an original idea proposed by N. C. Seeman in 1982. He suggested that one can use DNA as a physical material for the self-assembly of structures at the nanoscale [31]. This technique can arrange the DNA strands into large *two-dimensional* (2D) and 3D periodic lattices at the molecule level. DNA bundles can be assembled from only oligonucleotides or by the DNA origami concept with the help of a long single-stranded scaffold. Figure 2.6 shows a happy DNA 2D-lattice fabricated by a self-assembly process.

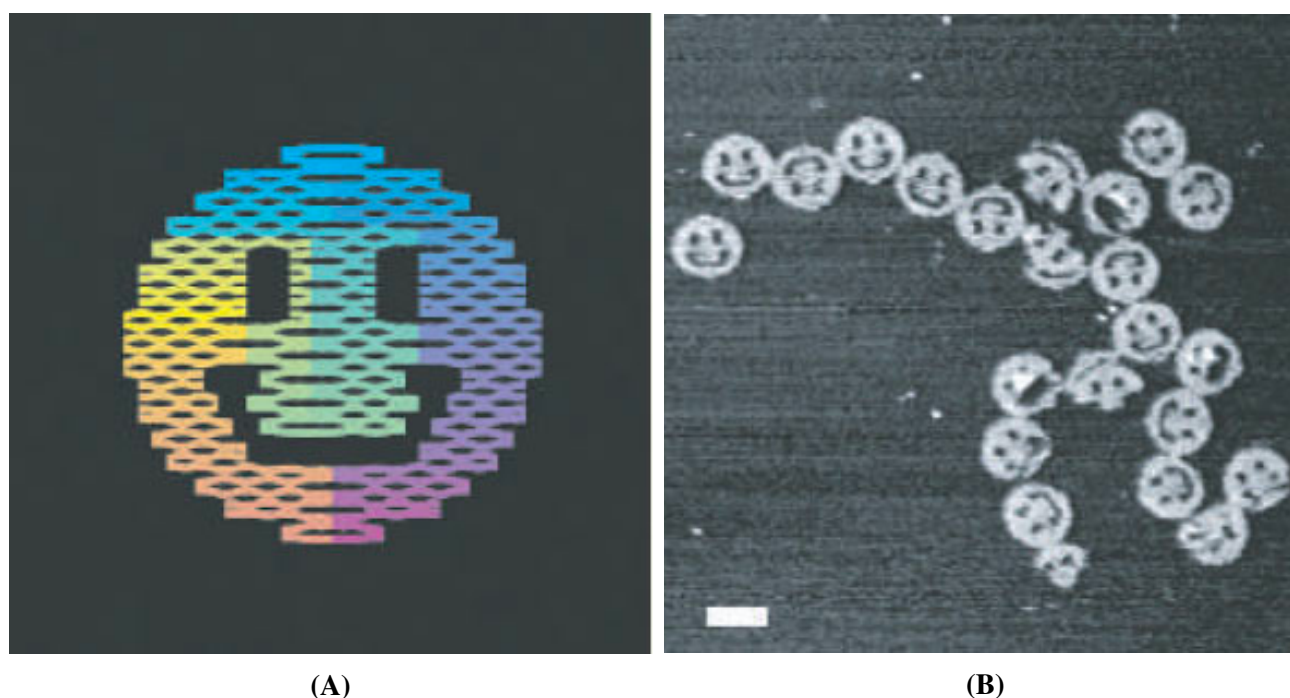


Figure 2.6: The happy face of bio-nano-technology. DNA in the form of smileys fabricated from a self-assembly process adapted from [32]. Figure 2.6A shows the folding path to make a DNA ‘smiley’. Figure 2.6B shows an AFM microscopy image of the finished product. The scale bar is 100 nm.

2.4.2 Experimental methods

“There’s plenty of room at the bottom.”

– R. Feynman, *Lecture given at California Institute of Technology, 1959*⁵

The structure of individual cell organelles were historically first recognised in optical or electron micrographs and then isolated through biochemical work [34]. Our main interest in this thesis is the connection between the micro- and macroscopic picture in biopolymeric bundles under external tensile loads. Experimental measurements on these kind of systems requires access the ‘bottom level’ of nature, represented by the atomistic and molecular scales. The advanced techniques for the manipulation of single molecules at the nanolevel had their dawn in the 1980s.

2.4.2.1 Fibre diffraction

The oldest weapon of choice to investigate the structure of fibrous molecules is X-ray fibre diffraction representing a specialised version of the widely used X-ray diffraction of crystallography. Such an instrument projects a beam of X-rays towards a sample. Scattered rays indicate the molecule structure by forming a diffraction pattern, i.e. a Fourier transform of the electron density, on a photographic

⁵Feynman offered a prize of \$1000 to the first person that could make an operating electric motor at the size of 1/64th inch cubed. The challenge was solved by the electrical engineer W. H. McLellan in November 1960. This challenge has been regarded by some as an inspirator of the development of nanotechnology [33].

film. Chains arranged in the same orientation produce a similar scattering effect, thus the greater percentage of crystallinity the better picture of the sample [35]. X-ray measurements are routinely carried out at synchrotron radiation facilities. The data analysis is a crucial part of the experiments. The method is most famous for the characterisation of the helical structure of DNA performed by Franklin, Crick and Watson in 1953 [36].

2.4.2.2 Microscopy and fluorescence

Microscopy comes in two main varieties, optical microscopy and electron microscopy. Arguably, optical microscopy represented the first scientific observational approach enhanced by advanced (for the time) technology. By and large, its resolution is limited by the light wave length, that at ~ 500 nm is much longer than the linear size of the structures one wants to observe and to measure. It remains one of the main observational tools at the scale of cell, or major cellular organelles.

The power of optical microscopy is enhanced by fluorescence techniques, based on the addition to the system of suitable chromophores, able to stain selected spots on macromolecules and on cells. The time dependent distribution of chromophores can be measured and recorded by probing the sample by a laser beam that excites chromophores' luminescence.

The resolution of electron microscopy is limited by the ability to control electron beams in space, and it reaches down to a fraction of nm. As such, it is suitable for observing the ultra-structure of cell down to virtually molecular resolution. An important parameter to judge the resolution of an electron microscope is the energy of its electron gun.

2.4.2.3 Force spectroscopy

Single Molecule Force Spectroscopy (SMFS) are techniques that allow direct manipulation of the single molecule level. The measured force or extension of the molecule is proportional to the displacement of the probe holding the molecule, but all instruments have individual precision and accuracy due to distinct stiffness constants and pulling mechanisms [37].

The bonds that connects the surface of the sample and the probe, the temperature of the surrounding environment, mechanical vibrations, air currents, acoustic, and electrical noise could impact the measurements [38]. Current manipulation of single-molecules are precise over six orders of magnitude in length and force⁶. The most common SMFS tools today are *Atomic Force Microscope* (AFM), *Optical Tweezer* (OT) and *Magnetic Tweezer* (MT).

⁶The current manipulation of single-molecules spans a range of 100 pm – 100 μ m in length and a range of 0.01 pN – 10 nN in force [38].

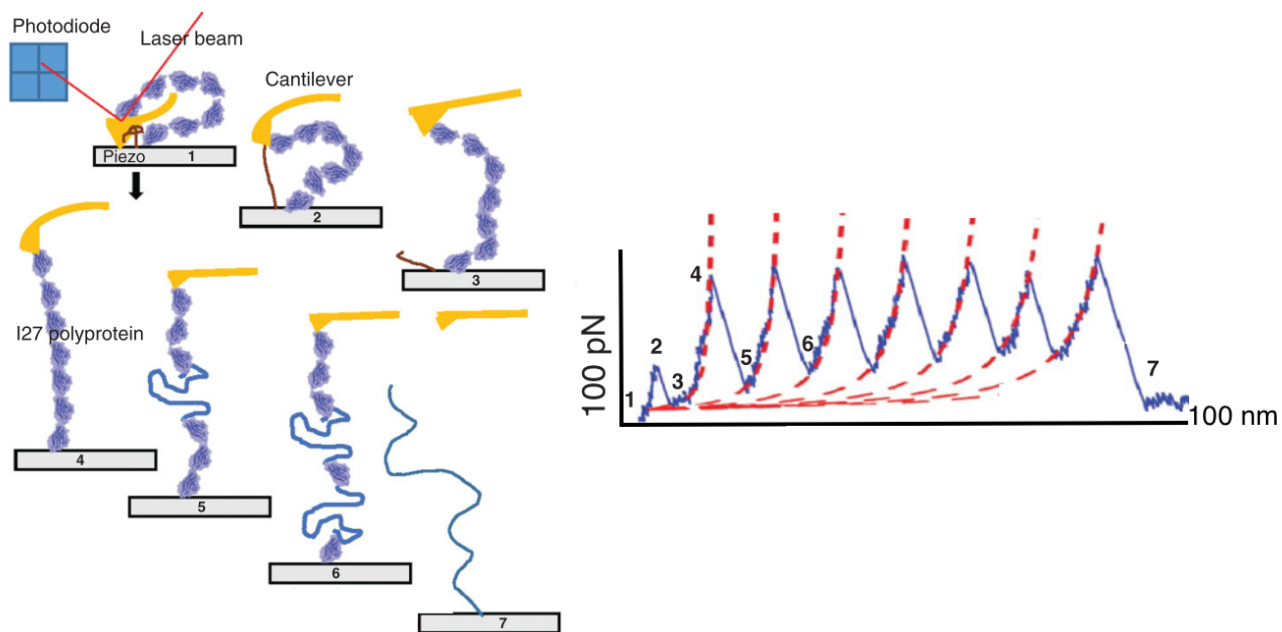


Figure 2.7: A schematic illustration of an AFM unfolding the polyl27 protein, adapted from [10]. Left: The unfolding process of different regions in the protein. Right: The measured force extension curve. Each saethooth-peak corresponds to the unfolding of an individual folded domain.

2.4.2.3.1 Atomic force microscope

AFM is a mechanical surface sensing technique ideal for studying strong inter- and intra-molecular interactions in single molecules [37, 39]. It measures forces in the pN range and can operate in liquid environments at a chosen temperature. The AFM tip approaches and retreats from the sample surface in a controlled manner. One can acquire two sorts of information from an AFM: topographical images and force measurements [3]. The rupture location of the molecule in a force measurement is recorded by the deflection of the cantilever spring [40]. A schematic representation of an AFM unfolding a chain molecule is shown in Figure 2.7.

2.4.2.3.2 Optical tweezer

OTs have an excellent resolution suitable to study mechanical properties of biopolymers in the low-force regime, $F < 100$ pN, typically not accessible for an AFM [10]. The instrument optically traps one end of the sample with a laser focus and sucks the other end through a micro pipette. A highly focused laser beam provides an attractive or repulsive force to measure the 3D displacement of the trapped sample with a time resolution of ms. Exerted forces and torques on individual molecules are in the pN – μ N order. The spring constant in the measurement depends on the focus of the laser and on the dielectric constant of the trapped object. A drawback with the use OTs is the potential danger of damaging the sample by the heat from the laser [38].

2.4.2.3.3 Magnetic tweezer

MTs have the ability to apply torque and mechanically coil/uncoil a tethered molecule. The instrument generates a magnetic force field that induces a moment proportional to the field gradient over the sample. If the gradient is steep, one can achieve high forces with a relative small magnetic field. The generated force can be approximated as constant over the length scale where the tethered bead moves. The resulting torque exerted on the beads is in the order of $10^4 - 10^5$ pN nm rad⁻¹. It is likely that the development of the instrument will include a high resolution camera and a large scale parallelism that allows simultaneous measurements on as many molecules as $10^2 - 10^3$ [41].

2.4.2.4 Modern *in vitro* tools

Microelectromechanical systems (MEMS) or *in vitro*⁷ 'lab on chip' instruments are the newest technology devices to mimic the microenvironment of cells by controlling the mechanical strain [2]. They are divided into hard silicon-based devices and systems made of soft polymers and gels [42] and are mainly used to study the mechanics of the single cell. A majority of such instruments cannot mimic the 3D micro environments that cells experience *in vivo*⁸.

⁷A biological process occurring in a controlled experimental environment rather than within a living organism.

⁸A biological process occurring in a living organism.

3 | POLYNUCLEOTIDES

The most famous examples of functional polynucleotides are DNA and RNA. Even though the helical structure of DNA was discovered in 1950s we still lack a complete understanding of its properties. The human body is made of 60 trillion cells each containing 2 m of genomic DNA. To pack DNA into eukaryotic cell nucleus the molecules typically undergoes a length compaction of $10^4 - 10^5$ times. The remarkable compression is made possible by protein-DNA-interactions giving origin to chromatin, an important example of a polynucleotide in a closely packed phase.

Stretching experiments on polynucleotides have focused on unravelling the force-extension curves and the underlying mechanics of the unfolding process of the double helix of DNA. How cells and organelles respond to bio-mechanical signals is under investigation, but not properly described. Experiments investigate how the movement of eukaryotic cells is coupled to deformations of the nucleus, and how mechanical forces affect the reproduction of cells. The development of new measurement techniques, such as structural DNA nanotechnology, have made important contributions to the field.

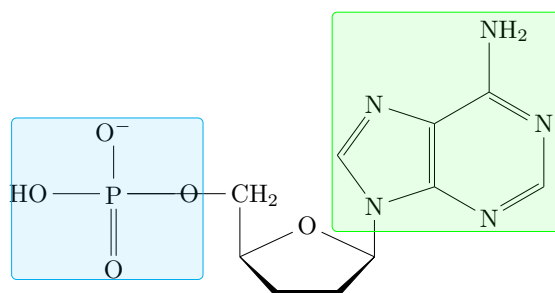
A brief outline of the structure of polynucleotides and of polynucleotide bundles is given in the following section. Further sections and subsections review experiments identifying the mechanical response of polynucleotides to an external force.

3.1 Molecule structure

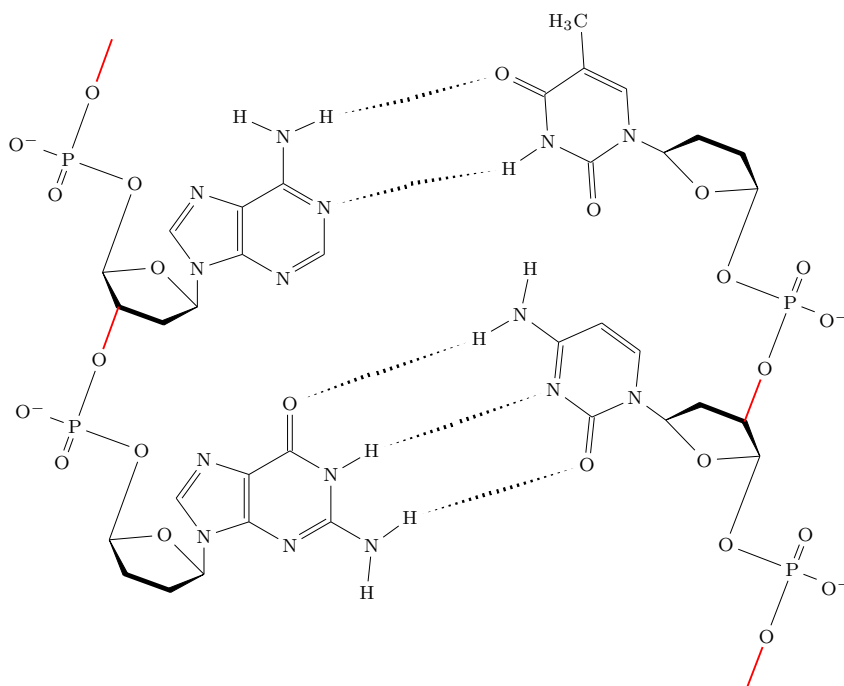
The chemical structure of a mono and polynucleotide is given in Figure 3.1. Nucleotides represent the monomeric building block of polynucleotides, and consist of a phosphate group and a nitrogen base attached to the five carbon (pentose) sugar. The negatively charged phosphate-sugar backbone are joined together by covalent bonds between the third carbon of the pentose ring and the phosphate group of the next nucleotide. The helical structure of DNA originates in hydrogen bonds between chains. RNA molecules usually adopt a single strand configuration, but fold into tertiary structures of the same helical symmetry driven by a similar mechanism. The genetic information in eukaryotic cells is stored in the cell nucleus.

3.2 Force-displacement curves

Stretching experiments performed in the early 90s focused on understanding the mechanical response of a denatured *double strand-Deoxyribonucleic Acid* (ds-DNA) into *single strand-Deoxyribonucleic*



(A) Deoxyadenosine monophosphate as an example of chemical structure of a monomeric unit in a polynucleotide. The phosphoric acid is indicated in blue, the pentose deoxyribose in black and the nitrogenous adenine group in green.



(B) Schematic overview of the chemical structure of the polynucleotide DNA in courtesy of [43]. The phosphoester links between the phosphate-sugar backbone are indicated in red.

Figure 3.1: Schematic overview of chemical structures of a mononucleotide (Figure 3.1A) and a polynucleotide (Figure 3.1B).

Acid (ss-DNA) [15, 44, 45].

The first reported stretching experiment on DNA was performed by Smith et al. in 1992 [15]. They investigated a single DNA molecule with length $l_0 = 16.2 \mu\text{m}$ tethered to a surface. The tethered beads were subjected to various combinations of magnetic and hydrodynamic forces, typically not greater than 1 pN. Using standard hydrodynamics model, the authors proved that a geometric parameter (the angle θ , in [15]) grew monotonically with increasing value of the applied force F . This one-to-one correspondence allows to estimate F from optical measurements of α . The experimental approach required a difficult calibration, because the effect of the viscous drag on the molecular motion depended on the position within the experimental cell. Once fully validated, the strain versus stress curve obtained from experiments did not match the predictions of the FJC model. A better match was achieved with the WLC model, suggesting that DNA behaves like a continuous flexible

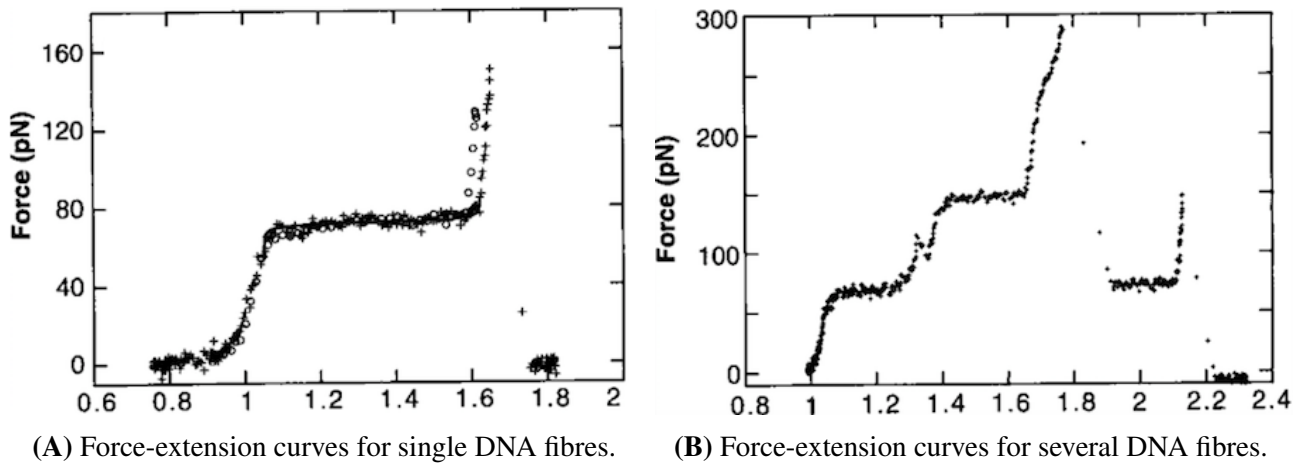


Figure 3.2: Force-extension curves for single DNA fibres (Figure 3.2A) and several DNA fibres (Figure 3.2B) adopted from [44]. The force profile for the single fibre is monotonic with one plateau followed by a steep drop. In comparison, the force profile of the bundle displays several plateaus.

chain.

An important observations was made by Cluzel et al., reporting that the force-displacement curve had a plateau around $F = 70$ pN, corresponding to a length $l_t = 1.7 \cdot l_c$ [44]. An illustration of the surprising result is given in Figure 3.2. The force-extension curves points towards a phase change of the DNA state. The phase transitions was explained by a two state model with an energy difference ΔE .

The paper by Smith et al. [45] also report the first observations of bundle effects in stretching experiments of polynucleotides.

Current research appears to validate that the DNA molecule will adopt different regimes under a tensile load. Under low forces, ($F < 10$ pN), the molecule encounters an entropy dominated regime. Under intermediate forces, ($10 \text{ pN} < F < 70$ pN), the molecule undergoes a Hookean regime where it stretches like a spring. At large forces ($F > 70$ pN) the molecule is extended by a large amount and the DNA undergoes structural transitions.

The presence of cations in a DNA solution is crucial for the mechanical unzipping of the helix [46]. Measurements of the DNA elasticity have turned out to be the most precise way of determining the persistence length of the molecule [47].

Stretching experiments performed on RNA have revealed the same two state form of the force extension curves as seen in DNA [48]. Collin et al. repeatedly measured the mechanical work associated with the unfolding and refolding of a small artificial RNA molecule [49]. They illustrated how non-equilibrium force measurements on single-molecules can provide equilibrium information, such as the free energy, for the folding process.

3.3 Torsional constraints

Pulling DNA without constraining the molecular torsion results in a deformation that consist of a combination of twist and stretch. Some experiments apply the external load on DNA while keeping fixed the orientation of the two chain terminations. Unfortunately, current research does not give a sufficiently discussion of how the local structure of the DNA responds to mechanical forces under a torsional constraint.

Nevertheless, results on stretching DNA while constraining the global torsion are available. Rotor bead tracking experiments have shown that DNA reaches a maximum twist at $F \approx 30$ pN before it overwind [50].

King et al. showed in 2016 that DNA under torsional constraints display a heterogeneous and rich plasticity as the applied tension is increased. They suggested that these structural rearrangements make it possible for of the genomic DNA to absorb changes in torsional constraints imposed by the surrounding environments [51].

3.4 DNA origami

DNA origami is a structural DNA nanotechnology based on DNA bundles. Joining multiple helices allows the creation of stiffer structures where the bending rigidity increase and the torsional rigidities are augmented moderately. Kauret et al. measured the bending and torsional rigidities of four- and six-helix bundles assembled by DNA origami in 2011 [52]. The structures were made of 4, 6, 18 and 20 helix bases with molecule length in the range of 450 nm.

3.5 The cell nucleus

The nucleus of eukaryotic cells contains the chromatin made of DNA and associated protein. How cells move in tissue is a central question in research on cancer and other diseases. Metastasis is the spread of cancer cells to new areas of the body, that requires migration through tissues. Recent experiments published within the last decade shows a direct link between nucleus and the 3D movement of cells. The experiments on deformation of the nucleus during migration have just recently begun [53].

3.5.1 Mechanical properties of whole cells

Mechanotransduction is the name of various mechanisms that convert mechanical stimuli into electrochemical signals in the cell [54]. The external environment of the nucleus is felt through the

cytoskeleton [55]. The nuclei of healthy cells are typically an order of magnitude stiffer than the cytoskeleton of the cell whereas the nucleus of metastatic cancer have abnormal shapes and stiffness.

Isolated nuclei respond to force by adjustments of their stiffness under applied tension. Guilluy et al. have shown that isolated nuclei can respond to force by changing their rigidity within seconds [56]. This suggests that nuclei can modify their rigidity whether the tension is applied on the cell or generated within the cell itself. Further work is required to precisely determine how nuclear mechanotransduction is regulated.

The diameter of pore sizes encountered during cell invasion range from 0.1 to 30 μm , comparable and smaller than the size of the migrating cell [9]. The nucleus contain the genomic information of the cell and is the site that houses DNA replication, transcription and processing of RNA. Mechanical forces and deformation during migration in space can impact the cellular function and viability. It is still not known if the mechanical stress during 3D migration is sufficient to damage the DNA. This is an interesting question for the future.

These observations point to the crucial role of mechanical properties in the functioning of healthy and diseased cells. Quantifying the molecule basis of these behaviours will open the way to innovative bio-medical approaches.

3.6 Chromatin

Chromatin was discovered in 1880 by W. Flemming. The later discovery of DNA made chromatin relevant as a carrier of the genetic information of cells [57]. The basic unit of chromatin is the nucleosome, a short DNA segment of 200 *Base Pair* (bp)¹ wrapped around a core of eight histone proteins [58]. In the cell cycle chromatin undergoes both condensation and decondensation processes.

The nucleosomes impacts the packing, replication, transcription, and repair of the DNA. How enzymes are able to access the gene information within this structure is still under debate [59].

3.6.1 Transitions during stretching

The force-extension curves produced during unwrapping of DNA from the histone linker and the measured force to break chromatin are surprisingly close to the force measured to break DNA [60].

Single and intact chicken erythrocyte fibres were studied with tweezers by Cui et al. in 2000 [61]. The required force to remove the core particles from the native chromatin was then 20 pN or higher. The observed force-extension curves clearly exposed a two state behaviour thus connecting transition between two phases to the value of the external force. The transition between the two states occurred

¹ 1bp \approx 3.4 Å.

when the work performed by the external force was equal to the difference in the chemical potential between the phases. An explanation of how a fiber could acquire the ability to interconvert between a condensed short state and a decondensed long state was required. An explanation is required also for the correspondence of the measured force with the plateau at ~ 65 pN in the DNA force-extension curves. Extension beyond 20 pN within a stretching cycle resulted in irreversible changes of the fibre. These features were explained by the possible lack the histone linker.

A later experiment determined the required force to unwrap DNA from the histone to be 20–40 pN [62].

3.6.2 The 30 nm-fibre

The two most important models to describe the chromatin fibre are the solenoid and the zig-zag model [6].

Much of the current debate revolves around whether or not the 30 nm-fibre exists or not. It is evidence that isolated from the nucleus chromatin tends to adopt a fibre-like conformation that resemble some kind of bundle structure [34, 60].

Maeshima et al. proposed that nucleosome fibres in the mitotic chromosome bulk does not form 30 nm chromatin fibres, but exists in an interdigitated state locally similar to a polymer melt with dynamic movements [57].

*In situ*² observations of nuclei by *Transmission Electron Microscopy* (TEM) have given results where chromatin appears with non obvious fibre-like properties [34].

Measurements indicate that chromatin unfolds by adopting an open ended beads-on-a-string conformation with all the internucleosome contact lost [7]. A separate modelling performed later confirmed that a plateau is observed during fibre unfolding where all the nucleosomes remained intact. Chromatin at low salt concentration is reported to exist in a loosely configuration known as 'bead-on-a-string'. The compact and ordered 30 nm configuration have been questioned by some. Force spectroscopy experiments on individual chromatin fibres is achieved by fixing the position of one of the ends and stretching at a constant force or up to a fixed position.

The decondensation of chromatin leads to an increase in the nuclear size and softening. Chromatin is thought to be a part of the nucleoskeleton that control the mechanical linking of the nucleus to the cytoskeleton and makes the cell migration efficient [53].

In a recent experiment scientists tested the external membranes of hamster cells by magnetic beads [22]. By maintaining the magnitude of the force, but changing the direction and the angle there were observed a direct link with the out stretched regions in the chromatin of the nucleus. The degree

²Experiment performed in the natural or normal environment.

of stretching and gene expression were varied based on the direction of the force in relation to the cytoskeleton of the cell. The bundle did not seem to be affected when pulling in the opposite direction of the fibre.

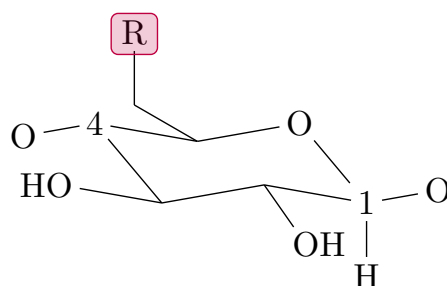
4 | POLYSACCHARIDES

Polysaccharides represents a class of materials which have renewable nature, tailorable surface chemistry, interesting optical properties, and anisotropic shapes [63]. They are generally highly solvable and easily connected to the AFM tip for stretching tests [10].

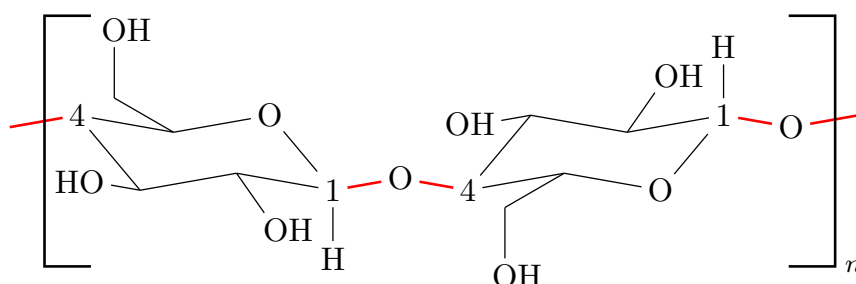
The experiments testing the mechanical properties of polysaccharides have focused on identifying the structural changes in the molecules when the sample is elongated and identifying if/how a polysaccharide component will influence the mechanical properties of a material.

Engineered *Nanocellulose* (NC)¹-materials and hydrogels have outstanding mechanical properties and are especially interesting as biopolymeric bundles.

A presentation of the polysaccharide chain structure and experiments on their mechanical properties is given in the following.



(A) The chemical structure of a monosaccharide. The pyranose ring of the glucose molecule is given in the chair configuration. Reaction group is indicated in red.



(B) Schematic overview of the chemical structure of cellulose, with a β -linkage, in courtesy of [64]. The glycosidic bonds between pyranose rings are indicated in red.

Figure 4.1: Schematic overview of the chemical structure of a monosaccharide (Figure 4.1A) and polysaccharide (Figure 4.1B). The fourth and the first carbon of the pyranose ring are indicated with numbers.

¹Cellulose is a product of the biosynthesis in plants. NC refers to processed materials or cellulosic extracts with structural dimensions at the nanoscale [63].

4.1 Molecule structure

An illustration of the chemical structure in a mono- and polysaccharide is given in Figure 4.1. A polysaccharide² is composed of saccharides linked by glycosidic bonds. The structures of the monomers are mostly 5 (pentoses) or 6 (hexoses) carbon atoms in ring configurations. The group are also known as 'carbohydrates' and is usually divided into starch, glycogen and cellulose.

A broad class of polysaccharides display isomerism where the chains have a similar molecule structure, but different biological functions. Amylose and NC are isomers of the same formula but different pyranose ring linking. Amylose is α -linked, dissolvable in water and function like an energy storage in compound plants. NC is β -linked, insoluble in water and function like a structural compound for plants.

4.2 Structural changes during stretching

The first measurements on single polysaccharide molecules were performed on the branched glucon molecules amylose and dextran under equilibrium conditions with an AFM [65, 66].

There were observed plateaus in the force-extension curves for both materials at a tensile load $F = 300$ pN for amylose and $F = 900 \pm 100$ pN for dextran. Both plateaus disappeared after treatment with periodate evincing that the pyranose ring structure's mechanical integrity must be preserved when a plateau is detected. After splitting of the pyranosering both the materials displayed identical behaviour.

These observations suggests that a force plateau indicates a transition from a chair-like to a boat-like conformation of the pyranosering [40, 67]. Today, the general consensus is that these transitions works as fingerprints for the individual polysaccharides in solution [68].

A schematic illustration of the chair-to-boat transition in a glycopyranosering is displayed in Figure 4.2.

4.3 Mechanical properties of nanocellulose

The viscosity of biological NC materials based on starch and chitin is dependent on the crystallinity of the sample.

Guhados et al. investigated this correlation by measuring the deflection across a suspended fibre of bacterial NC with an AFM in 2005 [69]. The Young's modulus of the material, independent of the

²The term 'Saccharide' means sugar in Greek.

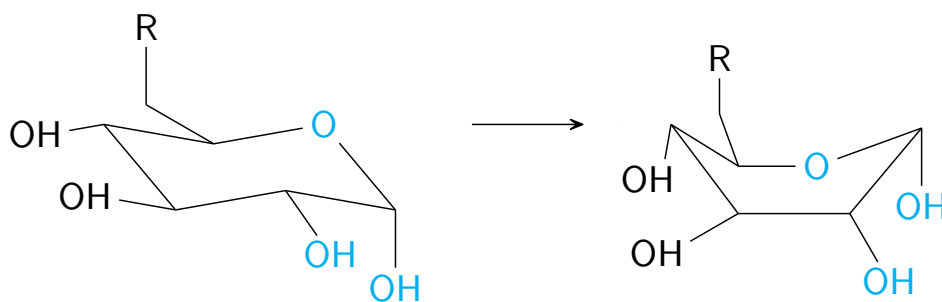


Figure 4.2: Schematic illustration of the chair-to-boat transition a pyranose ring can undergo under an applied tensile load.

material, was measured to be 78 ± 17 GPa. A value in the same range as predicted by the Voigt model indicating a homogeneous behaviour of the material.

Experiments performed on starch based foams have revealed that the mechanical properties of the foams are dependent of the cell wall and the cell structure [70]. Significant improvements in the yield strength, the plateau zone level, and the Young's modulus were demonstrated in compression tests. After enzymatic treatment 40% of the foam contained a mixture of closed and open cells. The different cell structures in the foam influenced both the linear-elastic and cell collapse region. At a low level of applied strain the elasticity was linear.

Wet-stretching experiments on rehydrated macroscale fibres composed of nanofibrillated NC and chitin showed a high correlation between the degree of alignment of fibres and the macroscale stiffness. The NC-based materials changed the original value of Young's modulus by a fourth and improved the tensile strength at maximum elongation by the double [71].

The tensile strength of polycaprolactone with a NC component also showed an improvement of more than the double in maximum tensile strength [72].

The mesoscopic assembly of NC fibrils exists in the size gap between nanocrystals and nanofibrils. Usov et al. in 2015 studied three different kinds of NC in 2015 [73]. The individual fibril and fibril bundles displayed a right handed chirality. A non-Gaussian kink angle distribution is in conflict with the accepted theory of alternating regions of crystalline and amorphous cellulose along the fibril length supporting process induced kink formation.

There have recently been suggested that the hydrophilicity of amylose are regulated by the pyranose linkage [74].

4.4 Polysaccharide hydrogels

Hydrogels are 3D polymeric networks with a high percentage of water. Potential applications of hydrogels are implantable devices, tissue engineering, control of the enzyme activity, encapsulation

substance for both food and medicine science, and wound care [75–77].

Individual polysaccharide fibrils have been identified as the microscopic origins of the distinct mechanical response in marine gels, indicating that the structural and mechanical properties of the gel are defined by the polysaccharide component [78]. Hydrogels were the first designed biomaterial used in the human body [75], even though, engineered hydrogels often lack the ordered microstructure of natural tissue and display a different response to load [29].

The hydrogel *alginate* is specially relevant as a biopolymeric bundle candidate and is extensively investigated in our department.

4.4.1 Alginate

Alginate is a marine, nontoxic polysaccharide found in seaweed. It can form a gel in physiological contact with divalent ions, often calcium, and is frequently used to structural biomimetic polysaccharide foams by freeze-drying. A majority of the capsules in medicine science are based on alginate [77].

Electrospun gelatin nanofibres of alginate have been added to brittle hydrogels to resist and strengthen crack propagation [29]. By varying the orientation of the nanofibres as multilayer laminates the elastic properties of the hydrogel was reinforced by two orders of magnitude. The greater fraction of fibres laying in the direction of the applied load, the stronger and stiffer hydrogels were generated. Hydrogels of single polymer alginate or gelatin were weak. A significant deviation in the strength was observed when the force was applied in a diagonal or transverse direction. The elastic modulus and tensile strength were respectively $E = 78 \pm 19$ kPa and $\sigma_{TS} = 19 \pm 9$ kPa for the alginate hydrogels and $E = 240 \pm 25$ kPa and $\sigma_{TS} = 10 \pm 3$ kPa for the gelatin hydrogels.

The influence of water and ethanol on the properties of alginate have been investigated [76]. Addition of low up to moderate until concentrations of 15% ethanol increased the viscosity whereas addition further than 20% reduced the intrinsic viscosity of the sample. The same trend were seen in the moduli and the stress at break. Hermansson et al. proposed that biopolymeric networks are composed of stress-bearing filaments or elastically active network of chains with a certain stiffness contributing to the overall increase in the free energy linked to the material deformation. Both the calcium and the polymer concentrations were the same through the experiment.

The *Extracellular Matrix* (ECM), a non-cellular part of tissue, providing structural support around the cells are composed of a gel. Engineered biomaterial made to mimic the viscoelastic properties of the ECM can often only display elastic response under application of external strain. Chen et al. recently showed that the viscoelastic strain and elastic recovery of a methacrylate-alginate hydrogel can be tuned by adding calcium ions to the substrate [79].

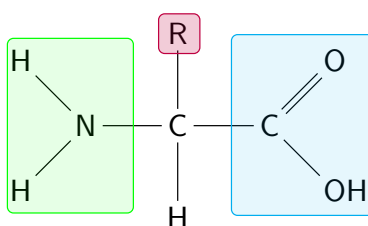
5 | POLYPEPTIDES

From a chemical point of view, proteins are the most complicated molecules we know [80, 81]. They play a major role in all aspects of cells' life, including their regulation of cells [82].

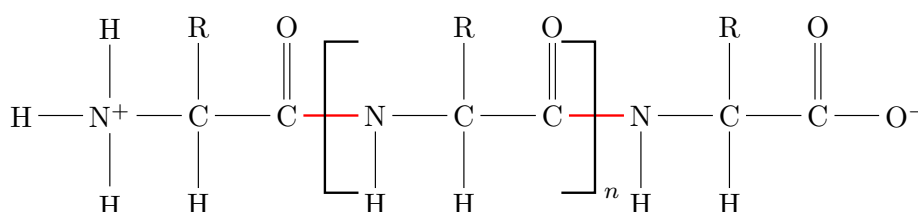
The polymeric nature of proteins, and their role in the structural mechanics of cells, make proteins ideal candidate to form bundles. Our main focus is on collagen, on amyloid fibres, and on proteins responsible for the structure and properties of the cytoskeleton. Since they are discussed in many papers, only a brief account is given of arguably the most glamorous bio-fibre of all, i.e., silk and of her close relative spider silk. In the following a presentation of the polypeptide structure and the experiments unrolling the mechanical forces that control them is presented.

5.1 Molecule structure

An illustration of the chemical structure of a mono- and polypeptide is given in Figure 5.1. The monomeric unit of polypeptides consists of an amin-group, which is a good hydrogen bond donor, a carboxyl-group, which is a good hydrogen bond acceptor, and an individual functional group. Peptide bonds link the amino group of one amino acid to the carboxyl group in another. When several amino acids are linked in a chain they form a polypeptide. Natural polypeptide chains containing between 50 and 200 amino acid residues are referred to as proteins. Many proteins, however, are made of a few peptides joined together by Coulomb and van der Waals interactions, and by hydrogen bonding.



(A) The chemical structure of a monopeptide unit. The amino-group is indicated in green, the functional-group in red and carboxyl-group in blue.



(B) Schematic overview of the chemical structure of a polypeptide. Peptide bonds are indicated in red.

Figure 5.1: Schematic overview of the chemical structure of a monopeptide (Figure 5.1A) and polypeptide (Figure 5.1B).

5.2 Collagen

Collagen is a prime construction material in biology. It is known to be viscoelastic providing mechanical stability, elasticity and strength to organisms [83]. The helical structure of collagen has been known since experiments performed by Ramachandran in 1951 [84]. The unravelling of the substructures of collagen in tissue began in the 1980s [85]. Tissue consisting of collagen, such as tendon or bones, is organised in amino acids, collagen molecules, collagen fibrils, collagen fibre and tissue [86]. The effect of cross-linkers in collagen-based materials were investigated before the effect of the single collagen fibrils [87].

The first experiment that measured the relaxation times of isolated collagen fibrils was performed by Shen et al. in 2011 [88]. They performed *in vitro* coupled stress and creep relaxation tests on type I collagen-fibrils by a MEMS device. Their results indicated that isolated collagen fibrils intrinsically behave as viscoelastic materials. A time-independent elastic modulus was determined to 140 ± 50 MPa upon initial loading of 20% strain by a Maxwell-Weichert model fit. The value dropped to 115 ± 41 MPa for subsequent loads, a trend confirmed by paired Student's t-tests.

Svensson et al. investigated the mechanical behaviour of individual collagen fibrils from human and rat loaded to failure by an AFM in 2013 [89]. Their results show that the human fibril failed at a significant higher stress than the rat fibril. The human fibrils displayed an initial rise in the modulus followed by a plateau with reduced modulus before ending with an even higher increase in the stress before failure. The differences were explained by variance in the cross-link maturity of the two tissue types.

Collagen fibrils isolated from rat patellar tendon have been investigated by *Scanning Electron Microscope* (SEM) [85]. The results gave a qualitative difference in the shape between the stress-strain curves in different tissue. Images show that the isolated collagen fibrils failed with a mechanism involving the circumferential part of the fibril, whereas the core was partially intact. It is likely that the specific location and energetics of fluid ions interacting with collagen molecules within a fibril play a central role in the mechanical behaviour. A SEM-picture of the surface of a mammalian collagen fibril at the location of fracture is given in Figure 5.2.

5.2.1 Load transfer mechanisms

A central question for collagen fibrils is if they bear the load independently or if it is transferred between them, possibly by shear forces produced during sliding. An early explanation was that crumbled fibrils would be straightened and reoriented in the direction of the applied load. This was mechanically tested in a multiscale experiment of Szczesny et al. in 2014 [90]. Their results suggested that the

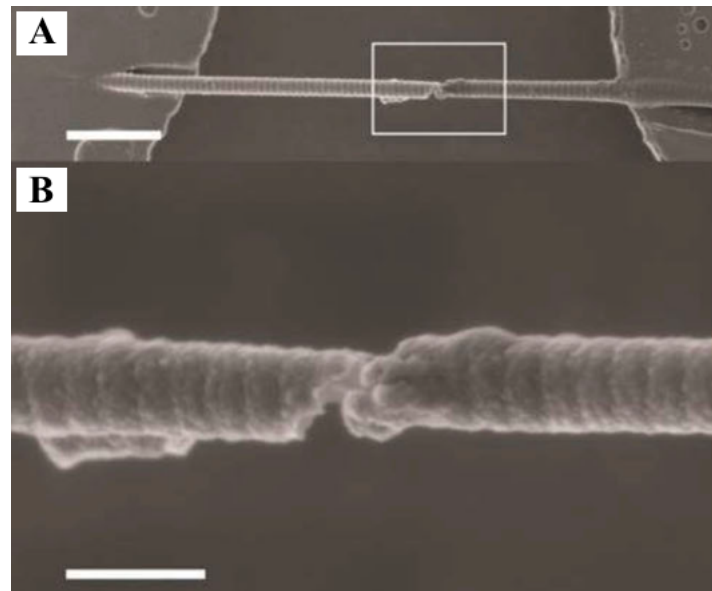


Figure 5.2: SEM image of a mammalian collagen fibril at the location of fracture in courtesy of [85]. Scale bars represent 1 μm in (A) and 200 nm in (B).

interfibrillar sliding was produced the post-yield drop in the tissue stiffness. A shear lag model based on load transfer between discontinuous fibrils could predict the microscale deformations.

5.3 Amyloids

Amyloid was initially a term to describe the iodine stained deposits seen in liver autopsies. Today the expression refers to abnormal fibrous, extracellular, proteinaceous deposits found in tissues and organs of people affected by neuro-degenerative diseases. Amyloids are insoluble and dominated by a β – *sheet* structure [91]. Spectroscopy measurements have revealed that forces required to mechanically fracture amyloid fibrils range from 300 – 500 pN. These high values are explained by the interactions within the amyloid core. The hydrogen bonding in the cross β -sheet structure, van der Waals and electrostatic forces are responsible for the resistance to unfolding of native structural motifs in proteins.

Measurements have revealed that the mechanical strength of the fibrils are very high [40]. The uncontrolled folding procedure of amyloid fibres have been connected to a number of destructive human diseases. In recent years the formation of amyloids have been placed as a central cause of Alzheimer disease, bovine spongiform encephalopathy (mad cow disease), and Parkinson’s disease [36].

Studies performed by Paul et al. in 2016 indicated a possible scaling law dependency of the measured and calculated values of Young’s modulus on chains’ length [92]. They tested a range of fibril by Deep Ultraviolet Resonance Raman Spectroscopy and AFM techniques. Their results were

compared with simulations and stress-strain calculations performed on linear and unbranched β -sheet fibrils. Theoretical and experimental results revealed that the structural and material properties of the amyloid fibrils are size dependent.

In 2017 Lamour et al. demonstrated that different amyloid fibrils of different proteins covers a broad spectrum in terms of Young's modulus and tensile strength [93]. This suggests that the difference in the mechanical properties of amyloids are caused by variations in the content and packing of the β -sheet structure within the fibril core.

5.4 The mechanics in the cytoskeleton

Microtubules, actin and intermediate filaments are the underlying bundle structures that control the mechanics of the cell's cytoskeleton. There is a strong indication that strain hardening and softening, the role of nonthermal forces, dynamic heterogeneity, and the cell's ability to move, polarise and divide are controlled by the cytoskeleton. Understanding these processes could give us a better insight in the mechanisms of cancer and other diseases [94].

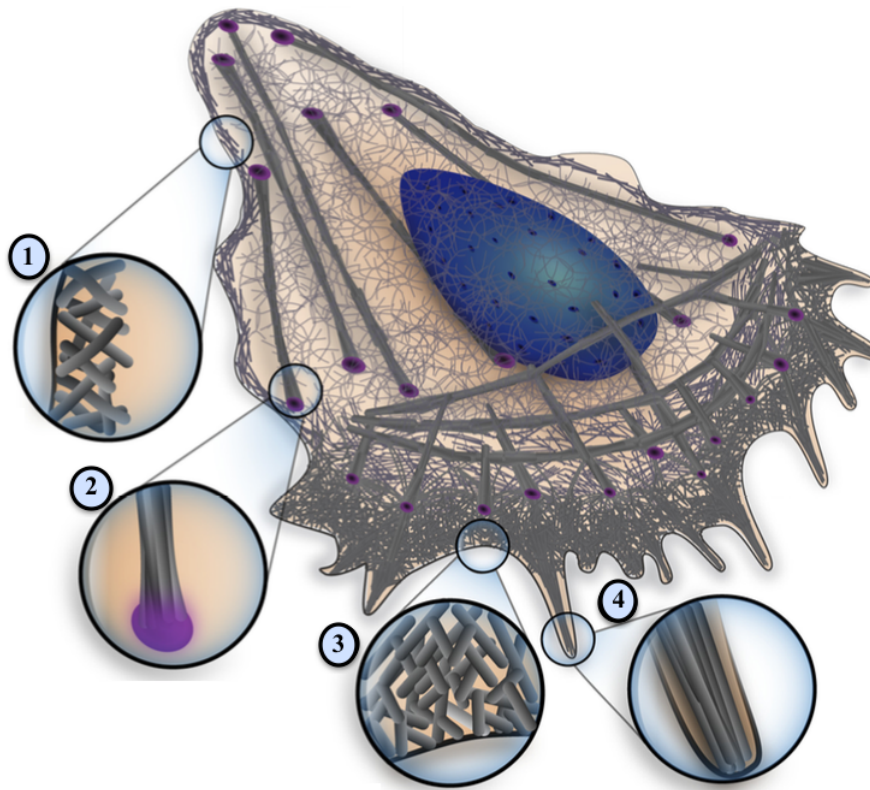
5.4.1 Actin

Actin filaments are two-stranded helical polymers built by actin proteins. They organise in linear bundles, 2D branched or cross-linked networks, parallel bundles, antiparallel structures, and 3D gels [80, Chapter 16]. The diameter of an actin filament is typically 5 – 9 nm with a persistence length of a few micrometers. Individual filaments are flexible structures that easily bend, when the filaments are cross-linked or bundled the macromolecule becomes strong. Short and stiff bundles of actin tend to stay straight under an applied force, whereas the long actin bundles display a tendency to buckle and deform.

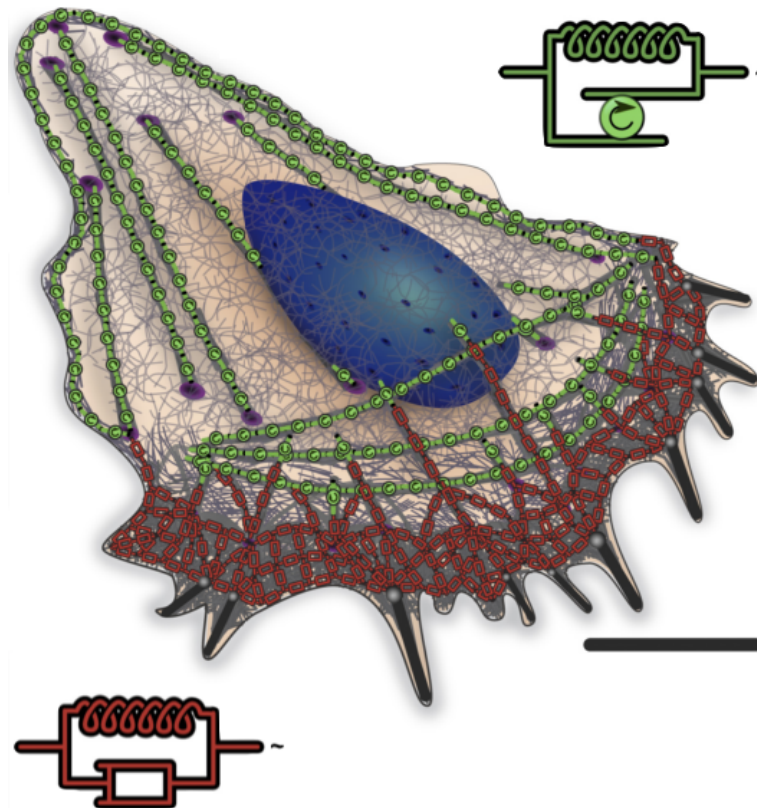
The polymerization process that occurs by noncovalent interactions when actin goes from a globular monomer to a filamentary polymer can be treated as an equilibrium polymerization [25]. The assembly process of actin is known to be under the influence of profilin, an abundant actin monomer binding, to a great extent [95]. Various experiments have tested the required rupture force for different actin arrangements. An illustration of the organisation of actin filaments in the cell and their mechanical properties is given in Figure 5.3.

The group of Ferrer et al. measured the molecular rupture forces between single actin filaments and actin binding proteins to be in the order of 40 – 80 pN by OT force spectroscopy [96].

Blanchoin et al. stated later that the rupture force for bundles depends on the type of actin binding proteins, ranging from 30 pN for α -actinin to 50 pN for filamin [95].



(A) Organisation of the actin structures in the cell. 1) Displays the cortex as crosslinked networks. 2) Shows the antiparallel contractile structures called stress fibres. 3) Illustrates the branched and crosslinked networks called lamellipodium. 4) Displays the parallel bundles filopodia.



(B) Mechanical representation of the different actin structures in the cell: areas marked with green symbols are active springs, areas with red symbols behave like viscoelastic systems of dashpots, and areas with black symbols behave like rigid rods.

Figure 5.3: A schematic overview of the actin filaments of the cell (Figure 5.3A) and the mechanical abilities of the different architectures (Figure 5.3B) adapted from [95].

In a study from 2015 Palmieri et al. compared the mechanical and morphological features of a tumour and lymphatic metastases of the same tumour. They found that the decrease in cell elasticity was accompanied by a high isotropy of actin fibres [5].

Early experiments linked the cell elasticity to the presence of stress fibres, but recent experiments have revealed that it is the total amount of actin is related to the cellular stiffness [8].

5.4.1.1 Stress fibres

Stress fibres are found in non-muscle cells and are especially interesting as a bundle structure. They are composed of 10–30 actin filaments crosslinked by α -actinin with bipolar arrangements of myosin. These bundles are responsible for fibre contraction and are often anchored to focal adhesions connecting the ECM to the actin cytoskeleton.

It is suggested that the tension or contraction of stress fibres are the exact mechanism that convert mechanical signals into biochemical signals [97].

Stress fibres are also coupled to the mechanical link between the intracellular actin bundles and the ECM [98].

One have identified at least four types of stress fibres in the cell, but a complete determination and characterisation of the morphological, functional and biological relationship between them is still lacking [99].

5.4.2 Tubulin

The term tubulin refers to the globular proteins of the tubulin superfamily or a member of this family. Tubulin proteins are assembled from six different structures. In eukaryotes the most common configuration is long, straight, and hollow cylinders of an outer diameter of 30 nm built by alternating α - and β -tubulin. Due to their cylindrical structure tubulin polymers tends to be much bigger than actin filaments [81, Chapter 34].

Microtubulin is a polar structure. The plus end of the helix is extended towards the surface of the cell, whereas the minus end is anchored near the cell centre [80, Chapter 16]. Tubulin plays an important role in determining the shape of cells and separating daughter chromosomes in the process of mitosis. Our knowledge of the growth and shrinking of microtubules is primary based on *in vitro* studies of pure tubulin.

Until 2011 one assumed that the tubulin dimers were the only substance able to form microtubules and that the chemical state of the nucleotides of the cells were crucial for the incorporation. On the contrary, observations performed in 2011 revealed that both tubulin dimers and oligomers can be

added to the microtubule ends. The chemical state of the nucleotides are not crucial for tubulin addition [100].

An experiment from 2016 have shown that the high surface density of kinesin motor proteins are capable of longitudinally splitting of microtubules into protofilament bundles. The diameter of a microfilament composed of thirteen protofilaments was 25 nm [101].

The dipole moment of tubulin have even been connected to the *consciousness* of cells [102]!

5.4.3 Intermediate filaments

Intermediate filaments are fibres with ropelike structures of approximately 25 nm length made of filaments of a large and heterogeneous family. They can form beneath the inner nuclear membran and extend across the cytoplasm, giving the cell mechanical strength [80, Chapter 16].

Intermediate filaments provides the strength needed to pull the nucleus and have the highest resistance to tensile force among the components of the cytoskeleton [9].

5.5 Spider silk

Spider silk is a natural material with remarkable properties. It is one of the toughest, strongest and most robust matter we know. The remarkable properties have been attributed to the specific secondary and tertiary structure of the silk molecule. It forms hierarchical fibrillar structures by self-assembly. Spider silk and amyloids fibrils have some degree of structural similarity. They both experience mechanical properties of similar magnitude and are both made of β -sheet structures.

Because it is possible to produce long and continuous fibres of silk it is a material ideal for mechanical investigations [103, 104]. There exists a huge interest of capturing the mechanical properties of silk to synthetic reproduce silk inspired materials.

Both the hydration level and the solvent conditions affect the silk proteins [105]. Cooperative deformation of hydrogen bonds in the tertiary structure transforms weakness into strengths in the crystalline structure [83].

A bottom-up approach on artificial bundles generated by electrospinning experiments allowed tensile testing of macroscopic artificial silk [103]. The interplay between physical β -sheet cross-linking and water-induced segment mobility of the amorphous matrix were tested on both single fibres and bundles. The β -sheet nanocrystallinities had dimensions of 5-7 nm. Figure 5.4 shows the difference in the hierarchical structure of natural and the bottom-up fabrication of engineered spider silk.

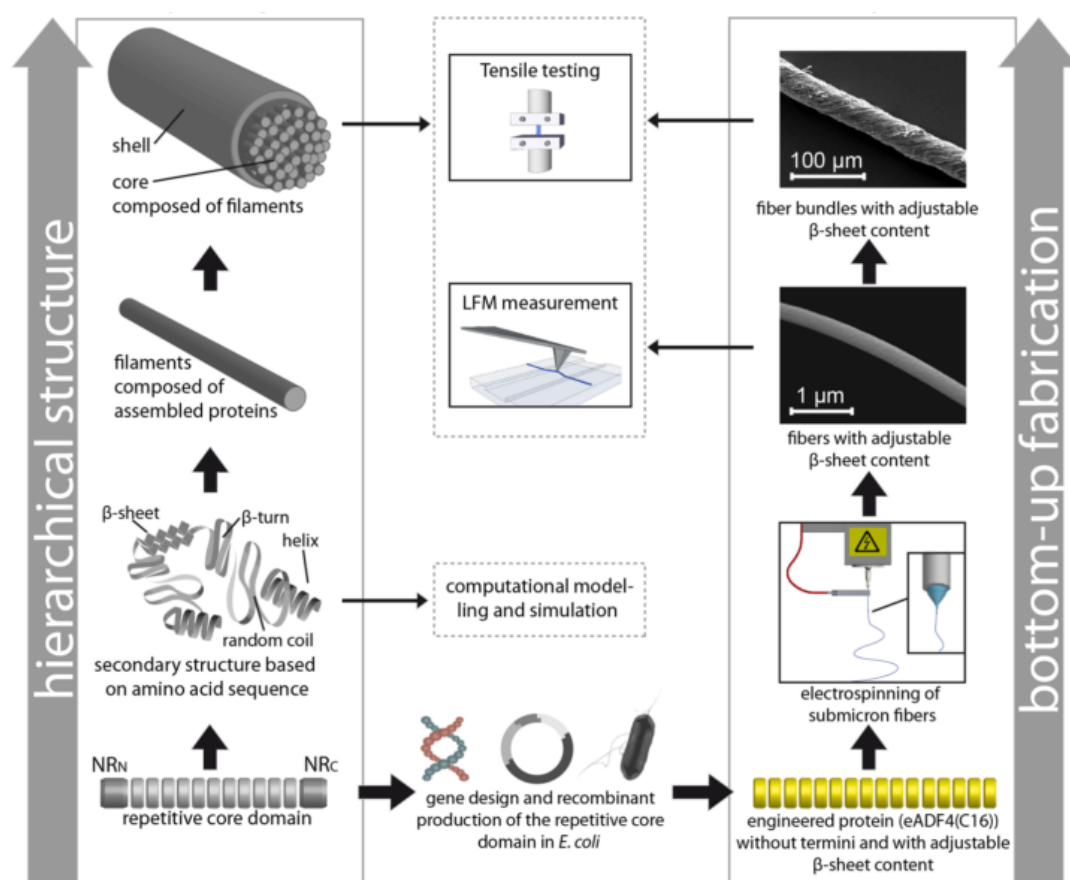


Figure 5.4: Hierarchical structure of natural and the bottom-up fabrication of engineered spider silk adapted from [103].

6 | MOLECULAR DYNAMICS

MD is a simulation technique that reproduces the time evolution of coordinates and momenta of N interacting classical particles by numerically integrating the corresponding Newton's equations of motion.

General concepts and methods of statistical mechanics connect the instantaneous and/or average value of phase-space functions to quantities such as density, pressure, temperature, etc. that are relevant on the macroscopic scale.

MD implementations require the definition of a potential energy surface as a function of the particle coordinates [106, Chapter 4].

Models for the potential energy surface, also known as *force fields*, may describe the system in atomistic detail, or they may adopt a more coarse grained point of view [107]. Methods relying on the computation of energy and forces by quantum chemistry (*ab-initio*) approaches arguably represent the most sophisticated and certainly the most expensive way to define the potential energy surface.

Needless to say, the success of MD is largely due to the amazing progress of computer facilities that has taken place during the last thirty years. State of the art methods and top computer facilities now allow the simulation of systems made of $\sim 10^6$ particles (with Coulomb charges) at the rate of 20 ns per day.

6.1 Numerical algorithm

Newton's equations of motion enjoy a number of geometrical properties that simplify their numerical integration, provided the computational algorithms reflect these same properties. The simplest and most useful property is that for a time independent Hamiltonian the total energy is a constant of motion. A similar property holds for the angular momentum of an isolated system in an isotropic medium. More in general, Liouville theorem applies to the flow of representative points in phase space [108, Chapter 9]. Computational algorithms reflecting this same property seem to enjoy decisive advantages with respect to the methods that violate Liouville's theorem.

To choose the best numerical algorithm for a given problem one should consider:

- **Efficiency:** does the algorithm scale favourably (i.e., nearly linearly) with the size N of the system? At present this is the most relevant issue, since for systems of 10^6 particles linear and quadratic scaling differ by a factor of 10^6 in their computational cost. *Central Processing Unit*

(CPU) memory is seldom an issue, while surprisingly disk space might be a problem, since for large systems simulation trajectories might occupy a vast amount of disk storage.

- **Stability:** Is the energy conserved on a long term basis for systems having a time-independent Hamiltonian? Is the integration scheme stable for different values of the parameters?
- **Simplicity:** Is the scheme easy to implement?
- **Preservation ability:** Hamiltonian dynamics is symplectic, i.e. volume and area preserving, so should the algorithm also be.

An observable in a MD-simulation is measured by expressing it as a function of particle position and momenta, set up an initial configuration for the system of interest, assign initial velocities to all particles, and prepare the sample under investigation at equilibrium. The algorithm repeatedly compute the interatomic forces between particles and the forces caused by the chosen potentials until the results are satisfactory. A flow chart of the essential steps of the MD algorithm is given in Figure 6.1.

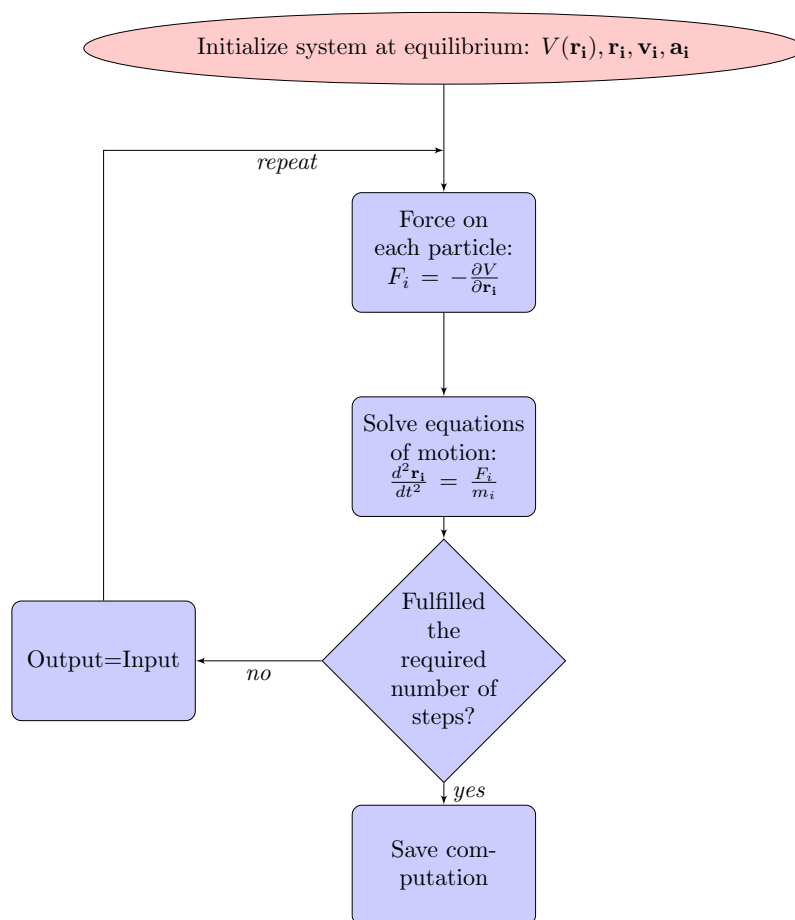


Figure 6.1: Typical flow chart of a MD algorithm.

Requirements for a MD-simulation are comparable to those of real experiments: one must prepare the numerical 'sample' carefully at equilibrium conditions, the duration of the measurements must be

long enough to give a satisfactory picture of the average behaviour in the system, or one can easily measure a different effect than one thinks [106, Chapter 4].

6.1.1 Verlet algorithms

The Verlet algorithm is usually the best choice of integration scheme for a MD-simulation. It is simple, long-term stable and has a low computational cost. The original method has been used to solve stiff differential equations since the late 18th century. Verlet introduced the algorithm in the context of MD in the late 1960s [109].

The scheme identifies the first and second derivative of the position coordinate \mathbf{r} as velocity $\dot{\mathbf{r}} = \mathbf{v}$ and acceleration $\ddot{\mathbf{r}} = \mathbf{a}$ by expanding the position coordinate of particle i in time:

$$\begin{aligned}\mathbf{r}(t + \Delta t) &= \mathbf{r}(t) + \mathbf{v}(t)\Delta t + \frac{1}{2}\mathbf{a}(t)\Delta t^2 + \frac{1}{3!}\mathbf{r}^{(3)}(t)\Delta t^3 + \mathcal{O}(\Delta t^4) \\ \mathbf{r}(t - \Delta t) &= \mathbf{r}(t) - \mathbf{v}(t)\Delta t + \frac{1}{2}\mathbf{a}(t)\Delta t^2 - \frac{1}{3!}\mathbf{r}^{(3)}(t)\Delta t^3 + \mathcal{O}(\Delta t^4).\end{aligned}\tag{6.1}$$

Taking the sum side by side of the two expressions in Eq. (6.1) one obtain expressions for the next time step in position and the current time step of the velocity:

$$\begin{aligned}\mathbf{r}(t + \Delta t) &= 2\mathbf{r}(t) - \mathbf{r}(t - \Delta t) + \mathbf{a}(t)\Delta t^2 + \mathcal{O}(\Delta t^4) \\ \mathbf{v}(t) &= \frac{1}{2} [\mathbf{r}(t + \Delta t) - \mathbf{r}(t - \Delta t)].\end{aligned}\tag{6.2}$$

where the terms of order $\mathcal{O}(\Delta t)$ and $\mathcal{O}(\Delta t^3)$ cancel out. Thus Eq. (6.2) is more stable than the original expression.

Eq. (6.2) is now formulated as a 'leapfrog' scheme. The velocity at time t can only be computed after evaluation of $\mathbf{r}(t + \Delta t)$. This feature can be a problem for equations of motion that depend on the velocity. This difficulty is solved by expressing the next time step of the velocity $\mathbf{v}(t + \Delta t)$ by the acceleration:

$$\begin{aligned}\mathbf{r}(t + \Delta t) &= \mathbf{r}(t) + \mathbf{v}(t)\Delta t + \frac{1}{2}\mathbf{a}(t)\Delta t^2 \\ \mathbf{v}(t + \Delta t) &= \mathbf{v}(t) + \frac{\Delta t}{2} [\mathbf{a}(t) + \mathbf{a}(t + \Delta t)].\end{aligned}\tag{6.3}$$

Eq. (6.3) represents the mathematical expression of the so-called velocity Verlet algorithm.

6.2 Impact of bead-bead interactions

Controlling the scaling of the computational cost with the number of particles N is crucial for the efficiency of a computation. The calculation of the force upon each particle in the system is responsible for the main use of the CPU in a MD-simulation. Essentially such a computation requires evaluation of $\frac{N(N-1)}{2}$ pair interactions. In principle the computation time scales like N^2 , a number that quickly becomes enormous¹.

For neutral particles, a common trick to decrease the running time from N^2 to *almost* N is the use of a list of neighbours or an improved *Verlet's List* (VL) [109]. Instead of calculating the interaction from all particles on particle i one introduces a cut off radius r_c for a sphere around the particle. When evaluating the interaction among particles one takes into account only the contributions of those in the list. The list must be updated every time a neighbouring particle enter or leave the sphere. The VL identifies all the distinct pairs in the system, and avoids redundant pairs such as (i, j) and (j, i) . For large system of particles the storing and testing of the pair separation might become expensive because the size of the list increases linearly with the size of the system [106, Appendix F].

For Coulomb systems, achieving a nearly linear scaling requires state of the art approaches to compute long-range sums over charges. These are represented, for instance, by particle-particle-particle-mesh Ewald algorithms.

¹In some computations the number of particles, N can reach 10^6 [110] or even $500 \cdot 10^6$ [111].

7 | OUR NUMERICAL MODEL

As anticipated in the introductory chapters, the rapid growth of computer power and the increasing ability of experimentalists to make and manipulate systems of nanometric size is bringing within reach the computational analysis of mechanical problems of biopolymers.

Nevertheless, there is still a broad range of sizes and especially of characteristic times that exceed our ability to reproduce the time evolution of the systems of interest at the atomistic level. For this reason, a coarse grained and fairly idealised model has been developed, in many ways intermediate between atomistic simulation models and the traditional FBM.

A comprehensive study developed along these lines is reported in [4]. In this model, that we propose to call *particle-based FBM*, bundles consist of chains, made, in turn, of particles interacting only along the polymer backbone. The model introduces real time dynamics, temperature and entropy into the picture. All aspects that depend on particle-particle interactions are still missing, thus the model is unable to describe density and surface effects, or the formation of different phases (liquid, crystal, amorphous, liquid crystal, ...) throughout the sample.

The major methodological development provided by the present work consists of introducing non-bonded bead-bead interactions, reflected in a non-vanishing size of beads in the polymer chain. The numerical model originates from the Hamiltonian of [4], but with an additional potential term to describe the non-vanishing bead size. The system under study is a fibre bundle clamped to two solid-like plates. A force of equal intensity and opposite direction is applied to each of the plates, representing the tensile load on the sample. Now the potential energy of the system is the sum of pair interactions of the Morse form along the chain backbone, and a non-bonded contribution among chains. The non bonded interaction is described by the same functional form with, however, different coefficients. Despite this change of the basic Hamiltonian, the change of behaviour from the ideal chain is hardly recognisable from a superficial observation.

The introduction of general bead-bead interactions changes the computational task. Simulations require more time to account for intra- and inter-chain interactions, and might need Ewald sums in the case of polymers carrying an electrostatic charge.

The system evolution has many similarities with the non-interacting case. At variance from traditional force fields such as Gromacs, Amber or CHARMM, the covalent bonds of our model can break. Hence, the Morse pair potential acting along the chain is cut at a finite range, to make the breaking of bonds unambiguous. Moreover, our simulations are carried out by MD, whose computational via-

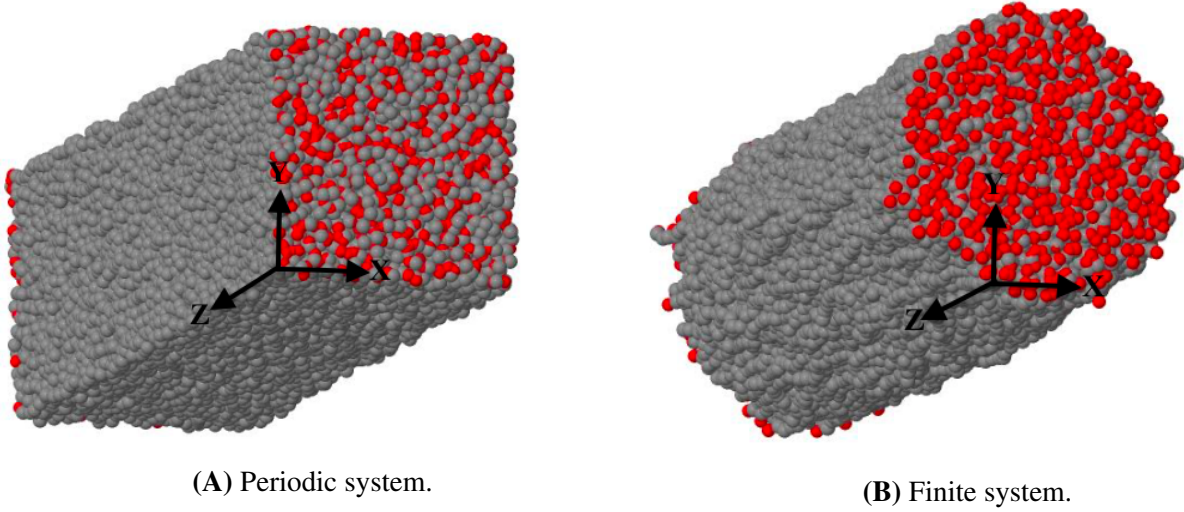


Figure 7.1: The initial configuration of a system with PBC (Figure 7.1A) and non-PBC (Figure 7.1B) before starting the stretching simulation. The bundle consists of 400 chains each made of 100 beads. Gray dots represent beads connected by intact bonds. Red dots represent the end points of the chains attached to two solid-like planar surfaces perpendicular to the z -axis.

bility requires a force field that is continuous everywhere together with its gradient. An illustration of the system is given in Figure 7.1.

7.1 System Hamiltonian

The system under study is made of n_c chains attached to two planar surfaces perpendicular to the z -axis. The two opposite chain terminations are free to move in the x - and y -directions, but along the z -direction they are kept on the boundary planes. The instantaneous length of the system is defined by $L_z = z_b - z_a$ requiring $z_b \geq z_a$.

Each chain n_c contains n_b regular beads. The position vector for bead $i = 0, 1, \dots, n_b, n_{b+1}$ is denoted \mathbf{r}_i . The z -coordinate of the two end points is defined as $z_0 = z_a$ and $z_{n+1} = z_b$. Each end point of a chain j interacts with the nearest regular bead through a harmonic potential $V_{end}(\mathbf{r})$ given by:

$$V_{end}(\mathbf{r}) = \frac{1}{2} K_{end} \mathbf{r}^2, \quad (7.1)$$

where \mathbf{r} describe the distance between interacting beads and K_{end} denotes the corresponding spring constant. Nearest neighbours along each chain interact exclusively through a truncated Morse potential:

$$V_M(\mathbf{r}) = \begin{cases} D_0 \left[e^{-2a_0(\mathbf{r}-r_e)} - 2e^{-a_0(\mathbf{r}-r_e)} \right], & \mathbf{r} < r_c \\ a_s (\mathbf{r} - r_c)^2 + b_s (\mathbf{r} - r_c)^3, & r_c \leq \mathbf{r} \leq r_c + \Delta \\ 0 & \mathbf{r} \geq r_c + \Delta. \end{cases} \quad (7.2)$$

Table 7.1: Parameters used to mimic the higher strength and shorter range of bonded versus non-bonded interactions.

	D_0	a_0	r_0
Bonded	6	2	1.5
Non-bonded	0.1	2	2

R describes the distance between neighbouring beads, D_0 the potential well depth, r_e is the equilibrium distance and a_0 the well width. A differentiable and continuous potential is guaranteed by smoothly switching off the bead-bead potential $V_M(r)$ in between r_c and $r_c + \Delta$. The requirement of a continuous definition of $V_M(\mathbf{r})$ and $V'_M(\mathbf{r})$ determines the coefficients a_s and b_s .

The same analytical term with different coefficients has been used to model non-bonded interactions:

$$E_{nonb}(\mathbf{r}_1, \dots, \mathbf{r}_n) = \sum_{pairs} U(|\mathbf{r}_i, \mathbf{r}_j|), \quad (7.3)$$

where $U(\mathbf{r})$ is defined as

$$U(\mathbf{r}) = \begin{cases} D'_0 \left[e^{-2a'_0(\mathbf{r}-r'_e)} - 2e^{-a'_0(\mathbf{r}-r'_e)} \right], & \mathbf{r} < r'_c \\ a'_s (\mathbf{r} - r'_c)^2 + b'_s (\mathbf{r} - r'_c)^3, & r'_c \leq \mathbf{r} \leq r'_c + \Delta \\ 0 & \mathbf{r} \geq r'_c + \Delta. \end{cases} \quad (7.4)$$

To mimic the lower strength and longer range of non-bonded versus bonded interactions we used the parameters given in Table 7.1.

7.1.1 Two different but related chain models

Following the standard practice in force field models, we neglect non-bonded interactions among the closest neighbours of each chain. Atomistic force fields neglect three or four nearest neighbours. Since our force field is simple, we neglect only up to second neighbours. More precisely most of the simulations have been carried out using a model neglecting non-bonded interactions on nearest neighbours only. We call this our *regular chain model*. Remarkably, we noticed that neglecting non-bonded interactions up to second neighbours (along the chain) gives a model reproducing some of the most intriguing features shown by single chains and bundles of polynucleotides. As shown in the following chapters, the stress-strain relation for this model, that we will call *extensible chains model*, shows two distinct regimes at low and at high tensile load. The apparent non linearity in the system response is due to the possibility of second neighbours to occupy the same position since they lack short range repulsion. In this way they gain additional non-bonded attraction when the chain is not

highly strained. The compact configuration, however, is a disadvantage when the applied load is high. In such a case the bundle adopt a more extended configuration, loosing part of the cohesive energy, but gaining from the work performed by the external load. This mechanisms endows the model with a two-states phase diagram, that closely corresponds to the DNA behaviour as introduced in Section 3.2.

An analytic expression for the wall potential $V_{wall}(\mathbf{r})$ is added to the Hamiltonian to restrict the movements of the beads in space and enclose the system by the separation plates at z_a and z_b :

$$V_{wall}(\mathbf{r}) = \frac{1}{2}k_{wall} \left[(z - z_L)^2 \theta(z_L - z) + (z - z_R)^2 \theta(z - z_R) \right]. \quad (7.5)$$

\mathbf{r} is the position vector of the interacting bead and θ denotes the Heavyside step function defined as:

$$\theta(z) = \begin{cases} 0, & \text{for } z < 0, \\ 1, & \text{for } z \geq 0. \end{cases} \quad (7.6)$$

Describing the bead-bead interaction in the system by a potential term $U(\mathbf{r}_{i,j})$ the total system potential energy becomes:

$$V(\{\mathbf{r}_i^{(j)}\}) = \sum_{j=1}^{n_c} \left\{ \frac{1}{2} V_{end} |\mathbf{r}_1^{(j)} - \mathbf{r}_0^{(j)}|^2 + \sum_{i=1}^{n_b-1} V_M(|\mathbf{r}_i - \mathbf{r}_{i+1}|) + \sum_{i>j}^{n_b} U(\mathbf{r}_{i,j}) + \sum_{i=2}^{n_b-1} V_{wall}(\mathbf{r}_i^{(j)}) + \frac{1}{2} V_{end} |\mathbf{r}_{n_b}^{(j)} - \mathbf{r}_{n_b+1}^{(j)}|^2 \right\}. \quad (7.7)$$

The kinetic energy is given by

$$K = \frac{1}{2} m_e \sum_{j=1}^{n_c} \sum_{i=0}^{n_b+1} |\dot{\mathbf{r}}_i^{(j)}|^2, \quad (7.8)$$

where m_e describes the mass of the end-point bead. The total system Hamiltonian is given by contributions from both the potential and the kinetic energy:

$$H(\{\mathbf{r}_i^{(j)}\}, \{\dot{\mathbf{r}}_i^{(j)}\}) = V(\{\mathbf{r}_i^{(j)}\}) + K(\{\dot{\mathbf{r}}_i^{(j)}\}). \quad (7.9)$$

Writing and integrating the equations of motion of the Hamiltonian in Eq. (7.9) leads to the dynamics of a microcanonical (V, E, N) ensemble with conserved quantities for volume, energy and particles. During stretching of the bundle we apply a tensile load, thus our numerical system is not isolated and the constant energy condition is not fulfilled. To keep the state of the system constant we imagine our sample to be in contact with a pressure and temperature bath. In our simulation approach

these conditions have been met by introducing a Lagrangian of the particle coordinates with a few additional variables. We then turn to a Lagrangian formulation.

7.1.2 The Lagrangian

All simulations are carried out at constant temperature (see below). Simulations for bundles extended in 2D are carried out at constant pressure. The pressure in the simulations of finite bundles identically vanish since the sample exposes free surfaces in the three directions.

To keep pressure constant during the simulation of systems periodic in 2D, we let the size of the simulation box fluctuate in time. The fluctuation of the box is denoted as ξ . By the use of *Periodic Boundary Condition*¹ (PBC) and treating ξ as an additional parameter we perform a coordinate transformation along the x - and y -direction $(x, y, z) \rightarrow (\xi S_x, \xi S_y, z)$. Following Ref. [112] we postulate an extended Lagrangian:

$$\mathcal{L} = \underbrace{\frac{m}{2} \sum_{i=1}^n (\dot{S}_x^2 + \dot{S}_y^2)}_{\text{Kinetic term}} + \frac{m}{2} \sum_{i=1}^n \dot{z}^2 + \frac{W}{2} \dot{\xi}^2 - \overbrace{\sum_{i=1}^n \sum_{j>i}^n \phi(r_{i,j}) - \sum_i^n v(z_i) - P_{2D} \xi^2}^{\text{Potential term}}. \quad (7.10)$$

The individual bead mass is denoted by m , the derivative of the transformed position coordinates are described by \dot{S}_x, \dot{S}_y , W the phenomenological mass of the system, a pairwise additive potential is denoted $\phi(r_{i,j})$ and a kinetic 2D pressure along x - and y -direction is denoted P_{2D} . The systems equations of motion are derived from the Euler-Lagrange equation [108, Chapter 2]

$$\begin{aligned} \ddot{\xi} &= -\frac{\xi}{W} \left[m \left(\sum_i \dot{S}_x^2 + \dot{S}_y^2 \right) - 2P_{2D} \right] \\ \ddot{z} &= \frac{1}{m} \left[\sum_{j>i} \frac{\partial \phi(\mathbf{r}_{i,j})}{\partial \mathbf{r}_{i,j}} \frac{\partial \mathbf{r}_{i,j}}{\partial z} - \dot{v}(z) \dot{z} \right] \\ \ddot{S}_k &= \frac{1}{m\xi^2} \left[\sum_{j>i} \frac{\partial \phi(\mathbf{r}_{i,j})}{\partial \mathbf{r}_{i,j}} \frac{\mathbf{r}_i - \mathbf{r}_j}{r_{i,j}} \right] - 2\frac{\dot{\xi}}{\xi} \dot{S}_k, \quad k = x, y. \end{aligned} \quad (7.11)$$

¹PBC is based on the infinite replication of the system dividing space into periodic boxes. A particle leaving the box at one side reenter through the opposite side.

7.1.3 Temperature with Langevin Dynamics

As suggested in Section 6.1 one solves Newton's equation of motion by the velocity Verlet algorithm. The application of the external load, however, implies that work is performed on the system during its time evolution, continuously changing the thermodynamics parameters during the experiment. In real-life experiments, temperature is kept nearly constant by the unavoidable thermal contact with the environment. To mimic the same effect and to control temperature we resort to the well known *Langevin Dynamics* (LD). During the stretching we perform work on the system, and thus the energy will increase. However, the temperature can be kept constant by a slight modification of the integration algorithm and by introducing LD [113]. To change from Newton's to Langevin's dynamics we add two forces, representing thermal noise $\beta(t)$ and a frictional force proportional to the velocity $\gamma_i \geq 0$. Hence, the equations of motion of Langevin's dynamics take the form:

$$\mathbf{F}_i - \gamma_i \dot{\mathbf{q}} + \beta(t) = m_i \ddot{\mathbf{q}}_i. \quad (7.12)$$

The forces derived from the potential energy is still described by \mathbf{F}_i . The random force $\beta(t)$ must satisfy the relations

$$\begin{aligned} \langle \beta_i \rangle &= 0 \\ \langle \beta_i(t) \cdot \beta_j(t') \rangle &= 6\gamma_i k_B T \delta_{i,j} \delta(t - t'). \end{aligned} \quad (7.13)$$

where T is the target temperature in the simulation, k_B denotes the Boltzmann constant and δ is the Dirac delta distribution.

The singular character of the *white noise* contribution prevents the straightforward application of the Verlet or velocity Verlet algorithm. To overcome this problem, a slightly modified version of the velocity Verlet is adopted, using the approach of [113].

7.2 Investigated values

All the values in our simulations were given in scaled units, most computed quantities turn out to be of the order of unity. This gives the advantage of results with scalability. Chosen parameters in the simulations are given in Table 7.2.

Table 7.2: Parameters used in simulations.

Physical quantity	Variable	Value
Number of chains in the bundle	n_c	400
Number of beads per chains	n_b	100
Mass of the beads	m_{beads}	1
Time step	Δt	0.005
Smooth cutoff for the potentials	r_c	3
Cutoff length for the potentials	Δ	0.5
External pressure	P	40
Boltzmann constant	k_B	1

7.2.1 The choice of time step Δt

Following standard practice and experience a stable solution of the equations of motion requires $\sim 10^2$ simulation points over an oscillator period. In this way each oscillation needs to be covered by 100 points. To be on the safe side we took the time step $\Delta t = 5 \cdot 10^{-3}$. An efficient way to validate the implementation is to show that energy is conserved when Langevin dynamics is replaced by the Newtonian dynamics.

7.3 Limitations of the model

The very idealised description of microscopic interactions throughout the system is certainly the first and major limitation of the model. Polymers are described at the coarse grained model, without any detail of the (often complex) atomistic structure. Bead-bead interactions are isotropic, while in reality hydrogen bonding and complex molecular structures impart a strong anisotropy to the interactions. Beads are neutral, and including Coulomb interactions would require much longer computations. Moreover, the realistic and quantitative description of bond breaking events requires at least standard approximations for the electronic structure, usually formulated within density functional theory.

The second major limitation is represented by the short size and time scales covered by MD-simulations. Although the reach of the method is expanding, we are still short of realistic simulations.

The equations of motion underlying our simulations describe the time evolution of classical particles. At the molecular level, all systems are quantum mechanical, at least to some degree. No current method is able to cover the quantum mechanical aspects of complex systems.

Our samples interact only with the clamps. In reality, and especially in biological systems, bundles are embedded into a relevant environment, often represented by electrolyte-water solutions.

In our model, covalent bond can break but they cannot recombine. However, more than a limita-

tion of the model, this is our choice of model to be simulated, that in this case describes systems in which covalent bonds, once broken, do not form again.

Despite these limitations, we think that our models and simulations provide a general view of bundles, and might represent a useful tool to understand their role in biological systems.

8 | RESULTS

Simulations concerned four distinct versions of the particle-based FBM. In all cases, bundles are limited along their longitudinal axis by the planar clamps.

Two variants, one regular and one extensible, concerned fibres of finite size in all directions, exposing a free polymer surface limiting a bundle of approximately cylindrical shape. Two other variants, again for a linear and for an extensible polymer, concerned bundles extended along the plane perpendicular to the fibre axis. To limit size effects, PBC are applied along the x - and y -directions perpendicular to the longitudinal z -axis of the bundle.

Two types of stretching experiments have been simulated, corresponding to constant applied load, and to stretching at a constant strain rate, closely corresponding to the approaches used to characterise creep in real-life experiments.

The presentation of the results is based on the finite bundle case. When needed similarities and differences are given in the second part of the chapter.

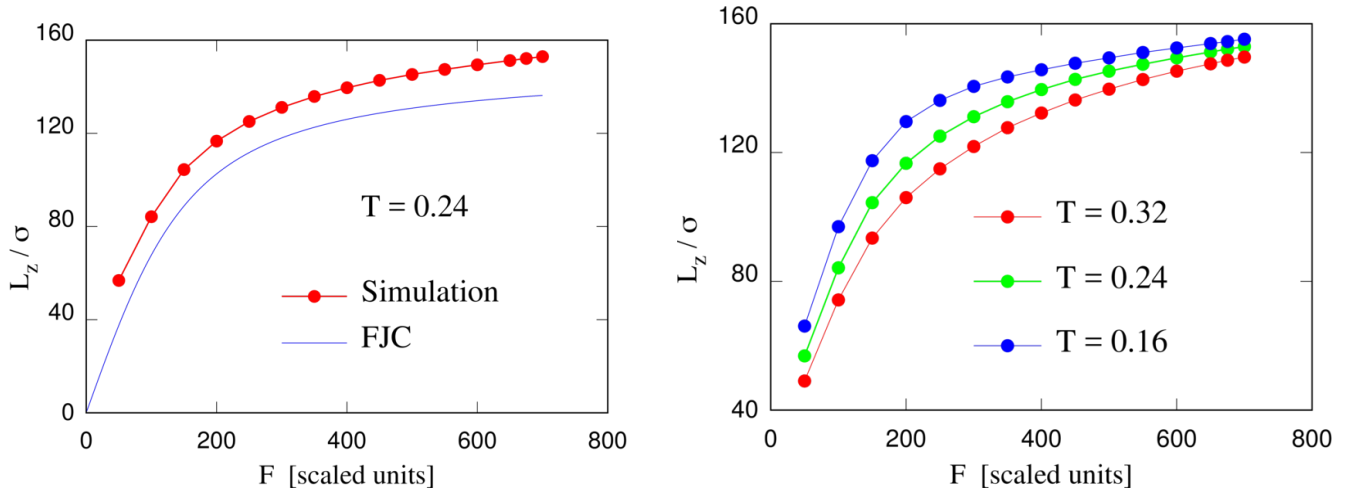
8.1 Sample preparation

For each of the four variants of the basic model, a first *generating* sample has been prepared by equilibrating a bundle of 400 chains, 100 beads long at $T = 0.8$ (in our scaled energy units) a temperature at which the sample appears to be liquid. A short further equilibration lasting 10^6 steps was carried out at the same $T = 0.8$ with the addition of a moderate tension $F = 40$ in scaled units. No bond breaking was allowed during equilibration.

Then, a representative population of twenty samples was generated by running further 10^6 MD steps at constant conditions, selecting one configuration every $50 \cdot 10^3$ MD steps. These samples have been used for all the simulations discussed below.

At first, these samples were brought to the different low temperatures of $T = 0.24$, $T = 0.30$, and $T = 0.33$. At these temperatures, both the finite and the extended samples appeared to be solid-like. More precisely, they appear to be in a glassy state, since no local and, even less, long range ordering was identifiable. Annealing took place by reducing at a constant rate the target temperature in the Langevin equations. In all these standard cases, temperature was decreased at the rate of $1 \cdot 10^{-6}$ per MD step.

At this stage, and before allowing for bond breaking, we characterise a few basic properties of the bundles. The elongation of the bundle under increasing load at $T = 0.24$ is compared to the



(A) A comparison of the length of a finite regular and a FJC bundle as a function of load at $T = 0.24$. The solid dots represent the values of the simulations, the continuous blue line is the prediction of the FJC.

(B) A comparison of the length of finite regular bundles as functions of load at different temperatures. The solid dots represent the values of the simulations. Lines are a guide to the eye.

Figure 8.1

prediction of the FJC model in Figure 8.1A. Both curves display a linear behaviour at low load, and saturate to high load. The results depend on temperature, and Figure 8.1B shows this reproduced in a graphical form. Interesting, but as expected, bundles get shorter with increasing T . This observation shows that even in the case of interacting beads, the entropy of ideal chains will largely determine the size and elastic properties of the bundle.

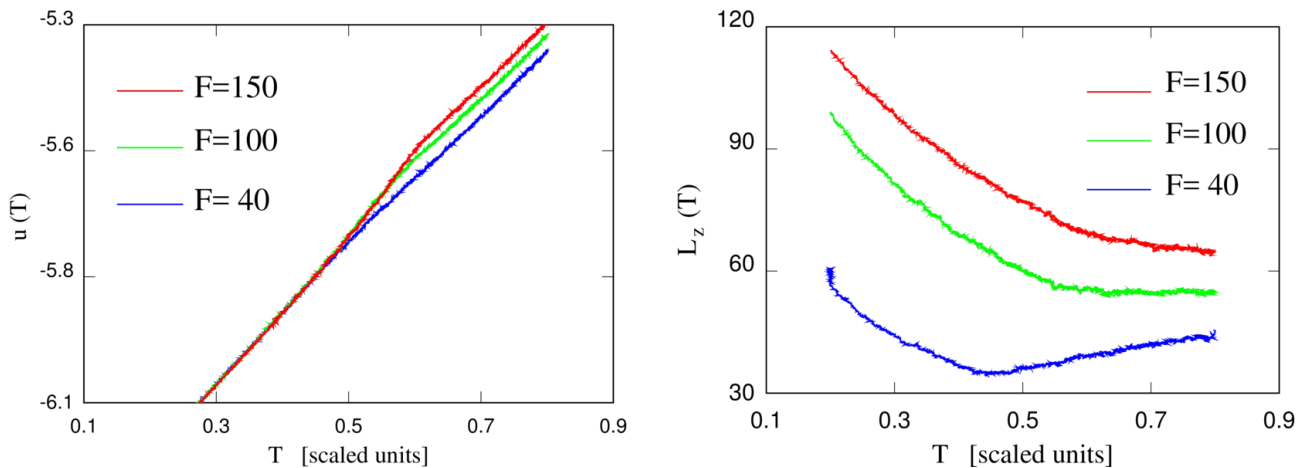
To verify the ability of our sample preparation protocol to approach equilibrium before the stretching experiment takes place, we carried out a longer annealing of a linear, finite sample (i.e., without PBC), at a rate of 10^{-7} per MD step. A short movie of the sample evolution during the $6 \cdot 10^6$ steps of the annealing is shown online [here](#). The first simulation took place with an applied force of $F = 40$.

The temperature dependence of the potential energy per particle $u(T)$ and of the bundle length $L_z(T)$ during the annealing is shown in Figure 8.2. The results are reproducible and reversible, meaning that if we cycle the temperature, the system follows the same $u(T)$ and $L_z(T)$ curves with almost no hysteresis. In simpler systems, the change of slope in $u(T)$ at $T \sim 0.4$ would mark the glass point of the fluid. In this case the interpretation is less obvious, since the $u(T)$ result is complemented by the reversal of slope in $L_z(T)$ taking place at nearly the same temperature. At $T > 0.4$, in particular, the sample displays the normal thermal expansion behaviour. At $T < 0.4$, the system becomes longer with decreasing T , very likely because in polymers entropy represent a major factor in limiting the system size to $\sim N^{1/2}$, instead of the $\lim N$ scaling expected for a chain relaxed at $T = 0$.

As already stated, data shown in Figure 8.2A have been collected with $F = 40$. A series of curves for different F values clarify the meaning of the change of behaviour at $T = 0.4$. Figure 8.2B collects

the results of annealing the same bundle with an applied tensile load of $F = 100$ and $F = 150$. The anomaly in the $u(T)$ curve has evolved into a kind of jump probably broadened by finite size effects, taking place at higher temperature with increasing value of F . Analysis of snapshots suggests that anomaly and jump mark the crystallisation (low T portion of the data) transition out of a liquid like sample. Crystallisation requires a non-negligible load. Below a threshold that we did not locate the bundle transforms into a glassy structure. The results for $L_z(T)$ under tension reflect the changes of $u(T)$, and show additional features that we not discuss to limit the size of the thesis.

Explicit tests of stretching and failing by creep show that the one order of magnitude reduction of the annealing rate increases the creep resistance of the sample. In this respect, the result of the text contradicts the hypothesis that the standard annealing is able to produce equilibrated systems. Nevertheless, we decided to proceed with the standard population of 20 samples at $T = 0.24$, $T = 0.30$ and $T = 0.33$ as representative of systems in the amorphous state, close but, strictly speaking, not at equilibrium. The bundle life time τ of the samples was defined to be the required time to break 400 chains.



(A) Energy per particle $u(T)$ during the annealing process of a finite regular bundle.

(B) Sample length $L_z(T)$ during the annealing of a finite regular bundle.

Figure 8.2: Energy per particle (Figure 8.2A) and sample length (Figure 8.2B) during the annealing process from $T = 0.8$ to $T = 0.2$ at a rate 10^{-7} per MD step. A low tension $F = 40$ was applied during the entire annealing

8.2 Regular finite bundle

We regard our regular finite bundle as the most important of our systems, since it might represent a numerical model for some of the nanometric biopolymers described in the 3, 4, and 5.

8.2.1 Evolution under tension

The time evolution during a stretching experiment at $T = 0.24$ and $F = 550$ is displayed in Figure 8.3. The snapshots clearly show that the sample grows thinner and thinner on the middle during the simulation because the broken fibres coil around their clamped end points to minimise the free energy of the bundle surface. Surprisingly the bundle fractures at two points. The first fracture occurs close to the left clamp, the second fracture occurs close to the right clamp. Roughly 50% of the original bundle remains isolated in the middle, no longer in contact with the clamps. The surface produced by the fracture are rather chaotic and certainly not smooth. Two remarkable observations are worth emphasising already at this point: creep represents a very slow relaxation process taking place in the system. Before the avalanche stage one hardly detects the irreversible increase in the length of the bundle, lasting many million periods of the fastest (stretching) oscillation modes. The second observation is that the slow irreversible sample evolution of the first stages turns violent in the avalanche stage, breaking many bonds on chains already broken, and ejecting high energy fragments of low energy. This last observation might provide a new approach to detect fracture in its early stages.

8.2.2 The effect of the force

The instantaneous length of a regular finite bundle at $T = 0.24$ and load $F = 450$ is displayed in Figure 8.4A. Due to a small applied tensile load in the post annealing stage the length of the equilibrated bundle is $L_0 \sim 144$ at $t = 0$. As the time evolves the elongation curve clearly follows the typical behaviour of soft viscoelastic materials described in Section 2.2. First, the system undergoes a short elastic region where the bundle length increases suddenly. This primary regime is followed by a long creep regime lasting most of the simulation time in which the bundle length slowly increases. In the tertiary regime the creep rate increases before the bundle rupture.

The marked region in Figure 8.4A displays a neck in the elongation curve where the curvature seems to change at slightly more than 50% of the simulation time. The steady rate of the change in bundle length is caused by the slow process of chain breaking, the system would set to an equilibrium state with out this effect.

Figure 8.4B displays the number of broken chains \bar{n}_c and broken bonds \bar{n}_b in the bundle as a function of time. As expected, the breaking of bonds and chains follows the exact same curve before the bundle life time τ is reached and the sample fractures. After this point only bonds can break. The rate at which chains and bonds break increases slowly over the creep region before it accelerating when approximately 25% of the chains have been broken and starts an avalanche of chain breaking

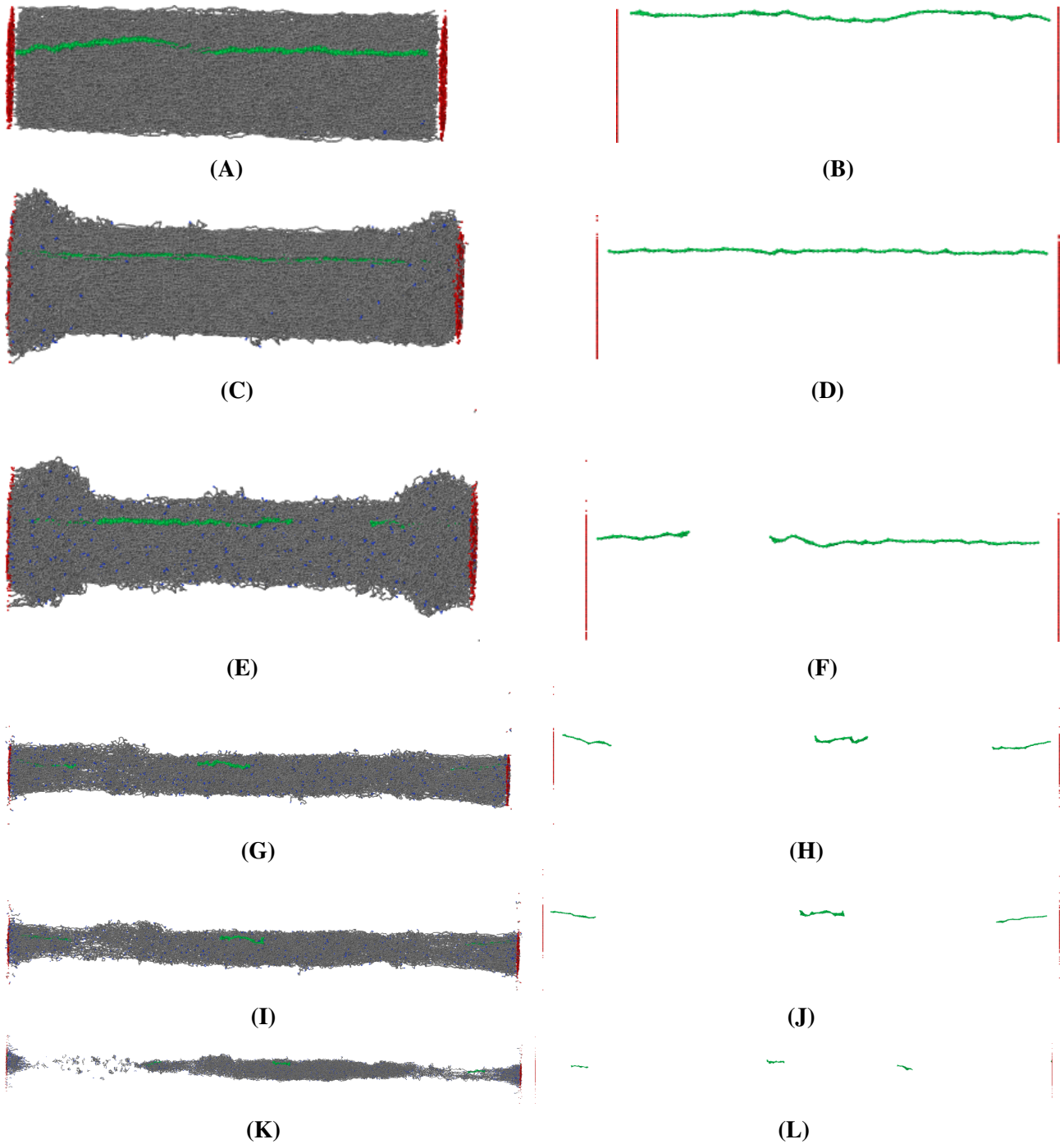


Figure 8.3: Snapshots taken at non-uniform times in a simulation of a regular finite regular bundle (Figures 8.3A, 8.3C, 8.3E, 8.3G, 8.3I, and 8.3K.) and a single fibre (Figures 8.3B, 8.3D, 8.3F, 8.3H, 8.3J, and 8.3L.). Red beads illustrate the chains head points, gray beads represent intact bonds, blue beads illustrate broken bonds, and green beads are components in a single chain fibre at the bundle surface.

in the end of the simulation. The acceleration in chain breaking and the simultaneous increase of the system length in the end of the simulation is due to increased interchain interactions.

Figure 8.5A displays the elongation curves for the same system under different loads. The effect of the applied tensile load is also as expected: the system at highest load breaks first, higher load decreases the creep resistance of the sample. The number of broken chains as a function of time follows the same curve as in Figure 8.4B. The chains break at a slow rate at first before an avalanche starts after 25% of the chains have been broken for all the different forces.

As already stated, slowing down the annealing procedure gave a significantly increased bundle life time τ . This effect is graphically displayed in a creep experiment for a system at $T = 0.24$ and $F = 500$ in Figure 8.6.

8.2.3 The effect of the temperature

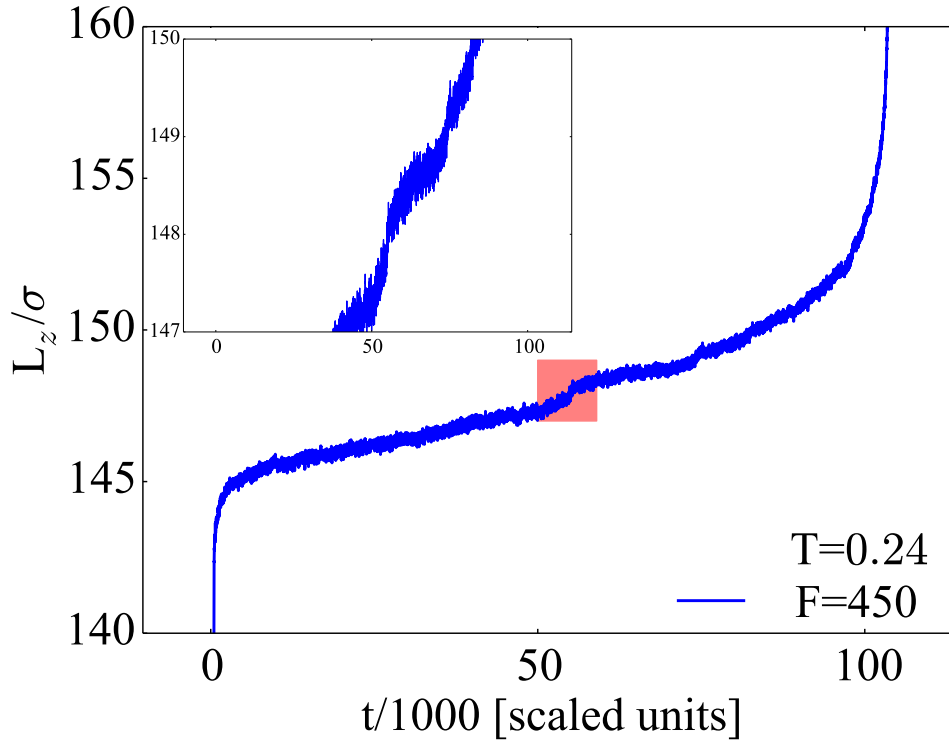
To quantify the effect of temperature, a series of simulations have been carried out on bundles loaded by $F = 360$ at temperatures $0.24 \leq 0.33$. The results for the time dependence of the sample length are reported in Figure 8.7A, and, as expected, show that the bundle lifetime is shorter at higher temperature. These results are converted into an Arrhenius plot (Figure 8.7B) showing the logarithm of the bundle lifetime as a function of inverse temperature. The simulation points are interpolated fairly well by a straight line, showing that the bundle breaking is a regular activated event. The slope of the linear interpolation measures the activation energy, and can be used to extrapolate our results to lower temperatures, corresponding to lifetimes beyond the reach of our simulations.

8.3 Regular periodic bundle

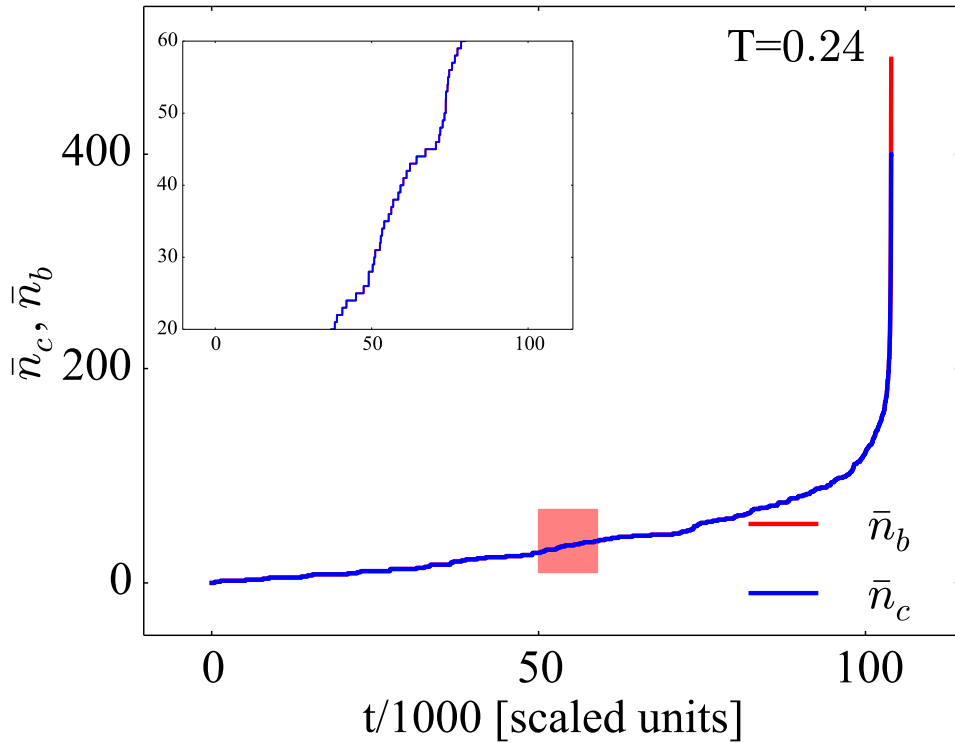
In contrast to the regular finite bundle our periodic sample does not display the effects of the finite surface. Figure 8.8A display the elongation curve as a function of time for a regular periodic bundle. The curves follows the same form as the elongation of the regular finite bundle, given in Figure 8.9A. The anomaly dividing the creep regime is longer than one seen in the finite system and appears before half of the simulation time has passed, shown in Figure 8.9B.

The breaking of chains as a function of temperature follows the same form independently of the applied force as displayed in Figure 8.8B. The rate of chain breaking in the regular periodic systems are always a little higher then the rate in the regular finite system displayed in Figures 8.9C and 8.9D.

The simulation trajectories offer a very detailed view of the breaking process. As an example of the investigations that can be carried out, we analyse the distribution of strain for covalent bonds in a

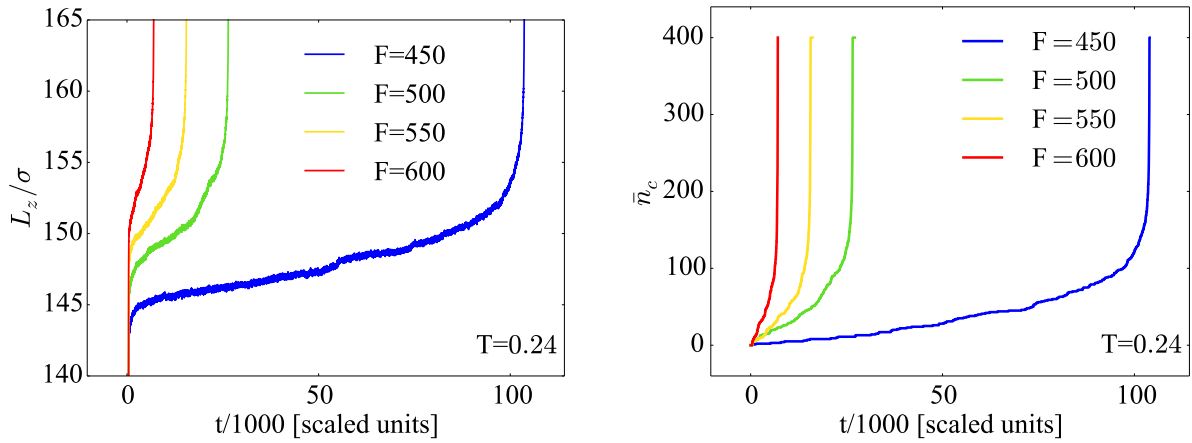


(A) The length of a regular finite bundle as a function of time at $T = 0.24$.



(B) Broken chains \bar{n}_c and broken bonds \bar{n}_b in a finite regular bundle as a function of time at $T = 0.24$.

Figure 8.4: Instantaneous system length (Figure 8.4A) and rate of broken chains (Figure 8.4B) in a regular finite system at $T = 0.24$ and $F = 450$.



(A) The length of finite regular bundles as a function of time at $T = 0.24$ and different forces.

(B) Broken chains in finite regular bundles as a function of time at $T = 0.24$ and different forces.

Figure 8.5: The effect of the force on regular finite bundles.

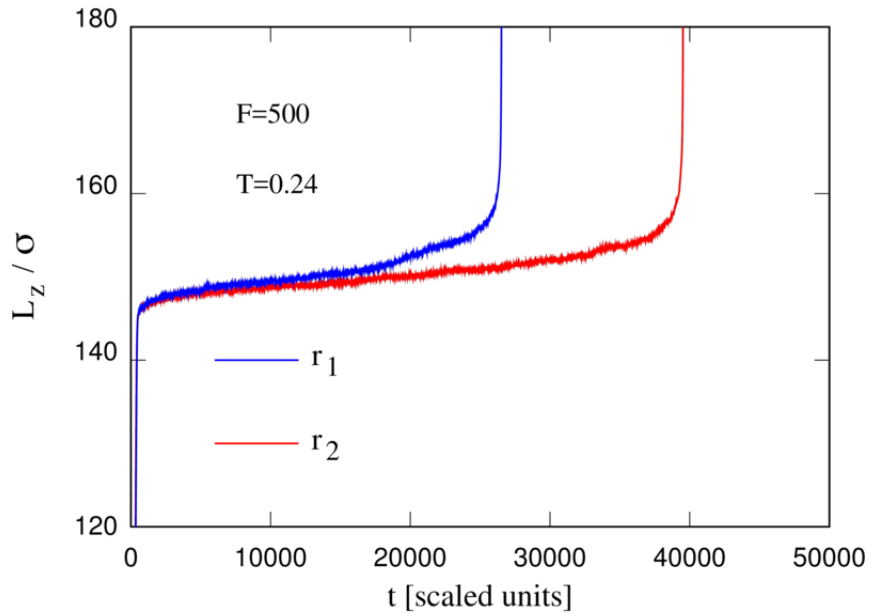


Figure 8.6: Comparison of the effect of a short reduction of the temperature ($r_1 = 1 \cdot 10^{-6}$ per MD-step) and a long relaxation reduction of the temperature ($r_2 = 1 \cdot 10^{-7}$ per MD-step) in a creep experiment on a regular finite bundle.

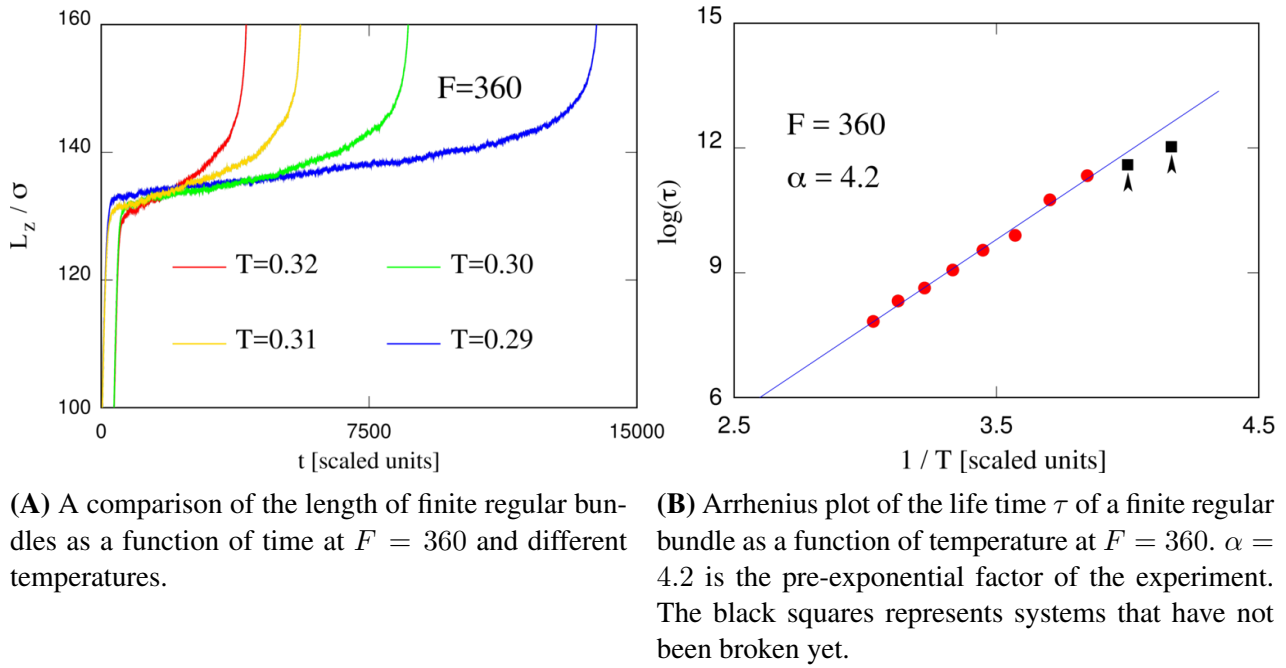
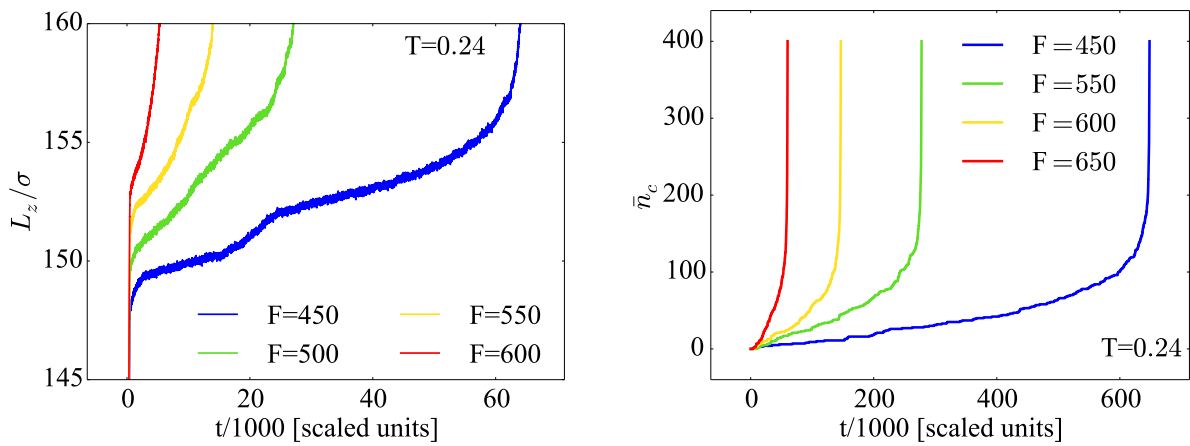
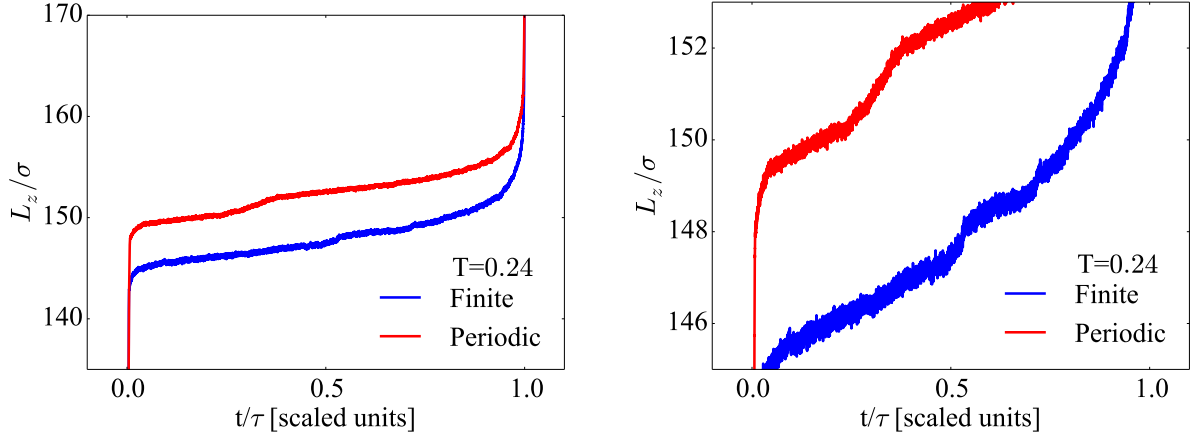


Figure 8.7: The effect of the temperature on regular finite bundles.

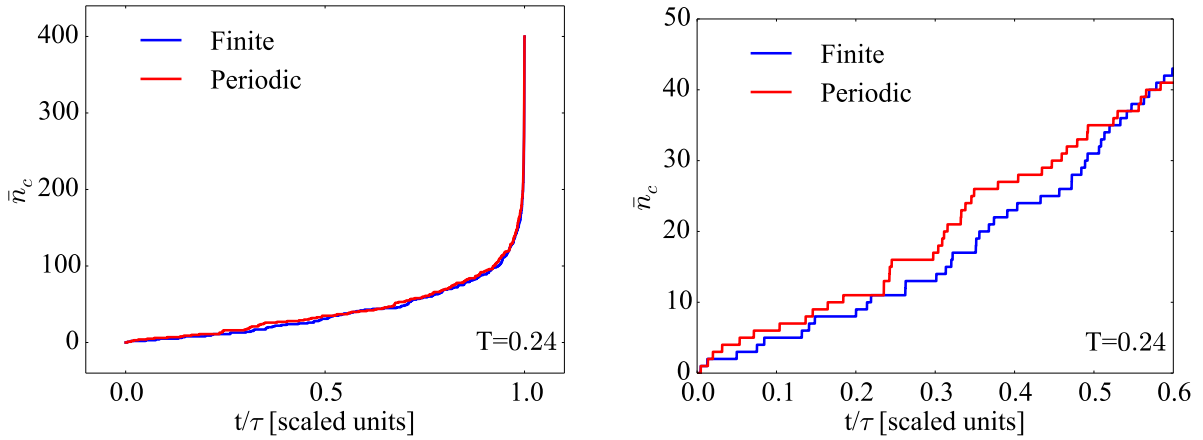


(A) The length of periodic regular bundles as a function of time at $T = 0.24$ and different forces. **(B)** Broken chains in regular periodic bundles as a function of time at $T = 0.24$ and different forces.

Figure 8.8: The effect of the force on regular periodic bundles.

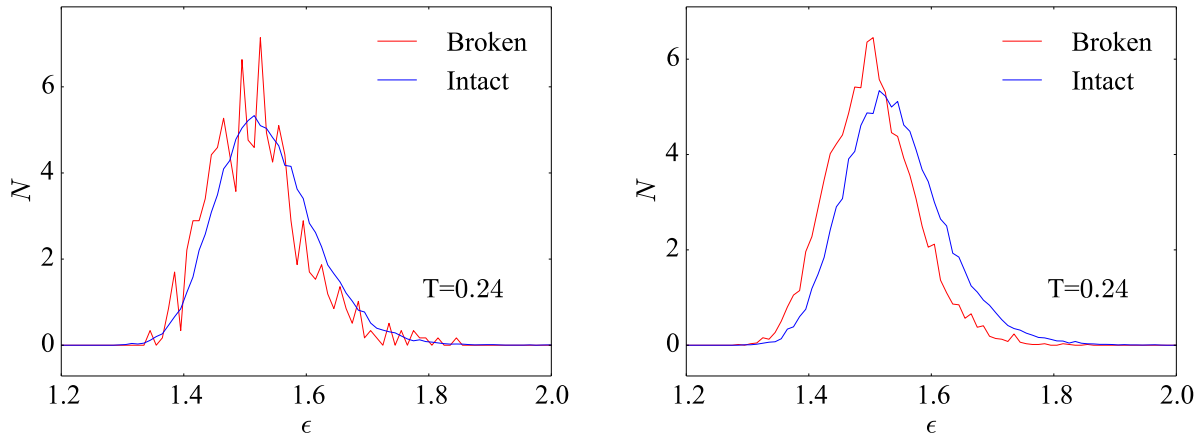


(A) A comparison of the length of periodic regular and finite regular bundles as a function of normalised time at $T = 0.24$ and $F = 450$. (B) A zoomed comparison of the length of periodic regular and finite regular bundles as a function of normalised time at $T = 0.24$ and $F = 450$.



(C) A comparison of broken chains of periodic regular and finite regular bundles as a function of normalised time at $T = 0.24$ and $F = 450$. (D) A zoomed comparison of broken chains of periodic regular and finite regular bundles as a function of normalised time at $T = 0.24$ and $F = 450$.

Figure 8.9: Interesting differences in the observables from the simulations of regular periodic and finite periodic bundles.



(A) Distribution of strain at $t = 3 \cdot 10^3$ with 3 broken chains. (B) Distribution of strain at $t = 51 \cdot 10^3$ with 65 broken chains.

Figure 8.10: The distribution of strain on broken and intact chains early (Figure 8.10A) and late (Figure 8.10B) in the simulation of regular periodic bundles under a tensile load $F = 450$ at $T = 0.24$.

regular bundle at $T = 0.24$ and $F = 450$. We compare, in particular, the probability distribution of strain on broken and intact chains at the beginning of the simulation when only 3 chains are broken, with those of a later stage, when 65 chains (out of 400) are broken. The results are displayed in Figure ?? . As expected, they show that with increasing chain breaking, bonds on intact chains are the most elongated, since they feel the impact of the applied tensile load to a greater extent than the unbroken chains. As more of the chains break the distribution of strain on broken chains becomes better defined and less noisy.

8.3.1 Constant strain rate

To mimic the approach of real creep experiments we also performed stretching test at a constant strain rate. In this case our simulation was carried out by moving the confining plates outward at a constant speed and measuring the force at the two plates.

Figure 8.11 displays snapshots from a creep simulation of a regular periodic bundle at a constant strain rate $\dot{\epsilon} = 5.0 \cdot 10^{-6}$ and temperature $T = 0.24$. In contrast to the evolution of the finite regular systems, broken fibres do not tend to coil near the bundle end when they break. This is also an effect of our interpretation of the surface, which in this case is periodic in the x - and y - directions. This effect is clearly seen in the evolution of the single (green) fibre that tends to buckle back and fourth in the xy -plane and not coil at the confining plates. After fracture the bundle splits into two equally sized parts separated at the middle. In comparison with the regular finite bundle, the fractured surface is extremely smooth. Figure 8.12 displays the fracture surface as seen in the half bundle and a geometric interpretation of the surface.

Figure 8.13A displays the applied force as a function of normalised time at different strain rates on regular periodic bundles. As expected, the strain rates impact the chain breakings. The sample at the highest strain rate first reaches 400 broken chains as displayed in Figure 8.13B.

As shown in Figure 8.14, broken chains and broken bonds deviate from each other after ~ 50 chains are broken, thus the relation between the breaking of chains and bonds follows a different path than the other regular samples at constant stress. No chains, or bonds breaks before the force reaches a critical value determined by the strain rate. The number of broken bonds is from this point always higher than the number of broken chains.

8.3.2 Low density samples

Low density samples were produced by suddenly removing the extra pressure from the regular periodic bundles at high T . Surprisingly the system at $T = 0.24$ changed into fractal-like structures, made of bundles quenched to a low density, out of equilibrium state consisting of a few tens of chains displayed in Figure 8.15.

8.4 Extensible periodic bundle

Again we would like to remind our readers about the second kind of our chains: the extensible system. These are characterised by neglecting non-bonded interactions up to the second neighbour along the chains, which produced a highly non-linearity in the stress-strain relations.

Figure 8.16A displays how the non-linear property of the chains affects the creep regime of the extensible periodic bundles. Both the equilibrated samples of initial lengths $L_0 \sim 87$ first experience a short creep regime before they both undergo a phase transition followed by a new period of creep. The bundle where bond breaking is allowed during the equilibration process experience a much shorter lifetime than the bundle in which bond breaking was prevented. The form of the elongation curves are qualitatively different. The phase transition can be interpreted as follows: the additional energy caused by the tensile load is at first only big enough to rupture the superimposed bonds. The rupture of these bonds is seen in the first creep region. The normal chains does not break before a little longer before the additional energy from the load is big enough to rupture these bonds.

A hint on the consequence of the exclusion of the second neighbours in the chains are given in the intrachain correlation function at times before, $t_1 = 3.0 \cdot 10^4$, and after, $t_2 = 6.0 \cdot 10^6$ the phase transition. Figure 8.16B displays a clear reduction in the intrachain interactions during the stretching process.

As for the other systems under constant strain rate the breaking of chains follows the breaking of

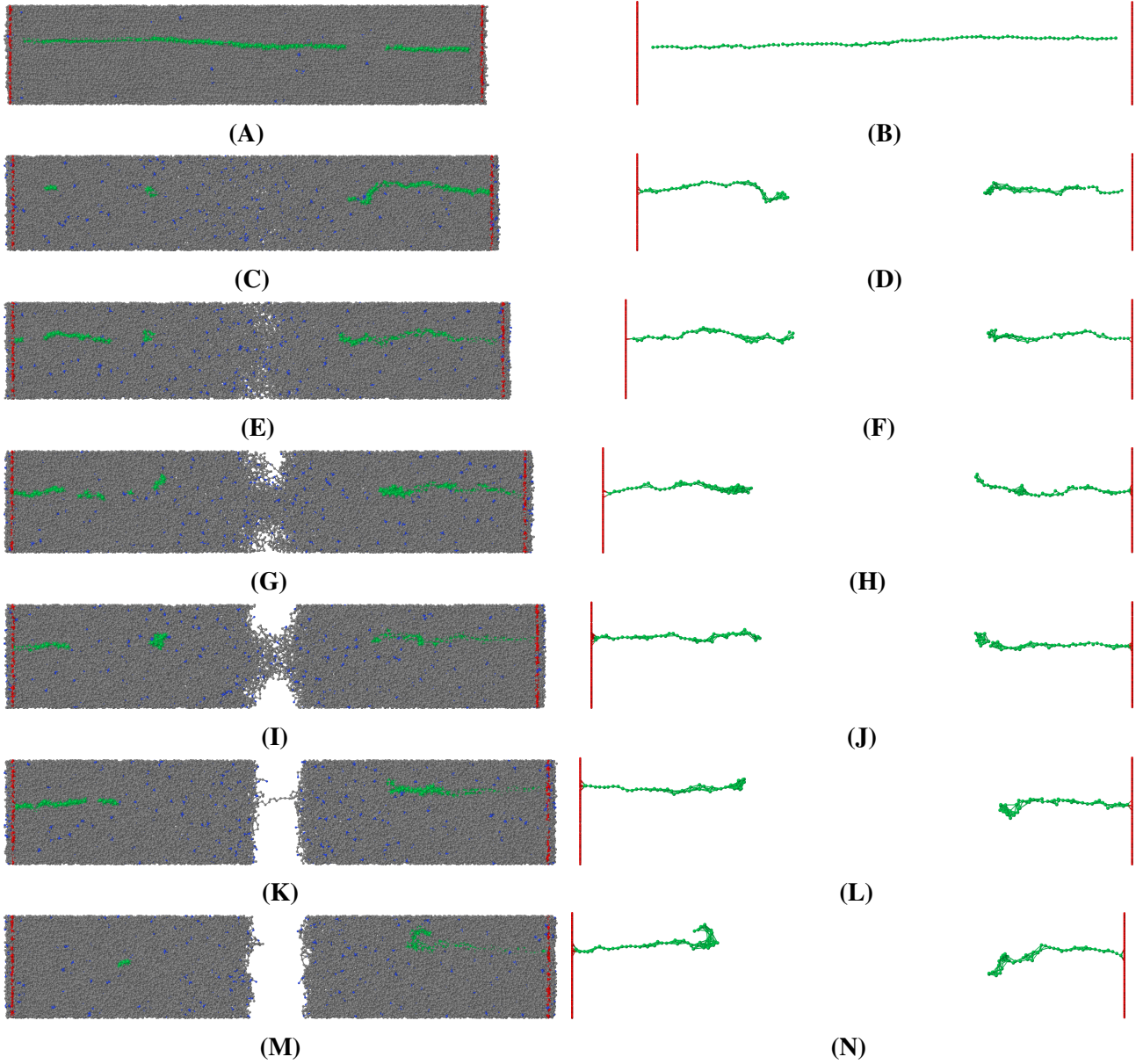
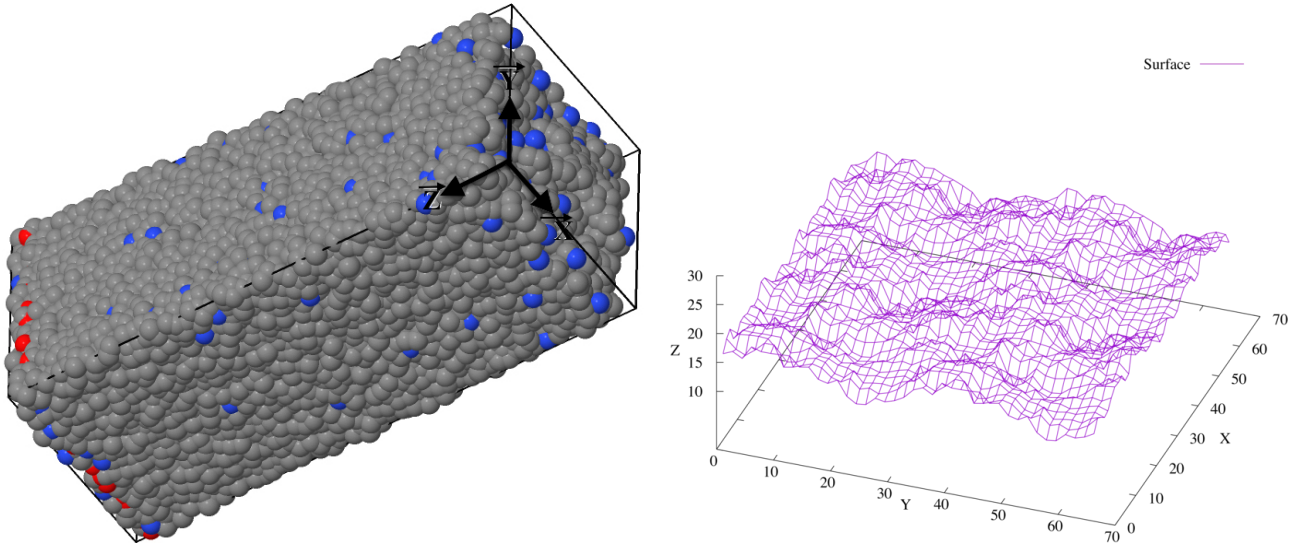


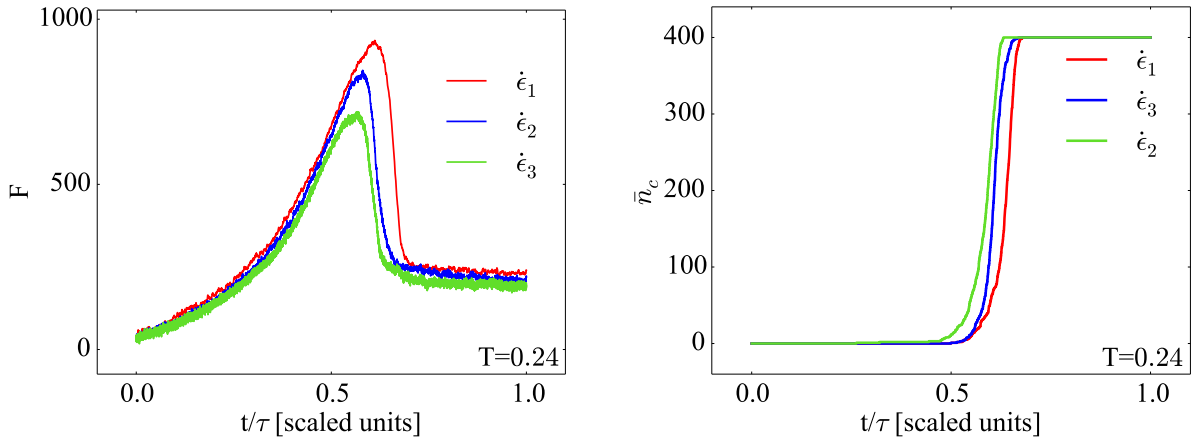
Figure 8.11: Snapshots taken at non-uniform times in a simulation of a regular periodic bundle (Figures 8.11A, 8.11C, 8.11E, 8.11G, 8.11I, 8.11K, and 8.11M.) and a single fibre (Figures 8.11B, 8.11D, 8.11F, 8.11H, 8.11J, 8.11L, and 8.11N.) at constant strain rate $\dot{\epsilon} = 5.0 \cdot 10^{-6}$ and temperature $T0.24$. Red beads illustrate the chains head points, gray beads represent intact bonds, blue beads illustrate broken bonds, and green beads are components in a single chain fibre at the bundle surface.



(A) Fracture surface. Red beads illustrate the end points of the chains, gray beads represent intact bonds, and blue beads illustrate broken bonds.

(B) Geometric interpretation of the fracture surface.

Figure 8.12: The fracture surface (Figure 8.12A) and a corresponding geometric surface (Figure 8.12B) of a regular periodic sample at constant strain rate $\dot{\epsilon} = 5.0 \cdot 10^{-6}$.



(A) Applied load F on regular periodic bundles as a function of normalised time.

(B) Broken chains as function of normalised time on regular periodic bundles as a function of normalised time.

Figure 8.13: Evolution of applied load (Figure 8.13A) and broken chains (Figure 8.13B) as a function of normalised time at $T = 0.24$ and constant strain rates: $\dot{\epsilon}_1 = 1.0 \cdot 10^{-4}$, $\dot{\epsilon}_2 = 2.5 \cdot 10^{-5}$, and $\dot{\epsilon}_3 = 5.0 \cdot 10^{-6}$.

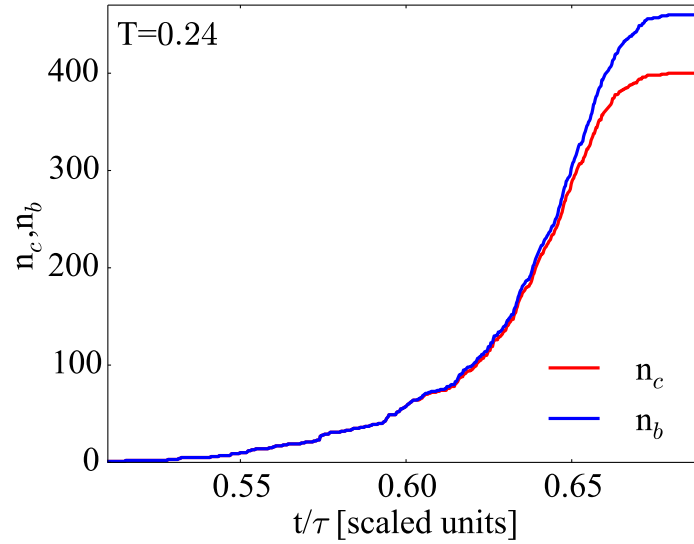
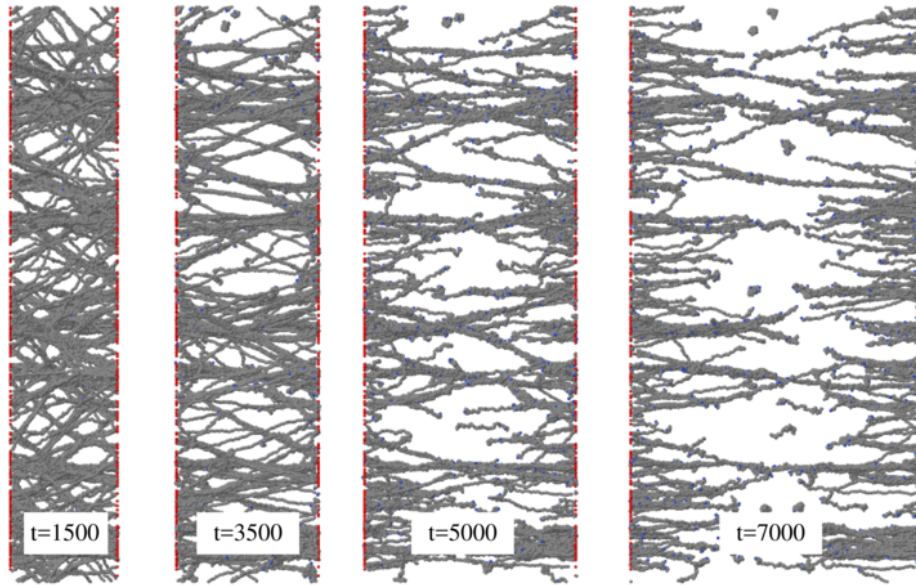


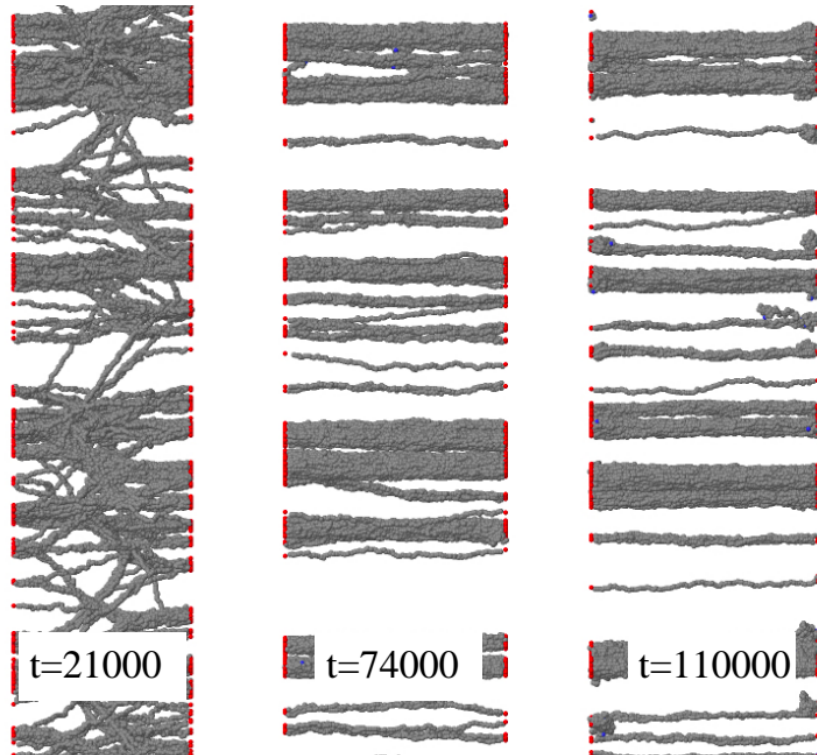
Figure 8.14: Broken chains and bonds as a function of normalised time at $T = 0.24$ and constant strain rate $\dot{\epsilon}_1 = 1.0 \cdot 10^{-4}$.

bonds, seen in Figure 8.16C. But, the form of the chain breaking curve is different then the previous cases. The chain breaking rate now follows a more linear form in, until 50% of the chains have been broken. Than the chain breaking rate follows the same analanche form as the regular systems illustrated by a comparison between a regular periodic bundle at $F = 450$ and an extensible periodic bundle at $F = 360$ given in Figure 8.16D.

This system completes the presentation of our simulation results.

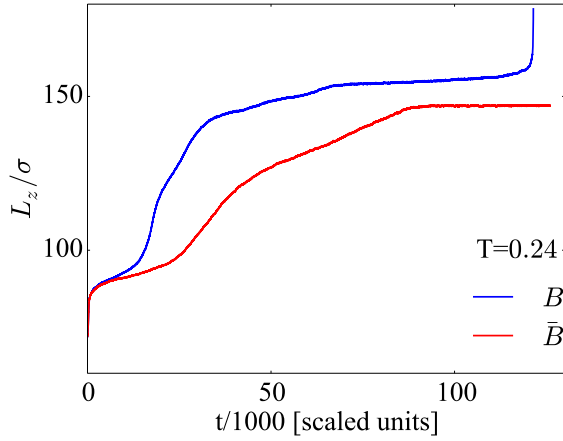


(A) Snapshots of an extensible periodic sample with non-movable head beads.

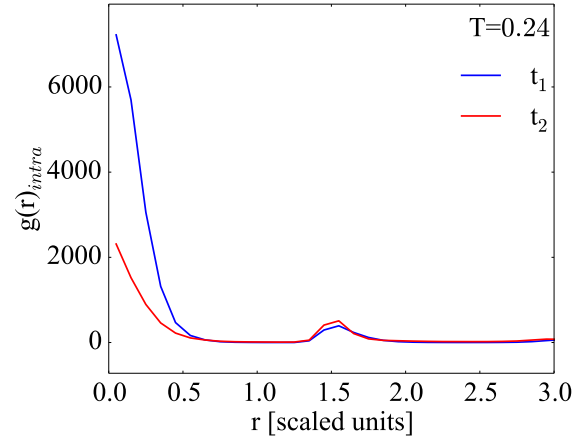


(B) Snapshots of an extensible periodic sample with movable head beads.

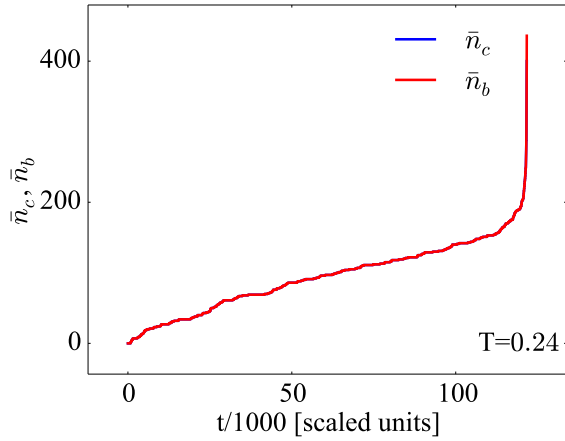
Figure 8.15: Snapshots from the simulations of regular periodic bundles at low density with non-movable (Figure 8.15A) and movable (Figure 8.15B) head beads at $T = 0.24$ and $F = 380$. Red beads illustrate the chains head points, gray beads represent intact bonds, and blue beads illustrate broken bonds.



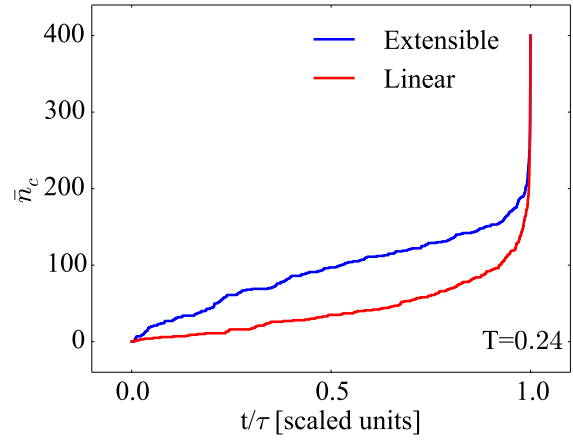
(A) The length of extensible periodic bundles allowing (blue) and preventing (red) bond breaking during the equilibration process as a function of time at $F = 380$ and $T = 0.24$.



(B) The intrachain correlation function before (t_1) and after (t_2) the phase transition in an extensible periodic bundle at $F = 360$ and $T = 0.24$.



(C) Broken chains and broken bonds as a function of time.



(D) A comparison of broken chains in a regular periodic bundle at $F = 450$ and an extensible periodic bundle at $F = 380$. Both samples at $T = 0.24$.

Figure 8.16: Interesting observables from the simulations of extensible periodic bundles.

9 | SUMMARY AND CONCLUSIONS

For nearly a century the FBM represented the approach of choice to model the breaking of fibrous materials under tension [17], especially when taking place under moderate load by creep or fatigue. Following early applications in theoretical studies complementing experiments on textile fibres, wood or paper, the FBM has been developed into a computational tool widely used for computer simulations, often in conjunction with modern theories of phase transitions and critical phenomena, emphasising cooperativity, universality and scaling in their description of the breaking process.

Over the years, the model has incorporated many additions, accounting for non-Hookean bonds, mixtures of different fibres, soft clamps, etc [1]. In its most basic formulation, however, the FBM does not include mass and inertia effects, it does not account for packing of fibres and does not describe the interplay of crystal, liquid, amorphous and coexisting crystal-amorphous phases.

The original plan of my thesis has been to re-introduce into the model as many as possible of the missing features.

My work started from a recent development on the same subject due to Linga et al. [4]. In their study, the Authors implemented and validated a particle-based version of the fibre-bundle model, in which bonds are identified by the particles they join. Particles, in turn, are identified by their instantaneous position and momentum, that are evolved in time using classical molecular dynamics. Particles, in particular, interact with each other via an idealised polymer-like reactive force field, that allows the breaking of bonds and thus of chains and bundles. Moreover, temperature and pressure are set by suitable thermostat and barostat. The system properties are estimated by analysing the configurations visited by the system over time. To investigate creep, an axial load is applied to the bundle, greatly enhancing the rate of thermally activated breaking of bonds that eventually triggers the final avalanche terminating the sample integrity.

For the sake of computational expediency, however, Linga's model neglects all non-bonded bead-bead interactions, thus providing an over simplified view of the system properties, lacking many of the features and properties one is interested in.

My task, therefore, has been to introduce non-bonded bead-bead interactions, introducing short range repulsion forces as well as medium range dispersion (van der Waals) interactions. In this way, polymer beads acquire a non-vanishing size, together with the ability to form different phases, from liquid to crystal or to amorphous. The addition of non-bonded interactions has drastically altered the nature of the computational task, increasing the cost and the complexity of the computation. However,

the addition of non-bonded interactions has brought a wide range of phenomena within the reach of the model, that, in many cases, we have been able to observe by simulations. In this respect, I think that the original aim of the thesis has been fully achieved.

For instance, as a result of my additions to the basic IFM, our model reproduces a variety of new features, including finite size effects, phase changes driven by variations in temperature or in the applied load, as well as regular (i.e., smooth) or anomalous size effects, arising from the packing of chains and from the structure and properties of the surfaces delimiting the bundle.

Besides our focus on creep and thus on bond-breaking processes, and apart from the unusual bundle termination conditions, the model we discuss in many ways merely represents a coarse grained model of polymer bundles, in line with a vast simulation activity on polymers. However, we view it as a model in itself, representing a genuine missing link between the FBM and atomistic or coarse grained force field models. Our subjective point of view is justified by the close correspondence of results with those of traditional FBM, by the prevalence of non-equilibrium and irreversible conditions, and by the simultaneous investigation of strain-controlled and of load-controlled conditions, paralleling the long standing duality of real-life experiments on creep and fatigue.

In the thesis, I first introduced the model, and I described in detail the simulation method. The main body of the thesis is devoted to present representative results for finite bundles of a few hundred chains, as well as for polymeric samples extended in the two directions perpendicular to the longitudinal axis of the bundle.

Our interest in a particle-based FBM is driven primarily by applications in biophysics and in nanosciences. A vast number of biological structures at the cellular level display an apparent fibrous nature, consisting of chain-like molecules self-assembled in bundles, often displaying several levels of structural organisation. Obvious examples are provided by actin bundles in muscles, polysaccharide structures such as cellulose and chitin, collagene and amyloid fibres made by the supra-molecular polymerisation of proteins.

While these considerations are easily acceptable, we realised that the literature lacks a systematic account of the role of fibre bundles in biological systems, discussed from a physicist's point of view. The task of filling this hole in the literature is challenging and exceeds the scope of a Master thesis. However, I carried out the few first steps of this library work, and Chapter 3, 4, and 5 report a short review of mechanical properties of biological fibrous structures made of polynucleotides, polysaccharides and polypeptides, as made, characterised and applied by biophysicists, and, in general, by chemical-physicists.

My library search revealed that most of the experimental and computational effort of the last decades has been driven by the quest of single-molecule mechanical probes. By necessity or by

choice, however, a portion of these studies report data and analyses of bundles of bio-polymers. I think that the bundle-aspect adds new still largely unexplored possibilities of developing new nano-materials tuning their properties to our needs better than possible until now. Unfortunately, this middle ground in between single molecule and bulk material is likely to be the most challenging to explore. Computer simulation, however, provides a powerful approach to undertake this exploration.

I expect that in the near future this line of research will evolve along two major directions.

On the one hand, larger systems still idealised in their interactions will be simulated over much longer times combining advanced simulation techniques, computer science approaches and more powerful computers, possibly based on innovative architectures.

On the other hand, there will be much development towards a more chemically accurate description of the systems whose creep or fatigue properties are being investigated. Efforts in this directions are already under way, and pictorially shown by Figure 9.1, courtesy of Mr. Eivind Bering, representing the stretching and eventual breaking of a 16-chain poly-alanine bundle, described in atomistic detail.

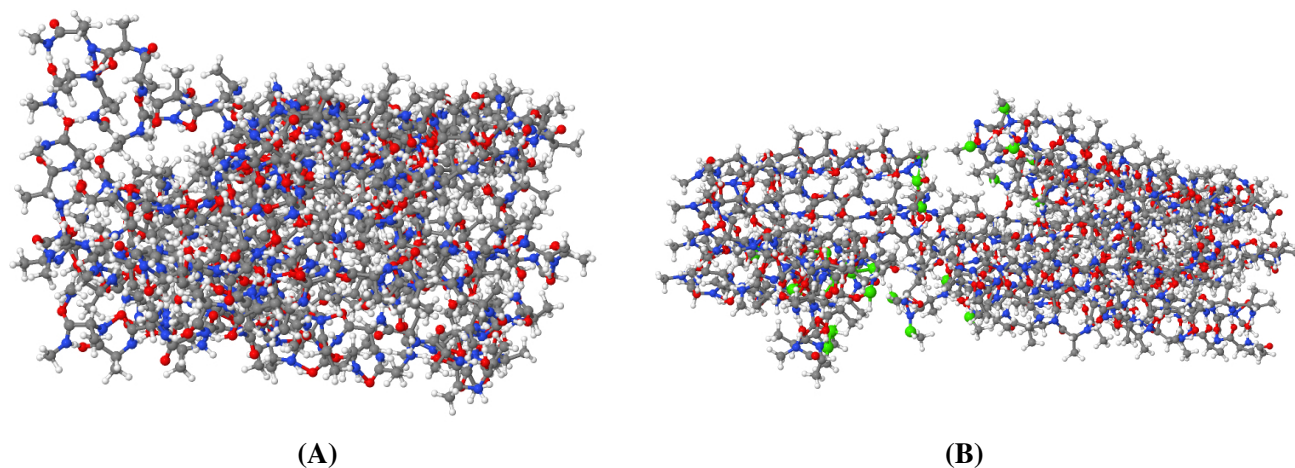


Figure 9.1: Snap shots from a simulation of a real system of polyalanine consisting of 16 fibres before (Figure 9.1A) and after (Figure 9.1B) rupture in a strain-controlled experiment at rate $r = 1.5 \cdot 10^{-5}$. The time between the two snap shots are 1.4 ns. Green beads indicate broken carbon bonds.

Besides the scientific results reported in the thesis, my Master semester achieved "measurable" results represented by:

1. A manuscript is in preparation on the definition and properties of the model, reflecting the content of the second part of the thesis. As such, the manuscript could be completed within a relatively short time.
2. My computations produced a sizeable amount of data on the properties of extensible chains whose stretching and creep behaviour closely match those of DNA. These results could be published soon.

3. My bibliographic exploration of bundles of bio-molecules suggests that a review paper on the mechanical properties of these systems seen from a physical point of view could be very valuable. This plan, however, would take still a long effort, and it is unlikely that it will be done.

BIBLIOGRAPHY

- [1] A. Hansen, P. C. Hemmer, and S. Pradhan, *The fiber bundle model: Modeling failure in materials* (John Wiley & Sons, 2015).
- [2] H. Kamble, M. J. Barton, M. Jun, S. Park, and N.-T. Nguyen, [Royal Society of Chemistry](#) **16**, 3193 (2016).
- [3] S. Kumar and V. M. Weaver, [Cancer and Metastasis Reviews](#) **28**, 113 (2009).
- [4] G. Linga, P. Ballone, and A. Hansen, [Physical Review E](#) **92** (2015).
- [5] V. Palmieri, D. Lucchetti, A. Maiorana, M. Papi, G. Maulucci, F. Calapà, G. Ciasca, R. Gior-dano, A. Sgambato, and M. De Spirito, [Soft Matter](#) **11**, 5719 (2015).
- [6] J. Langowski, [The European Physical Journal E: Soft Matter and Biological Physics](#) **19**, 241 (2006).
- [7] R. Collepardo-Guevara and T. Schlick, [Biochemical Society Transactions](#) **41**, 494 (2013).
- [8] M. Lekka, [Bionanoscience](#) **6**, 65 (2016).
- [9] A. L. McGregor, C.-R. Hsia, and J. Lammerding, [Current Opinion in Cell Biology](#) **40**, 32 (2016).
- [10] Z. N. Scholl, Q. Li, and P. E. Marszalek, [Wiley Interdisciplinary Reviews: Nanomedicine and Nanobiotechnology](#) **6**, 211 (2014).
- [11] G. R. Strobl, *The physics of polymers*, Vol. 2 (Springer, 1997).
- [12] N. I. Abu-Lail and T. A. Camesano, [Journal of Microscopy](#) **212**, 217 (2003).
- [13] P. E. Marszalek and Y. F. Dufrêne, [Chemical Society Reviews](#) **41**, 3523 (2012).
- [14] G. Francius, D. Alsteens, V. Dupres, S. Lebeer, S. De Keersmaecker, J. Vanderleyden, H. J. Gruber, and Y. F. Dufrêne, [Nature Protocols](#) **4**, 939 (2009).
- [15] S. B. Smith, L. Finzi, and C. Bustamante, *Science* **258**, 1122 (1992).
- [16] J. R. Lund and J. P. Byrne, *Civil Engineering and Enviromental Systems* **18**, 243 (2001).
- [17] F. T. Pierce, *Journal of Textile Industry* **17**, 355 (1926).

- [18] S. Sinha, J. T. Kjellstadli, and A. Hansen, [Physical Review E **92** \(2015\)](#).
- [19] P. C. Hemmer and A. Hansen, [Journal of Applied Mechanics **59**, 909 \(1992\)](#).
- [20] F. Kun, H. A. Carmona, J. S. Andrade Jr., and H. J. Herrmann, [Physical Review Letters **100** \(2008\)](#).
- [21] M. J. Buehler, S. Keten, and T. Ackbarow, [Progress in Materials Science **53**, 1101 \(2008\)](#).
- [22] A. Tajik, Y. Zhang, F. Wei, J. Sun, Q. Jia, W. Zhou, R. Singh, N. Khanna, A. S. Belmont, and N. Wang, [Nature Materials **15**, 1287 \(2016\)](#).
- [23] M. Peyrard, [Nonlinearity **17**, 1 \(2004\)](#).
- [24] J. Schnauß, T. Höndler, and J. A. Kös, [Polymers **8** \(2016\), 10.3390/polym8080274](#).
- [25] S. C. Greer, [Journal of Physical Chemistry B **102**, 5413 \(1998\)](#).
- [26] A. Sorrenti, J. Leira-Iglesias, A. J. Markvoort, T. F. A. de Greef, and T. M. Hermans, [Chemical Society Reviews \(2017\), 10.1039/C7CS00121E](#).
- [27] K. John and M. Bär, [Physical Review Letters **95**, 198101 \(2005\)](#).
- [28] N. Bhardwaj and S. C. Kundu, [Biotechnology Advances **28**, 325 \(2010\)](#).
- [29] K. Tonsomboon, A. L. Butcher, and M. L. Oyen, [Materials Science and Engineering C **72**, 220 \(2016\)](#).
- [30] N. C. Seeman, [Annual Review of Biochemistry **79**, 65 \(2010\)](#).
- [31] F. Zhang, J. Nangreave, Y. Liu, and H. Yan, [Journal of the American Chemical Society **136**, 11198 \(2014\)](#).
- [32] L. M. Smith, [Nature **440**, 283 \(2006\)](#).
- [33] P. Ball, “Honey, i shrank the motor,” (2004), Retrieved 31 May 2017 from ”<https://www.theguardian.com/science/2004/jun/10/science.nanotechnology>”.
- [34] S. A. Grigoryev and C. L. Woodcock, [Experimental Cell Research **318**, 1448 \(2012\)](#).
- [35] King’s College London Archive Project Blog, “Short and simple (ish) guide to x-ray diffraction,” (2011), Retrieved 24 March 2017 from ”<http://dnaandsocialresponsibility.blogspot.no/2011/03/short-and-simple-ish-guide-to-x-ray.html>”.

- [36] K. Morris and L. Serpell, [Chemical Society Reviews](#) **39**, 3445 (2010).
- [37] S. Kumar and M. S. Li, [Physics Reports](#) **486**, 1 (2010).
- [38] K. K. C. Neuman and A. Nagy, [Nature methods](#) **5**, 491 (2008).
- [39] J. M. Francois, C. Formosa, M. Schiavone, F. Pillet, H. Martin-Yken, and E. Dague, [Current Genetics](#) **59**, 187 (2013).
- [40] Y. Li, H. Liang, H. Zhao, D. Chen, B. Liu, T. Fuhs, and M. Dong, [Journal of Nanomaterials](#) (2016).
- [41] I. de Vlaminck and C. Dekker, [Annual Review of Biophysics](#) **41**, 453 (2012).
- [42] J. Rajagopalan and M. T. A. Saif, [Journal of Micromechanics and Microengineering](#) **21** (2011), [10.1088/0960-1317/21/5/054002](#).
- [43] T. Schwartz, “LaTeX: How to draw DNA with LaTeX,” (2015), Retrieved 25 May 2017 from “<https://plantgenerations.wordpress.com/2015/05/14/latex-how-to-draw-dna-with-latex/>”.
- [44] P. Cluzel, A. Lebrun, C. Heller, R. Lavery, J.-L. Viovy, D. Chatenay, and F. Caron, [Science](#) **271**, 792 (1996).
- [45] S. B. Smith, Y. Cui, and C. Bustamante, [Science](#) **271**, 795 (1996).
- [46] A. Singh and N. Singh, [Physica A: Statistical Mechanics and its Applications](#) **392**, 2052 (2013).
- [47] T. R. Strick, M.-N. Dessinges, G. Charvin, N. H. Dekker, J.-F. Allemand, D. Bensimon, and V. Croquette, [Reports on Progress in Physics](#) **66**, 1 (2002).
- [48] J. Liphardt, B. Onoa, S. B. Smith, I. Tinoco Jr., and C. Bustamante, [Science](#) **733**, 733 (2001).
- [49] D. Collin, F. Ritort, C. Jarzynski, S. B. Smith, I. Tinoco Jr., and C. Bustamante, [Nature](#) **437**, 231 (2005).
- [50] J. Gore, Z. Bryant, M. Nöllmann, M. U. Le, N. R. Cozzarelli, and C. Bustamante, [Nature](#) **442**, 836 (2006).
- [51] G. A. King, E. J. G. Peterman, and G. J. L. Wuite, [Nature Communications](#) **7** (2016), [10.1038/ncomms11810](#).
- [52] D. J. Kauert, T. Kurth, T. Liedl, and R. Seidel, [Nano Letters](#) **11**, 5558 (2011).

- [53] M. Krause and K. Wolf, [Cell Adhesion & Migration](#) **9**, 357 (2015).
- [54] A. Buxboim, I. L. Ivanovska, and D. E. Discher, [Journal of Cell Science](#) **123**, 297 (2010).
- [55] A. Fruleux and R. J. Hawkins, [Journal of Physics: Condensed Matter](#) **28**, 1 (2016).
- [56] C. Guilluy, L. D. Osborne, L. Van Landeghem, L. Sharek, R. Superfine, R. Garcia-Mata, and K. Burridge, [Nature Cell Biology](#) **16**, 376 (2014).
- [57] K. Maeshima, S. Hihara, and M. Eltsov, [Current Opinion in Cell Biology](#) **22**, 291 (2010).
- [58] O. Ordu, A. Lusser, and N. H. Dekker, [Biophysical Reviews](#) **8**, 33 (2016).
- [59] L. H. Pope, M. L. Bennink, K. A. Van Leijenhurst-Groener, D. Nikova, J. Greve, and J. F. Marko, [Biophysical Journal](#) **88**, 3572 (2005).
- [60] H. Schiessel, [Journal of Physics: Condensed Matter](#) **15**, 699 (2003).
- [61] Y. Cui and C. Bustamante, [Proceedings of the National Academy of Sciences](#) **97**, 127 (2000).
- [62] M. L. Bennink, S. H. Leuba, G. H. Leno, J. Zlatanova, B. G. de Grooth, and J. Greve, [Nature Structural & Molecular Biology](#) **8**, 606 (2001).
- [63] T. Abitbol, A. Rivkin, Y. Cao, Y. Nevo, E. Abraham, T. Ben-Shalom, S. Lapidot, and O. Shoseyov, [Current Opinion in Biotechnology](#) **39**, 76 (2016).
- [64] C. Niederberger, "Drawing cellulose," (2013), Retrieved 25 May 2017 from "<http://www.mychemistry.eu/2013/03/drawing-cellulose/>".
- [65] M. Rief, M. Gautel, F. Oesterhelt, B. Heymann, and H. E. Gaub, [Science](#) **275**, 1295 (1997).
- [66] P. E. Marszalek, A. F. Oberhauser, Y.-P. Pang, and J. M. Fernandez, [Nature](#) **396**, 661 (1998).
- [67] P. E. Marszalek, H. Li, A. F. Oberhauser, and J. M. Fernandez, [Proceedings of the National Academy of Sciences of the United States of America](#) **99**, 4278 (2002).
- [68] P. E. Marszalek, H. Li, and J. M. Fernandez, [Nature Biotechnology](#) **19**, 258 (2001).
- [69] G. Guhados, W. Wan, and J. L. Hutter, [American Chemical Society](#) **21**, 6642 (2005).
- [70] A. J. Svagan, M. A. S. A. Samir, and L. A. Berglund, [Advanced Materials](#) **20**, 1263 (2008).
- [71] J. G. Torres-Rendon, F. H. Schacher, S. Ifuku, and A. Walther, [Biomacromolecules](#) **15**, 2709 (2014).

- [72] K. Sutjarittangtham, T. Tunkasiri, P. Chantawannakul, U. Intatha, and S. Eitssayeam, [Journal of Computational and Theoretical Nanoscience](#) **12**, 798 (2015).
- [73] I. Usov, G. Nyström, J. Adamcik, S. Handschin, C. Schütz, A. Fall, L. Bergström, and R. Mezzenga, [Nature Communications](#) **6** (2015), [10.1038/ncomms8564](#).
- [74] Y. Bao, D. Xu, L. Qian, L. Zhao, Z.-Y. Lu, and S. Cui, [Nanoscale](#) **9**, 3382 (2017).
- [75] J. Kopeček, [Biomaterials](#) **28**, 5185 (2007).
- [76] E. Hermansson, E. Schuster, L. Lindgren, A. Altskär, and A. Ström, [Carbohydrate Polymers](#) **144**, 289 (2016).
- [77] L. B. Strand, A. E. Coron, and G. Skjak-Braek, [Stem Cells Translatoinal Medicine](#) **6**, 1053 (2017).
- [78] G. Pletikapić, H. Lannon, Ü. Murvai, M. S. Z. Kellermayer, V. Svetličić, and J. Brujic, [Bio-physical Journal](#) **107**, 355 (2014).
- [79] Y. X. Chen, B. Cain, and P. Soman, [AIMS Materials Science](#) **4**, 363 (2017).
- [80] B. Alberts, A. Johnson, J. Lewis, M. Raff, K. Roberts, and P. Walter, *Molecular biology of the cell*, 5th ed. (Garland Science, 1997).
- [81] J. M. Berg, J. L. Tymoczko, and L. Stryer, *Biochemistry*, 6th ed. (W. H. Freeman and Company, 2007).
- [82] B. D. Hoffman and J. C. Crocker, [Annual Review of Biomedical Engineering](#) **11**, 259 (2009).
- [83] I. Su and M. J. Buehler, [Nanotechnology](#) **27**, 1 (2016).
- [84] M. J. Buehler, [Journal of Materials Research](#) **21**, 1947 (2006).
- [85] Y. Liu, R. Ballarini, and S. J. Eppell, [Interface Focus](#) **6** (2016), <http://dx.doi.org/10.1098/rsfs.2015.0080>.
- [86] A. Gautieri, S. Vesentini, A. Redaelli, and M. J. Buehler, [Nano Letters](#) **11**, 757 (2011).
- [87] L. Yang, K. O. V. D. Werf, P. J. Dijkstra, J. Feijen, and M. L. Bennink, [Journal of the Mechanical Behavior of Biomedical Materials](#) **6**, 148 (2012).
- [88] Z. L. Shen, H. Kahn, R. Ballarini, and S. J. Eppell, [Biophysical Journal](#) **100**, 3008 (2011).

- [89] R. B. Svensson, H. Mulder, V. Kovanen, and S. P. Magnusson, [Biophysical Journal](#) **104**, 2476 (2013).
- [90] S. E. Szczesny and D. M. Elliott, [Acta Biomaterialia](#) **10**, 2582 (2014).
- [91] R. N. Rambaran and L. C. Serpell, [Prion](#) **2**, 112 (2008).
- [92] T. J. Paul, Z. Ho, C. Wang, M. Shanmugasundaram, J. Dejoannis, D. A. Shekhtman, I. K. Lednev, V. K. Yadavalli, and R. Prabhakar, [The Journal of Physical Chemistry Letters](#) **7**, 2758 (2016).
- [93] G. Lamour, R. Nassar, P. H. W. Chan, G. Bozkurt, J. Li, J. M. Bui, C. K. Yip, T. Mayor, H. Li, H. Wu, and J. A. Gsponer, [Biophysical Journal](#) **112**, 584 (2017).
- [94] M. Schoumacher, R. D. Goldman, D. Louvard, and D. M. Vignjevic, [The Journal of Cell Biology](#) **189**, 541 (2010).
- [95] L. Blanchoin, R. Boujemaa-paterski, C. Sykes, and J. Plastino, [Physiological Reviews](#) **94**, 235 (2014).
- [96] J. M. Ferrer, H. Lee, J. Chen, B. Pelz, F. Nakamura, R. D. Kamm, and M. J. Lang, [Proceedings of the National Academy of Sciences of the United States of America](#) **105**, 9221 (2008).
- [97] S. Tojkander, G. Gateva, and P. Lappalainen, [Journal of Cell Science](#) **125**, 1855 (2012).
- [98] G. Gateva, E. Kremneva, T. Reindl, and J. Dietmar, [Current Biology](#) **27**, 705 (2017).
- [99] M. Maninova, J. Caslavsky, and T. Vomastek, [Protoplasma](#) **254**, 1207 (2017).
- [100] O. Valiron, [Communicative & Integrative Biology](#) **4**, 10 (2011).
- [101] V. VanDelinder, P. G. Adams, and G. D. Bachand, [Scientific Reports](#) , 1 (2016).
- [102] S. Hameroff and R. Penrose, [Physics of Life Reviews](#) **11**, 39 (2014).
- [103] G. Lang, B. R. Neugirg, D. Kluge, A. Fery, and T. Scheibel, [American Chemical Society](#) **9**, 892 (2017).
- [104] J. F. Smith, T. P. J. Knowles, C. M. Dobson, C. E. Macphee, and M. E. Welland, [Proceedings of the National Academy of Sciences of the United States of America](#) **103**, 15806 (2006).
- [105] G. Bratzel and M. J. Buehler, [Biopolymers](#) **97**, 408 (2012).

- [106] D. Frenkel and B. Smit, *Understanding molecular simulations: from algorithms to applications* (Academic Press, 1996).
- [107] P. Ballone, *Entropy* **16**, 322 (2014).
- [108] H. Goldstein, C. P. Poole, and J. L. Safko, *Book*, Vol. 3 (Addison Wesley, 2007) pp. 1–646.
- [109] L. Verlet, *Physical Review* **159**, 98 (1967).
- [110] D. S. D. Larsson, L. Liljas, and D. van der Spoel, *PLoS Computational Biology* **8** (2012).
- [111] Innovaties Supercomputing in Deutschland, “SuperMUC boosts the largest molecular dynamics simulation by 4X in number of particles,” (2013), Retrived 12 Descember 2016 from “http://inside.hlr.de/_old/htm/Edition_01_13/article_06.html”.
- [112] M. Parrinello and A. Rahman, *Journal of Applied Physics* **52**, 7182 (1981).
- [113] N. Grønbech-Jensen and O. Farago, *Molecular Physics* **111**, 983 (2013).

